Resolved Stars' Insights into Galaxy Physics

Yumi Choi

A dissertation
submitted in partial fulfillment of the
requirements for the degree of

Doctor of Philosophy

University of Washington

2016

Reading Committee:

Julianne J. Dalcanton, Chair

Benjamin F. Williams

Evan D. Skillman

Program Authorized to Offer Degree:
Astronomy

University of Washington

Abstract

Resolved Stars' Insights into Galaxy Physics

Yumi Choi

Chair of the Supervisory Committee:
Professor Julianne J. Dalcanton
Astronomy

The history of a galaxy is encoded in its individual stars, and resolved stellar populations in nearby galaxies provide a wealth of information about star formation history (SFH), its relation to the interstellar medium, and galactic dynamics/structures. Using the power of resolved stars, imaged in multiple wavelengths by the Hubble Space Telescope, I investigate different types of galactic physics in three nearby galaxies: (1) measuring the escape fraction of ionizing photons from NGC 4214 and discussing its implications for cosmic reionization, (2) testing the density wave theory in M81 and understanding the origin of its spiral arms, and (3) tracing stellar overdensity features in M31 using red giant branch (RGB) stars and studying potential causes of the overdensities. In each of these studies, I developed and tested new methodology.

First, I develop a new approach to measure the escape fraction of ionizing photons from a galaxy, and apply the technique to the nearest starburst dwarf galaxy NGC 4214. This new technique includes inferring the intrinsic ionizing fluxes from individual stars within a galaxy as well as the amount of absorption by the intervening dust by modeling the observed individual stars' spectral energy distributions (SEDs), constructed from multi-wavelength HST observations, using the probabilistic SED fitting tool, called BEAST (Bayesian Extinction And Stellar Tool). By combining these measurements with the estimates of the amount of consumed ionizing photons by photoionization using the Hα luminosity, I present the escape fraction map for NGC 4214 with unprecedented spatial resolution. I found a sig-

nificant spatial variation in the escape fraction across the galaxy, and a ∼60 times higher global escape fraction (∼12%) than the previous measurement.

Second, I use resolved stellar populations to trace prominent spiral structures in M81, which are highlighted by blue, young stars, and to understand the underlying dynamical mechanisms between star formation and these galactic structures. The origin of grand-design spiral patterns has been extensively explored observationally. However, the conclusions from different studies have often conflicted even for the same galaxies. The discrepancies mainly result from estimating the age gradient using discontinuous tracers, such as star clusters and gas/dust emissions including HI, 24μm, CO and Hα. Instead of using discontinuous tracers, I model color-magnitude diagram that are constructed from resolved stars in M81 to derive spatially resolved SFHs around one of M81's spiral arms and compare with the star formation propagation predicted by the density wave theory. I find that the grand-design spiral arms in M81 are likely induced by tidal interaction with companion galaxies about 200–300 Myr ago, not by the density waves.

Finally, I use resolved stellar populations to investigate the global structures of the M31's disk. Specifically, I make use of old RGB stars, selected based on their near-IR color and magnitude from the Panchromatic Hubble Andromeda Treasury (PHAT) survey data. The selected RGB stars directly trace the stellar mass distribution in M31, whereas a standard approach (i.e., modeling two-dimensional IR surface light profile) to quantify the disk structures is biased due to variation in mass-to-light ratio among different stellar populations. From the constructed RGB stellar number density map, I constrain the disk structures of M31, trace the overdensity features at 5 and 10 kpc, and examine possible causes for this overdensity. This research project is in progress. Thus, in this thesis, I will briefly show preliminary results.

TABLE OF CONTENTS

LIST OF FIGURES

Figure Number Page

LIST OF TABLES

Table Number Page

ACKNOWLEDGMENTS

This research would not have been possible without support and guidance from my advisor, Professor Julianne Dalcanton, and the other members of my committee, Professors Benjamin Williams and Evan Skillman.

I have met many fantastic collaborators during my thesis. Special thanks to Morgan Fouesneau, Anil Seth, Dan Weisz, Karl Gordon, and Dustin Lang for sharing their expertise with me. To Thomas Quinn for valuable conversations on spiral arms.

I also thank to Professors Andy Connolly, Scott Anderson, and Željko Ivezić for giving me an opportunity to work on the AGN variability during my first three years. Former astronomers Robert Gibson and Andrew Becker have provided helpful feedback during this project.

I am fortune to have great classmates Yusra AlSayyad, Lauren Anderson, Lori Beerman, Patricia Carroll, James Davenport, Amit Misra, and Aomawa Shields. You guys are awesome.

Finally, I thank to my family in South Korea for their endless love and support.

DEDICATION

To my husband, Jaehoon, for his support and encouragement.

Chapter 1

INTRODUCTION

The history of a galaxy is encoded in its individual stars, giving us insight into galaxy physics. An analysis of multi-wavelength photometry of individual stars provides a wealth of information about star formation (SF), its interaction with the surrounding interstellar medium (ISM), and galactic dynamics/structures. With the aid of this great power of resolved stars, my dissertation focuses on addressing mainly two questions on galaxy physics: the role of dwarf starburst galaxies at the epoch of reionization using NGC 4214, and the origin of galactic structures in two giant spiral galaxies M81 and M31. To address these questions, I use resolved stars in these galaxies, imaged by the Hubble Space Telescope (HST) in multiple wavelengths. The knowledge obtained from detailed studies of nearby galaxies improves our understanding of higher redshift (z) galaxies that we cannot look into in detail.

1.1 The Power of Multi-wavelength Photometry of Individual Stars

All information we receive from a star is carried by photons, which originate in the star's atmosphere. Models of stellar atmospheres combined with stellar evolutionary tracks can generate a synthetic stellar spectrum for a given stellar age, initial mass, surface gravity, temperature, and metallicity. These stellar parameters determine the amount of energy emitted as a function of wavelengths, i.e., the spectral energy distribution (SED). For a given set of stellar parameters, it is possible to predict the brightness in each bandpass and the difference in brightness between bandpasses (i.e., color). Thus, spectral analysis of the observed star is a key tool to derive fundamental stellar properties.

Figure 1.1 shows examples of the ultraviolet (UV), optical, and infrared (IR) color-magnitude diagrams (CMDs) of artificial stars with different stellar parameters. Stellar age is a primary parameter to determine the positions of stars on CMDs. Young stars are blue in the ultraviolet (UV), optical, and infrared (IR) colors, while older stars are redder in all these colors. Because young stars emit more energy at short wavelengths, they are bright in shorter wavelength bandpasses and faint in the IR bandpasses. Old stars, on the other hand, emit more energy at longer wavelengths, making them brighter than young stars in the IR bandpasses. Metallicity is one of the secondary parameters. Even for stars with the same age, their different metallicities can put them in different positions on CMD.

There is another important factor affecting stellar SEDs – dust. Before the emitted photons reach an observer, they interact with any dust between the star and the observer. The interaction with the intervening dust modifies the intrinsic stellar SED via absorption and scattering. The interstellar extinction law describes the sum of these two physical processes as a function of wavelength. The extinction law is well estimated through far-UV (FUV) to IR by observations. Therefore, it is possible to generate a model stellar SED for a given set of stellar and dust parameters, by applying the extinction law to the intrinsic stellar SED. Therefore, comparison of star's multi-wavelength observations with model stellar SEDs allows us to infer the properties of that star and the intervening dust.

These derived stellar and dust properties allow us to reconstruct the star formation history (SFH) of a galaxy, and to understand the interaction between the stellar populations and the surrounding ISM. Also, it is possible to study galaxy dynamics and structures by exploring the change in spatial distributions of distinct stellar populations over time. This allows us to investigate the relationship between galactic structures and stellar populations confined to each structural component.

1.2 Massive Stars in a Dwarf galaxy as Sources for Cosmic Reionization

In spite of their short lifetime (< 10 Myr), massive stars play many important roles in various astrophysical fields. In particular, massive stars interact with the ISM both radiatively through the tremendous amount of ionizing photons they produce and mechanically through their energetic stellar feedback. Some ionizing photons are absorbed by the ISM and are reprocessed within a galaxy, while the others can travel far enough to escape from the galaxy through low-density holes and interact with the intergalactic medium (IGM). These photons produced by massive stars are thought to be responsible for cosmic reionization in

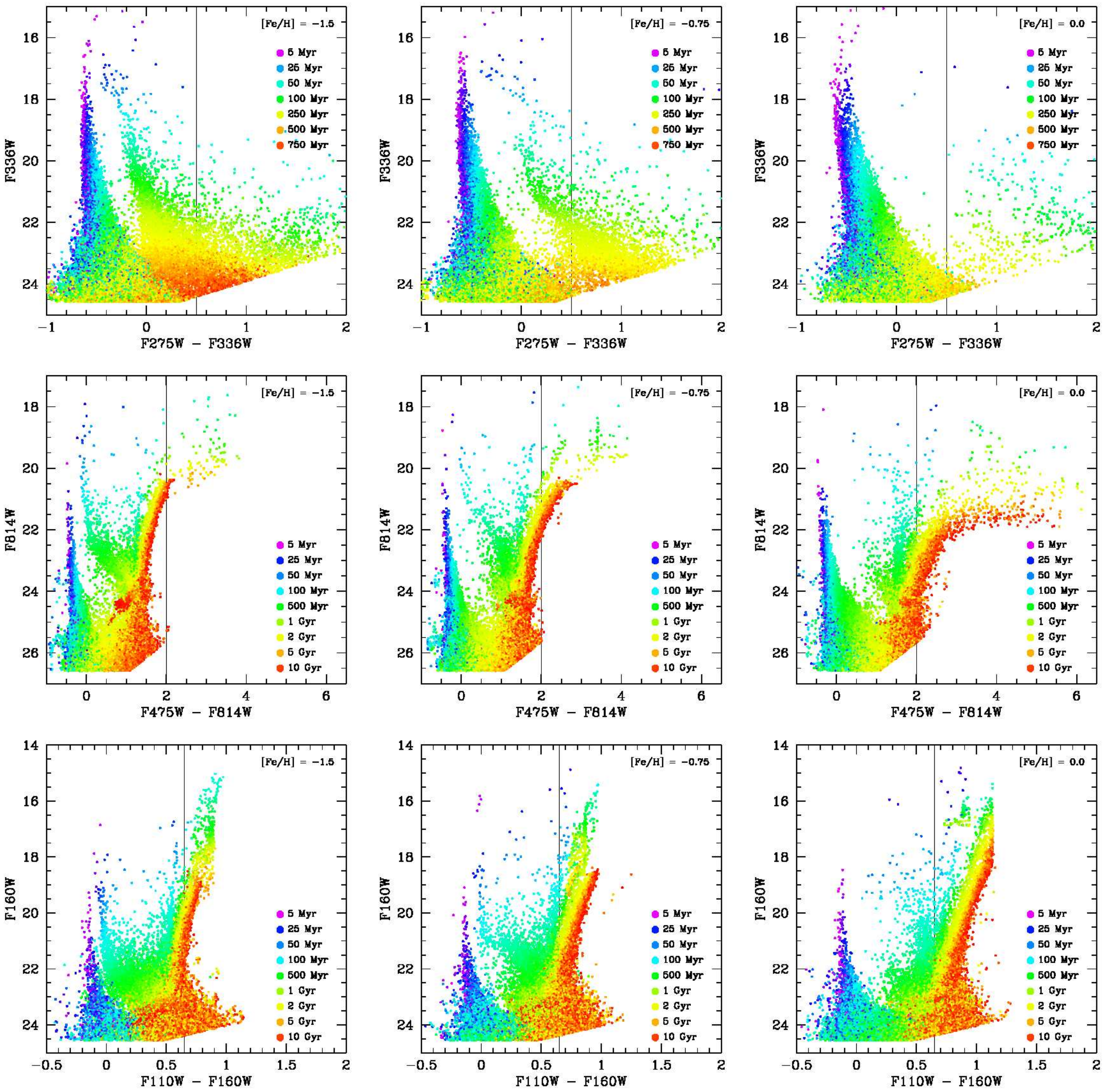

Figure 1.1 Simulated CMDs for WFC3/UVIS (top row), ACS/WFC (middle row), and WFC3/IR (bottom row), for three different metallicities ([Fe/H] = −1.5, −0.75, and 0.0; left, middle, and right columns, respectively), with points color coded by age. The simulations assume a constant star formation rate, no foreground or internal extinction, and photometric errors and completeness derived from artificial star tests for outer disk fields in M31. The solar metallicity CMDs are most likely to be characteristic of the young stellar populations throughout the disk, and the older stellar populations in the bulge. The intermediate metallicity ([Fe/H] = −0.75) CMDs are likely to be representative of the older thin and thick disk stars (e.g., Collins et al. 2011), and the low metallicity CMDs are likely to be characteristic of a potential stellar halo population (Chapman et al. 2006; Kalirai et al. 2006). Age color-coding is the same for all plots in single row, but varies from camera to camera. Vertical lines are plotted at a constant color for each camera, and are shown for reference, to allow comparisons between different metallicities. Figure from Dalcanton et al. (2012), reproduced by permission of the AAS.

the early universe.

Massive stars, especially in dwarf starburst galaxies, have a significant effect on cosmic reionization, because small galaxies' shallow gravitational potential wells allow for stellar feedback from massive stars to destroy the global ISM easily. For example, the first supernova (SN) explosion in a SF region can blow out most of the residual gas along the optically thin paths out beyond the host galaxy's gravitational potential, clearing holes. Then, ionizing photons, produced by massive stars that have not been explored as SNe, readily escape through these holes. The giant holes cleared by SN winds in these dwarf galaxies can be thought of as giant matter-bounded H II regions, sometimes called superbubbles.

Stellar feedback in more massive galaxies is less likely affect the global ISM. In this case, the stellar feedback is rather localized, meaning no low-density channels/holes reaching to the IGM. Furthermore, even if SN explosion blows out the surrounding gas, the leaked ionizing photons from H II regions are likely to be consumed by diffuse gas in the galactic halo. Therefore, massive stars in dwarf galaxies rather than those in massive galaxies are likely a dominant source for cosmic reionization (e.g., Bouwens et al. 2012; Robertson et al. 2013; Wise et al. 2014).

Although many observational and theoretical studies have suggested the importance of dwarf galaxies to cosmic reionization, the fraction of ionizing photons that escape from these galaxies into the IGM (the escape fraction, $f_{\rm esc}$) is poorly constrained (e.g., Siana et al. 2007; Iwata et al. 2009; Vanzella et al. 2012). There are remarkably few constraints on the details of this photon escape process, in spite of its importance in shaping the properties of the entire IGM.

Cosmological simulations often require the mean value of global $f_{\rm esc}$ at the reionization epoch to be higher than 20% (e.g., Ouchi et al. 2009; Wise & Cen 2009; Yajima et al. 2011) to match the observed ionization state of the IGM by z = 6 (e.g., Gunn & Peterson 1965; Fan et al. 2006; Dunkley et al. 2009). This tuned parameter is sensitive to the choice of the faint end UV luminosity function. If models include galaxies brighter than $M_{\rm UV}$ = -13, then $f_{\rm esc}$ can be constrained between 10% – 20%. However, if models consider only galaxies brighter than $M_{\rm UV}$ = -18, then $f_{\rm esc}$ is required to be higher than ∼30%. Furthermore, there is no consensus about the dependence of $f_{\rm esc}$ on galaxy properties or redshift.

Unfortunately, no existing observational measurements of f_{esc} match this high value at any redshifts (e.g., Shapley et al. 2006; Iwata et al. 2009; Vanzella et al. 2012; Nestor et al. 2013, Bergvall et al. 2006; Leitet et al. 2013). These low f_{esc} measurements may be due to biased sample selection towards strong emission line galaxies (i.e., high H I column density, thus insignificant leakage of ionizing photon), large uncertainty in UV background subtraction, and/or uncertain IGM transmission (e.g., Bergvall et al. 2013). These measurements are largely inconclusive because they must rely on a number of coarse assumptions that can strongly bias results to low escape fractions. Thus, we need more independent f_{esc} measurements from individual galaxies to better constrain f_{esc}.

In this thesis, I begin to remedy this situation by developing an entirely new methodology that (1) uses spectral energy distribution fitting of resolved stars to infer both the production of ionizing photons and their absorption by dust and (2) uses narrow-band images of Balmer lines to track the absorption of ionizing photons by neutral gas. These measurements allow us to derive maps of the ionizing escape fraction across the face of a galaxy, while avoiding assumptions about dust geometry along the line-of-sight and systematic errors inherent in using spatially-averaged spectra to infer the ionizing photon production rate. I apply this new technique to the nearby starburst galaxy NGC 4214. Using this galaxy as a test case, we can shed light on limitations in traditional methodologies by comparing to the results from our new method. This simpler methodology can easily be applied to a much larger sample of nearby galaxies, allowing a broad attack on understanding this important but elusive process.

1.3 Resolved Stars as Tracers of Galactic Structures

The present day structure of a disk galaxy reflects the formation and evolution of the galaxy. This is because the complex galactic structures are determined both by initial conditions and internal secular evolution following dynamical interactions. All of these processes can affect SF, which means resolved stellar populations can paint time on galactic structures. In other words, we infer a dynamical event at a given lookback time by investigating the spatial distribution of stellar populations for that given age. Thus, the decomposition of structural components as a function of time in galaxies is key to understanding the history of interactions between SF activities and galactic dynamics.

Using young stellar populations, one can infer the recent dynamical events that lead to formation of those young stars. In particular, young stellar populations are good tracers of spiral patterns in disk galaxies. Although more than half of galaxies in the Local Universe show spiral patterns highlighted by young stars (e.g., Lintott et al. 2008; Nair & Abraham 2010), their origin remains an open question. Several theories have been suggested to explain the underlying mechanisms connecting spiral patterns and SF. There are two models that are most widely accepted: the density wave theory for long-lived arms (Lindblad 1960; Lin & Shu 1964) and the gravitational instability model for short-lived transient arms (Goldreich & Lynden-Bell 1965; Julian & Toomre 1966; Sellwood & Carlberg 1984). While the density wave theory can explain active SF in the spiral arms as a result of the gas compression by the waves, the gravitational instability model predicts self-propagating stochastic SF.

If we assume stable density waves propagating through a galactic disk with a constant angular pattern speed, the corotation radius, Rcr, is expected to lie where the spiral pattern speed becomes the same as the rotational speed. Materials in the disk move faster than the density waves inside $R_{\rm cr}$, and vice versa outside $R_{\rm cr}$. When atomic or diffuse gas enters into spiral arms (upstream of the shock), it experiences a strong shock and gets compressed. This naturally leads to the formation of molecular clouds where stars form. Newly formed stars disperse surrounded molecular clouds through stellar feedback and continue to move away from spiral arms (downstream of the shock). Therefore, one should be able to find a systematic spatial ordering among SF/gas tracers with different timescales (e.g., H I for the cold dense gas, 24μm for obscured stars, and Hα for the young stars) within spiral arms that are supported by quasi-static density waves.

With grand-design spiral galaxies, many efforts have been made to measure such angular offsets among different SF/gas tracers. Findings and conclusions on the angular offsets have been different even for the same galaxy (Tamburro et al. 2008; Egusa et al. 2009; Foyle et al. 2011). While Foyle et al. (2011) found no evidence for a systematic ordering of different tracers, Tamburro et al. (2008) and Egusa et al. (2009) detected the systematic ordering of angular offsets. However, the amount of measured angular offsets are different from each other and thus the estimated timescales for the total SF processes are also different. Some recent studies even found no significant observational evidence favoring the density wave theory in nearby grand-design spiral galaxies (e.g., Foyle et al. 2011; Ferreras et al. 2012). Louie, Koda, & Egusa (2013) showed that this discrepancy is mainly caused by the choice of SF/gas tracers to measure the angular offsets. To study SF propagation across spiral arms, I perform a CMD-based SFH analysis in M81. This analysis tests the density wave theory completely independent of angular offset measurements.

Using old stellar populations, one can study the global structures of galaxies as well. A traditional way to unveil a global galactic shape is to model the 1-D or 2-D surface brightness profile of the galaxy. Profiles of galactic surface brightness have revealed that typical disk galaxies consist of at least three major structural components (bulge, exponential disk, and spiral arms). Galactic structures are usually more complex than this, and include additional components, such as bars, inner spiral arms, rings, etc. This traditional method, however, is limited for tracing the stellar mass directly due to variation in mass-to-light ratio among different stellar populations. Contrary to this traditional way, tracing the galactic structure with old stellar populations (e.g., red giant branch stars) is a more direct measure of underlying stellar mass.

The Andromeda (M31) is the nearest large disk galaxy, like as our own galaxy. M31 is one of the common types of spiral galaxies. Thus detailed analysis on M31's galactic structures provides valuable information on spiral galaxy in general. M31's surface brightness profile indicates that it has a complex inner structure and a prominent 10 kpc feature. The inner disk region consists of a weak nucleus, a boxy bulge, and a bar (Beaton et al. 2007). It is still not clear whether the prominent feature at around 10 kpc is spiral arms or ring. It is highly inclined ($i = 77.5$ degree), making it challenging to explore M31's galactic structures, and thus its origin as well. There is another interesting feature found at 5 kpc where the bar ends.

Inner and outer galactic structures are strongly correlated with each other. In particular, the non-axisymmetric bar can induce spiral/ring structures and drive the secular evolution in a galaxy. Therefore, characterizing these prominent galactic structures at 5 kpc and 10 kpc and exploring any possible connection with the bar might be a key to understanding the origin of these features. However, there might be other causes for these structures, such as collision or tidal interactions with M31's companion galaxies. There are many direct/indirect evidence for tidal interactions with M31's satellite galaxies: stellar debris, H I gas bridge, enhanced SFR, enriched metallicity, and dynamically hot populations.

With the Panchromatic Hubble Andromeda Treasury (PHAT; Dalcanton et al. 2012) photometry (Williams et al. 2014), it is possible to construct a red giant branch (RGB) stellar number density map, which is a direct tracer of the underlying stellar mass distribution. The RGB stellar number density map allows to constrain the global structure of M31 and quantify the prominent two galactic features at 5 kpc and 10 kpc. By comparing their observed properties with the predictions from different underlying mechanisms, their origin can be revealed.

1.4 Outline

The brief outline for this thesis is as follows. In Chapter 2, I describe a new methodology to measure the escape fraction of ionizing photons from well-resolved nearby galaxies. I present the measurements of both local and global escape fractions for starburst dwarf galaxy NGC 4214, and discuss the role of dwarf star-forming galaxies in the epoch of reionization.

In Chapter 3, I derive the recent SFHs of 20 regions around one of M81's grand-design spiral arms. Using the resulting spatially resolved SFHs, I test the traditional density wave theory by searching for the age gradients across the spiral arm that are predicted from the density wave theory. I then discuss the underlying mechanisms for the grand-design spiral arms in M81.

In Chapter 4, I explore the global disk structures of M31. I construct the RGB stellar number density map using the PHAT NIR photometry, constrain the global structures using the WISE W1 [3.4 μm] mosaic image and the RGB map, and then trace overdensity features. I investigate potential causes for these overdensity structures. This work is in progress, thus the results presented in this thesis are preliminary.

Finally, in Chapter 5, I provide the summary of the work in this thesis.

Throughout this document, the pronoun "we" is used to refer to myself (the lead investigator for all of the work presented here) and my co-investigators who assisted in this research.

Chapter 2

MAPPING THE ESCAPE FRACTION FOR NGC 4214

We present a new method for measuring the escape fraction of ionizing photons from galaxies using resolved stellar photometry. We then apply this technique to a nearby analog for the high-redshift starbursts thought to be responsible for cosmic reionization. The starburst dwarf galaxy NGC 4214 has been imaged with the high-resolution of WFC3 on HST from the near-UV to the near-IR (F225W, F336W, F438W, F814W, F110W, and F160W). These observations yielded measurements of the broad spectral energy distributions (SEDs) for ∼83,000 resolved stars with good photometric quality. We fit these SEDs to infer the intrinsic properties of individual stars and the intervening dust. We measure the escape fraction by comparing the number of intrinsic ionizing photons with the number of ionizing photons that are either absorbed by dust or used to ionize the surrounding neutral hydrogen, derived based on the extinction-corrected Hα emission. We find that the local escape fractions vary significantly across NGC 4214 with much of the ionizing flux escaping through a few channels towards us. The global escape fraction is ∼11.84%, which is higher by a factor of ∼60 than the previous measurement. The discrepancy shows how spatially-averaged spectroscopy or imaging can underestimate the escape fraction, highlighting the importance of spatial resolution in measuring the ionizing photon escape fraction.

2.1 Introduction

Cosmic reionization is one of the major events in the evolution of our Universe. Observations of the *Planck* CMB and Lyman α forest absorption in quasar spectra show that hydrogen in the neutral intergalactic medium (IGM) became completely ionized over an extended redshift range $6 \lesssim z \lesssim 10$ (Gunn & Peterson 1965; Fan et al. 2006; McGreer et al. 2015; Planck Collaboration et al. 2015). Ionizing photons escaping from galaxies at $z > 6$ are thought to be the dominant sources for this cosmic reionization (e.g., Barkana & Loeb 2001;

Wise & Cen 2009; Bouwens et al. 2012; Robertson et al. 2013, 2015; Finkelstein et al. 2015). The galaxy ultraviolet (UV) luminosity function up to redshift of ∼10 also suggests that ionizing photons escaping from numerous faint-end star-forming galaxies are sufficient to reionize the early universe (e.g., Bouwens et al. 2015; McLeod et al. 2015).

In this picture, dwarf star-forming galaxies release ionizing photons through low-density holes in their clumpy interstellar medium (ISM), which were created by strong stellar feedback from the most massive stars (e.g., Jaskot & Oey 2013; Alexandroff et al. 2015). The escaped ionizing photons then ionize the surrounding IGM. Therefore, constraining the fraction of ionizing photons that escape into the IGM (the "escape fraction", $f_{\rm esc}$) is the key to confirming whether dwarf star-forming galaxies were indeed responsible for cosmic reionization. Unfortunately, it is impossible to detect escaping ionizing photons from galaxies at the epoch of reionization due to the high fraction of neutral IGM. Therefore, looking at lower-redshift analogs is the only way to constrain the physics controls the escape fraction.

To be consistent with reionizing the universe by redshift $z \sim 6$ (e.g., Fan et al. 2006; Dunkley et al. 2009), the required escape fraction at the reoinization epoch has to be higher than 10–30%, depending on the choice of the ionizing photon production efficiency and the faint end properties of the UV luminosity function (e.g., Ouchi et al. 2009; Finkelstein et al. 2012; Robertson et al. 2013; Bouwens et al. 2015; Khaire et al. 2016). However, there is no theoretical consensus yet; different cosmological simulations predict a wide range of $f_{\rm esc}$, as well as different trends with z (e.g., Gnedin et al. 2008; Wise & Cen 2009; Yajima et al. 2011; Kimm & Cen 2014; Ma et al. 2015; Paardekooper et al. 2015). $f_{\rm esc}$ is also poorly constrained by observations at any redshift (e.g., Siana et al. 2007; Iwata et al. 2009; Vanzella et al. 2012). For example, no existing measurements of $f_{\rm esc}$ match this high value at either large redshift ($z \lesssim$ 4–5) or locally. Very few galaxies show any evidence for leakage – only 1–15% of candidates at high/intermediate-z (Shapley et al. 2006; Iwata et al. 2009; Vanzella et al. 2012; Nestor et al. 2013), and only four cases have detected leakage locally, but only at the few per cent level (Bergvall et al. 2006; Leitet et al. 2013; Borthakur et al. 2014; Leitherer et al. 2016).

Even these handful of local measurements have proven difficult to interpret. These low $f_{\rm esc}$ measurements may be biased due to sample selection from emission line surveys (i.e., high H I column density, thus insignificant leakage of ionizing photon). Instead, Izotov et al. (2016a,b) recently argue that using the line ratio of [O III]λ5007/[O II]λ3727, a proxy for the ionization parameter, is s more efficient to select actual LyC leakers. Another explanation for low f_{esc} measurements may be due to inherent difficulties related with the direct measurement of LyC flux. These include uncertain IGM transmission, large uncertainty in UV background subtraction, and mis-aligned opening angles of low-density holes with our line-of-sight (i.e., lowering the chance to detect leaked ionizing photons).

However, the most fundamental issue may be lack of sufficient spatial resolution to capture the local variation of f_{esc} within a galaxy. The escape of ionizing photons begins with the production of photons by O/B stars in dense star forming regions, which then must propagate through the complex, dusty interstellar medium (ISM) before eventually escaping. Thus, constraining f_{esc} requires measuring (1) the intrinsic ionizing photon production rate, and (2) either the photon absorption rate by the ISM or the amount of leaked ionizing flux. All of these quantities are sensitive to the distribution of hot stars and the ISM topology, which both vary significantly with position within a galaxy. As such, the value of f_{esc} also highly depends on local properties, and must vary spatially. Failure to resolve these small scale properties can lead to large uncertainties in global f_{esc} measurements.

In most existing studies (e.g., Heckman et al. 2011; Leitet et al. 2013; Borthakur et al. 2014; Alexandroff et al. 2015), one infers the intrinsic photon production rate by modeling the observed composite spectrum using synthetic stellar population models that also include dust (e.g., Starburst99; Leitherer et al. 1999). One then directly measures the ionizing radiation leaking from that galaxy by detecting the galaxy below the Lyman limit in the rest-frame. This process necessarily involves significant averaging, which in turn can lead to significant biases. For example, global spectral fits may involve over-correction for the internal extinction, which is determined based on the Balmer decrement. This measures can be biased because (1) actual escaping ionizing photons are not processed within the galaxy at all, and (2) Hα and Hβ recombination lines mainly come from the dust-rich star forming regions. Most prominent line features in the observed composite spectra as well as integrated ionizing and non-ionizing fluxes are both biased towards high-density regions where ionizing photons cannot easily escape. While ionizing photons are created in such regions, they actually escape through low-density or dust-free regions that are created by strong stellar feedback. Thus, applying spatially-averaged extinction corrections, which are likely overestimated, to the entire galaxy inevitably overpredicts the number of intrinsic LyC photons, thereby underestimates the global f_{esc}.

One way to overcome these challenges is to disentangle the resolved stellar populations of galaxies. Nearby starburst dwarf galaxies, in particular, provide excellent laboratories for evaluating the plausibility of early star-forming galaxies as the source of cosmic reionization. High-resolution imaging with the Hubble Space Telescope (HST) resolves individual stars in galaxies closer than 4 Mpc. Furthermore, multi-wavelength imaging with HST allows us to correct for dust star-by-star by modeling their broad stellar spectral energy distributions (SEDs). Recently, our team introduced a stellar SED fitting technique optimized for large resolved star datasets, called the Bayesian extinction and stellar tool (BEAST; Gordon et al. 2016). Given resolved stellar photometry over a range of wavelengths, the BEAST can infer the intrinsic spectrum and intervening absorption from individual stars. These intrinsic spectrum can then be applied to map intrinsic far-UV (FUV) and extreme-UV (EUV) fluxes.

Contrary to existing methodologies, our new approach does not require any spatial averaging, simplifying assumptions about dust/ISM geometry towards our direction, or challenging observations below the Lyman limit. The new approach enables us to infer the intrinsic ionizing photon production rates of individual stars. We also can infer the number of photons absorbed by dust using these same SED fits. Finally, we can measure the number of photons absorbed through ionization by measuring Hydrogen recombination lines in HST narrow-band imaging assuming Case B recombination (e.g., Hummer & Storey 1987; Kennicutt 1998). Figure 2.1 describes how we estimate the ionizing photon escape fraction in our direction using individual stars within a galaxy. With these three measurements, we can create a map of f_{esc} for a galaxy with unprecedented spatial resolution.

Herein, we apply this technique to resolved photometry of NGC 4214, a metal-poor star-forming dwarf galaxy (see Figure 2.2). Such nearby analogs of high-z star-forming galaxies are excellent laboratories to study the star formation (SF) process, and the impact of stellar feedback on the interstellar medium (ISM) and the surrounding intergalactic medium

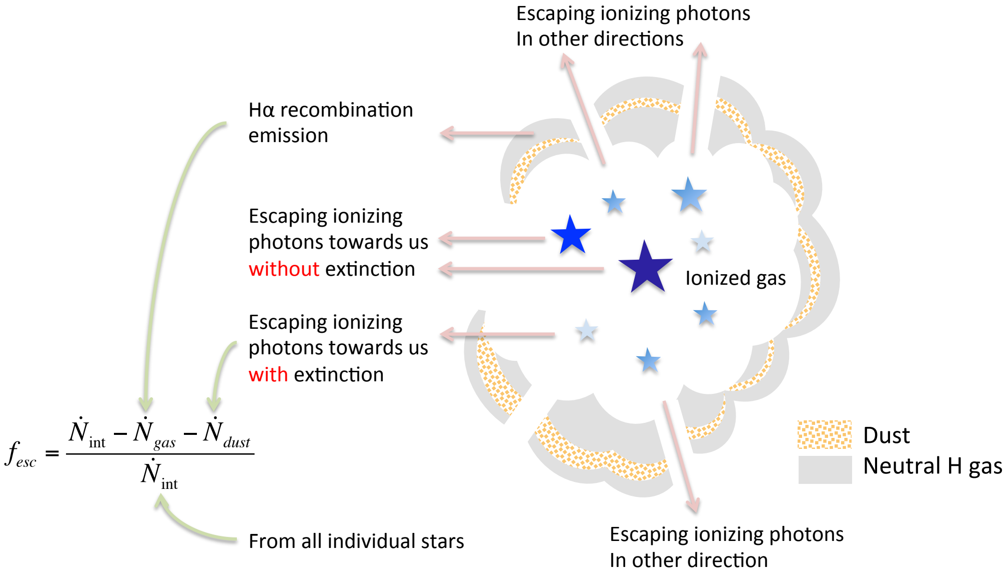

Figure 2.1 Schematic of our method of deriving the escape fraction of ionizing photons by measuring the numbers of (1) intrinsic ionizing photons ($\dot{N}_{\rm int}$), (2) ionizing photons consumed by neutral hydrogen ($\dot{N}_{\rm gas}$), and (3) ionizing photons absorbed by dust ($\dot{N}_{\rm dust}$).

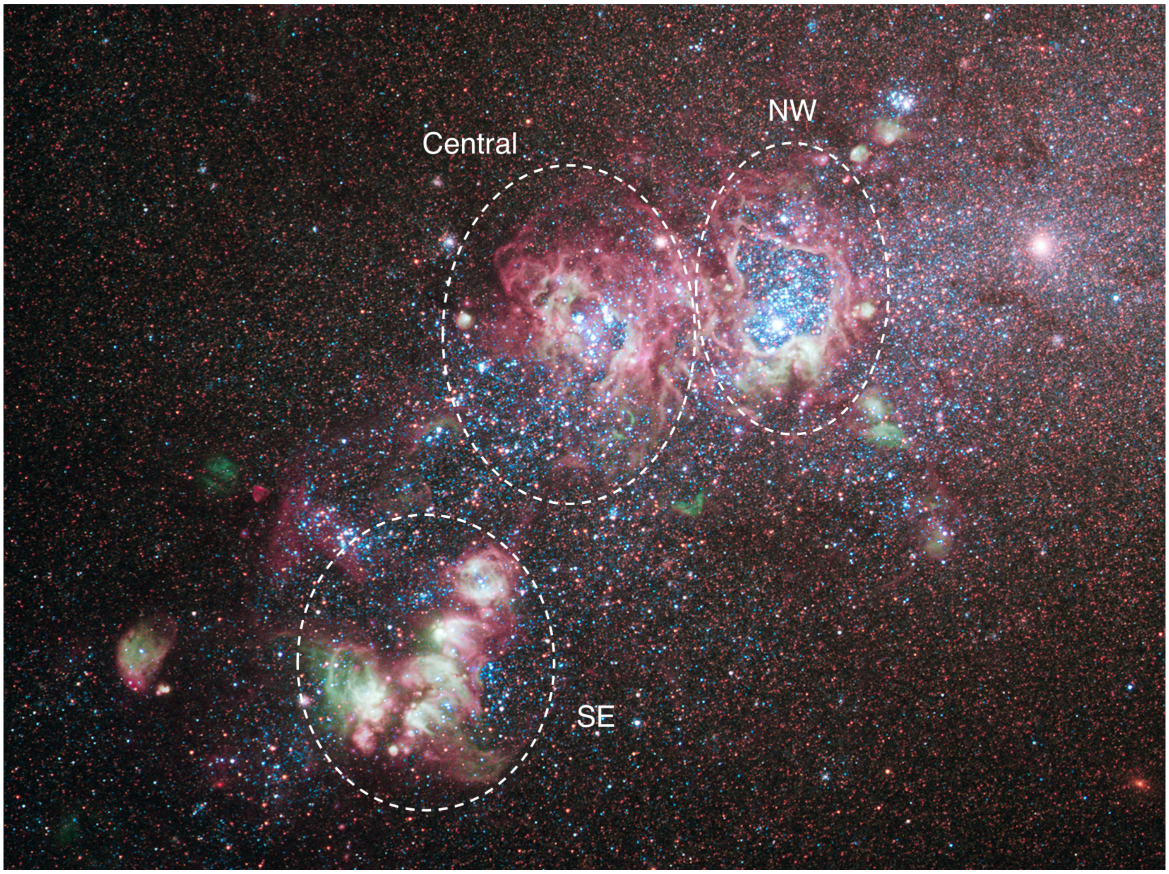

Figure 2.2 A composite image of NGC 4214 derived from HST/WFC3 data from GO-11360 (PI: OĆonnell). This image is a combination of red (F657N and F814W), green (F502N and F547M), and blue (F225W, F336W, F438W, and F487N) images. The morphology reveals many blue stars surrounded by expanding superbubbles. Credit: NASA, ESA, and the Hubble Heritage (STScI/AURA)-ESA/Hubble Collaboration.

(IGM). NGC 4214 is an especially appropriate galaxy to measure the escape fraction because of the presence of super bubbles in the galactic center.

There are three prominent star-forming complexes in NGC 4214 (SE, Central, and NW complexes as roughly marked in Figure 2.2), within which we expect most ionizing radiation to be produced. Enhanced star formation in these regions started ∼30 Myr ago (Williams et al. 2011), and the galaxy has a strong Wolf-Rayet feature in its spectrum (Kobulnicky & Skillman 1996), consistent with its high recent SFR. NGC 4214's total molecular gas mass is $M_{H2} = 5.1\times10^6\ M_\odot$ (Walter et al. 2001), the total atomic gas mass is $M_{HI} =$

4.1×10^8 $M_\odot$(Walter et al. 2008), and its stellar mass is $\sim1.5\times10^9$ $M_\odot$ (Karachentsev et al. 2004), making it a gas-rich dwarf galaxy. Its metallicity is low ($\sim$0.25 $Z_\odot$; Kobulnicky & Skillman 1996), similar to that of Small Magellanic Cloud. Its low metallicity results in the low dust content in NGC 4214. Hermelo et al. (2013) reported the gas-to-dust mass ratio of 350–470, which is 3.5–4.7 times higher than the Milky Way average value. Due to its proximity (3.04±0.05 Mpc; Dalcanton et al. 2009), NGC 4214 has been mapped in many wavelengths from the IR (e.g., with Spitzer and Herschel), through the optical (e.g., with HST), UV (e.g., with GALEX), and X-ray (Chandra). This large set of ancillary data for NGC 4214 enables one to probe its detailed ISM properties (e.g., MacKenty et al. 2000; Cormier et al. 2010; Hermelo et al. 2013) and its SFH using resolved stellar populations (e.g., McQuinn et al. 2010; Williams et al. 2011; Weisz et al. 2011). We adopt a distance of 3.04 Mpc (Dalcanton et al. 2009) and inclination of 44 degree (Walter et al. 2008). With this distance, an angular separation of $1''$ corresponds to 14.7 pc.

In Section 2.2, we begin with a brief overview of the HST imaging data, its photometry, and the ancillary data used in this work. In Section 2.3, we present a description of the Bayesian Extinction And Stellar Tool (BEAST), a probabilistic approach to modeling the dust extinguished photometric spectral energy distribution of an individual star while accounting for observational uncertainties common to large resolved star surveys. We also describe our specific BEAST settings for NGC 4214 in Section 2.4. Section 2.5 presents the fitting results for NGC 4214. In Section 2.7, we measure the both local and global escape fractions and discuss the implication for cosmic reionization and various effects in our escape fraction fraction measurement. We summarize our results and describe future work in Section 2.8.

2.2 Data and Photometry

2.2.1 Simultaneous 6-filter Photometry

We utilized *HST* images obtained with the WFC3/UVIS (F225W, F336W, F438W, and F814W bands) and WFC3/IR (F110W and F160W bands) cameras under the program GO-11360 (PI: O'Connell). The exposure times for F225W, F336W, F438W, F814W, F110W, and F160W are 1665s, 1683s, 1530s, 1339s, 1198s, and 2397s, respectively. The data is somewhat shallow, but sufficiently deep enough for our science goal, which focuses on massive O/B stars. Figure 2.2 shows a color image of NGC 4214 created from multi-wavelength HST/WFC3 data (program GO-11360; PI: O'Connell).

The resolved stellar photometry was derived as follows. First, cosmic rays (CRs) were identified in the WFC3/UVIS data by first running the IDL routine `lacosmic` on all of the UVIS data. Further CRs were identified by running `astrodrizzle` on data from each band with exposure times larger than 50 seconds.

Once the CRs were identified and flagged in the DQ extensions of the flt images, each image was processed through the DOLPHOT (Dolphin 2000) task `acsmask` or `wfc3mask` as appropriate. This task applies the DQ flags as well as the pixel area map to the flt SCI extensions in order to mask out bad pixels and CRs, and then calibrates the flux in each pixel by the area coverage on the sky. The flt images were then split into their individual CCDs using the DOLPHOT task `splitgroups`.

To simultaneously find and measure stars in all 6 bands, we first aligned all data to a relative precision of ∼0.2 pixel (8 milliarcseconds). We measured the positions of stars in each CCD of each exposure to provide the basis for astrometric alignment. These single CCD DOLPHOT catalogs were culled for artifacts using the same criteria as those used for the single camera photometry in Dalcanton et al. (2012). Once we produced catalogs for each individual CCD of each exposure, we used astrometry.net (Lang et al. 2010) to find the best alignment of all these catalogs. This software generated header update scripts that we applied to the original flc.fits images from MAST to produce astrometrically-aligned images from all visits in all bands.

With the original flt.fits images updated with the precision-aligned headers, we ran them all through the DOLPHOT preprocessing (`lacosmic`, `astrodrizzle`, `wfc3mask`, `calcsky`), to prepare to run the final photometry. We used the F438W `astrodrizzle` output as the DOLPHOT reference image for astrometry. Our final alignment to the F438W astrodrizzled reference image, as measured by DOLPHOT, had an rms scatter of 0.3 pixels or better in all of the IR exposures and 0.2 pixels or better in all of the UVIS exposures.

The output of DOLPHOT includes all $> 3.5\sigma$ peaks in the full data set. It therefore accounts for flux from neighbors as precisely as possible, but also contains many measurements that are due to artifacts (warm pixels, poorly-masked CRs) or noise. We therefore culled the catalogs based on quality parameters measured by DOLPHOT. In particular, in each band, we only accept measurements with a signal-to-noise > 4, a sharpness^2 < 0.15, and crowding < 1.3 (2.25) for the WFC3/UVIS (WFC3/IR). These cuts produced sharp-featured CMDs of accepted stars. In our final catalog, there are about 83,000 resolved stars that are detected in at least 4 bands. We refer the reader to Williams et al. (2014) for details of comparable simultaneous 6-filter photometry for the PHAT data set.

Figure 2.3 presents the optical CMDs of stars that are detected in 6 bands (left; 9,366 stars), 5 bands (middle; 12,323 stars), and 4 bands (right; 61,242 stars). Over 98% stars in our final catalog appear on these optical CMDs. Stars that are detected in all 6 bands are mostly blue and bright, whereas stars that are detected in 4 bands are fainter and redder. Even for the blue (F438W–F814W < 1 mag) stars, the brightest stars with 4-band detections are $\sim$2 mag fainter than those with 6-band detections. Stars with 5-band detections occupy the middle position on the CMD. In the CMD of 4-band detection stars, there are two clusters of stars: one at F438W–F814W < 1 mag, and the other at F438W–F814W > 1 mag. The bluer cluster consists of stars with 4-band detections in the UV and the optical filters (red solid contours), while the majority of stars in the redder cluster are detected in the optical and the IR filters (cyan dashed contours).

2.2.2 Ancillary Data

In addition to the HST broad-band imaging data, we used narrow-band images of Hα (F657N) and Hβ (F487N) lines (also from GO-11360; PI: O'Connell) to derive an extinction-corrected Hα map. To derive this map, we first subtracted scaled continuum images in the appropriate filters (F814W and F438W, respectively) from drizzled Hα and Hβ emission images. We also accounted for the [NII] contribution using a measured [NII]/Hα ratio of 0.117 for NGC 4214 (Kobulnicky & Skillman 1996). We then combine these continuum-subtracted emission images to calculate an extinction map using the Balmer decrement Hα/Hβ, and correct the Hα emission-line map for extinction. The extinction-corrected Hα

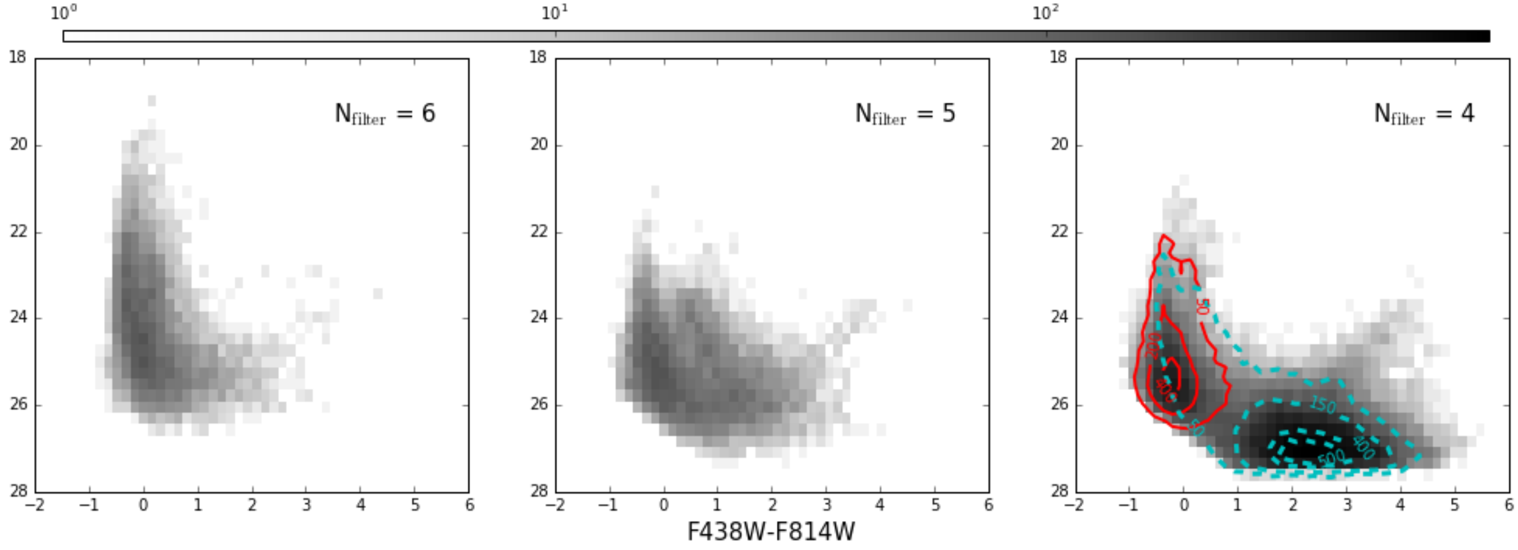

Figure 2.3 The optical CMDs of stars that are detected in 6 bands (left; 9,366 stars), 5 bands (middle; 12,323 stars), and 4 bands (right; 61,242 stars). In the right panel, we also show the distribution of stars with 2 UV and 2 optical detections (red solid contours). These stars occupy the blue (F438W–F814W < 1 mag) part the CMD. On the other hand, stars with 2 optical and 2 NIR detections dominate the red (F438W–F814W > 1 mag) part of the CMD (dashed blue contours).

map is used to estimate the number of ionizing photons consumed by photoionization in the surrounding ISM (see Section 2.7). We also use the GALEX FUV image (GI4-095, PI: Lee) to compare with the predicted FUV map derived from stellar SED fitting. Figure 2.4 shows the Hα (F657N), Hβ (F487N), and GALEX FUV images.

2.3 THE BEAST: Bayesian Extinction And Stellar Tool

The BEAST was originally developed by M. Fouesneau, and has been heavily updated by K. D. Gordon for the PHAT dataset and myself for the NGC 4214 dataset. K. D. Gordon is the leading author of the BEAST technical paper (Gordon et al. 2016), and I am a co-author of the paper.

We have developed a probabilistic tool for broad stellar SED fitting, called BEAST (Gordon et al. 2016). The the BEAST fits libraries of stellar model SEDs with dust extinction to the observed broad-band SEDs of individual stars. We can, therefore, fit multi-wavelength photometry of individual stars simultaneously for both the stellar properties (e.g., age, mass, metallicity) and the intervening dust properties (column density, composition, and grain size distribution). This is possible because the shape of stellar SED covering the UV to IR responds to dust and stellar temperature in different ways, with the UV filters, in particular, being essential to breaking the degeneracy between dust absorption and stellar temperature.

Therefore, by running the BEAST on multi-wavelength photometry of resolved stellar populations, we can infer the intrinsic model emission for each bright star in any bandpass, allowing us to create a high resolution map of the intrinsic ionizing photon production rate. In this section, we describe how we infer the intrinsic properties of individual stars and intervening dust from the stellar SED fitting technique in more detail.

The BEAST is optimized for large multi-wavelength surveys of resolved stellar populations. Full detailed description of the BEAST can be found in Gordon et al. (2016), which shows that the application of the BEAST to the PHAT survey dataset (Dalcanton et al. 2012; Williams et al. 2014) is successful, in that the results yield a reasonable Hertzsprung-Russell (HR) diagram, understandable variations in fit parameter precision, and a spatial map of the average dust column that correlates well with existing infrared derived dust

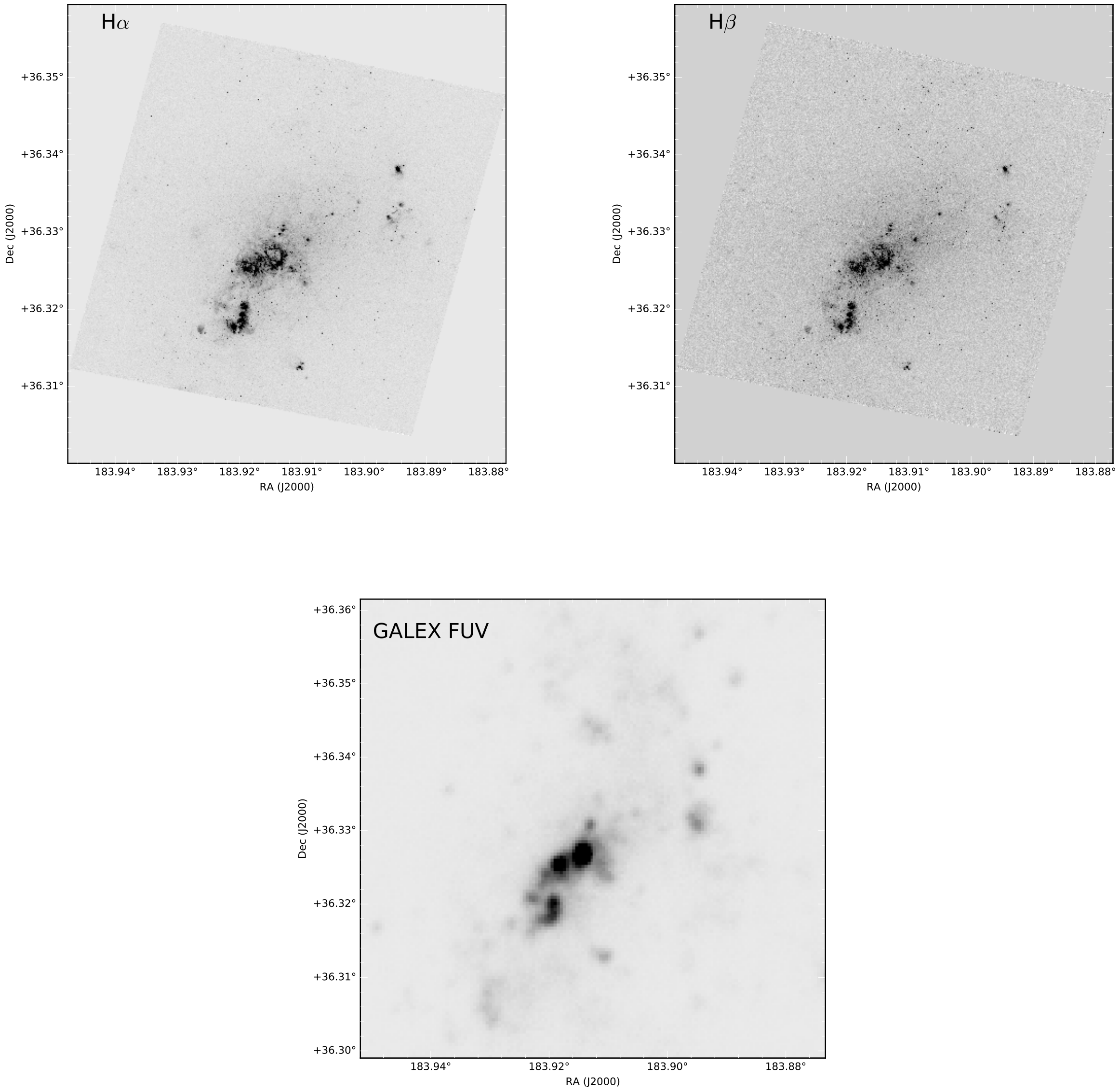

Figure 2.4 Ancillary Data for NGC 4214. Top: the narrow-band images of Hα (F657N) and Hβ (F487N) lines from the program GO-11360 (PI: O'Connell). Bottom: the GALEX FUV image (GI4-095, PI: Lee).

surface densities (Draine et al. 2014). While the BEAST has been originally developed for the PHAT survey, it is applicable to any multi-wavelength resolved star surveys, including the NGC 4214 dataset, with appropriate priors.

2.3.1 Fitting Technique

Bayesian inference enables us to constrain the model parameters (i.e., posterior probability distribution function, pPDF) given the multi-wavelength flux measurements (F_D) as

$$P(\theta \,|\, F_D) \propto P(F_D \,|\, \theta)\, P(\theta), \tag{2.1}$$

where $P(\theta)$ is the prior distribution, which reflects our prior-knowledge of physical models (θ) and observational data, and $P(F_D \,|\, \theta)$ is the likelihood function. The likelihood function is written using a multivariate Gaussian distribution as follows.

$$P(F_D \,|\, \theta) \;=\; \frac{1}{Q(\theta)}\,\exp\left(-\frac{1}{2}\chi^2(\theta)\right), \tag{2.2}$$

where $Q^2(\theta) \;\equiv\; (2\pi)^N \det|\mathbb{C}(\theta)|$. $Q(\theta)$ is the normalization term describing the full noise model. $\mathbb{C}(\theta)$ is a $N \times N$ covariance matrix of the N photometric bands (i.e., correlations between bands), including photon noise, flux bias due to stellar crowding, and absolute flux calibration uncertainties:

$$\mathbb{C}(\theta) = \mathbb{C}_P(\theta) + \mathbb{C}_\mu(\theta) + \mathbb{C}_C(\theta). \tag{2.3}$$

Thus, our $\chi^2(\theta)$ equals $\Delta^T \mathbb{C}(\theta)^{-1} \Delta$, where $\Delta = F_D - F_M(\theta) + \mu(\theta)$. $F_M(\theta)$ is the multi-wavelength model flux and $\mu(\theta)$ is the corresponding flux bias due to crowding. This $\chi^2(\theta)$ becomes the standard $\chi^2(\theta)$ if assuming independent measurements between bands, which is not realistic.

We take a grid-based approach in the BEAST fitting to explore the full model parameter space θ. With realistic sampling of the model grid, this approach is more efficient than a Monte Carlo Markov Chain (MCMC) or nested sampling approach. It also allows us to avoids the computationally intensive normalizations needed for MCMC results.

2.3.2 Stellar model

We construct our stellar model grid by mapping stellar atmospheric properties on to their evolutionary models. This choice maps each stellar evolutionary models (defined by stellar mass M, stellar age t, and metallicity Z) on to a stellar atmosphere model (defined by stellar effective temperature $T_{\rm eff}$, surface gravity $\log(g)$, and metallicity Z). Thus, (M, t, Z) is our primary set of stellar parameters, denoted $\theta_{\rm star} = \{M, t, Z\}$. A stellar model SED for a given stellar mass (M), age (t), and metallicity (Z) is

$$L_\lambda(M,t,Z) \;\; = \;\; 4\pi\, R^2(M,t,Z) \times\, S_\lambda(T_{\rm eff}, \log(g), Z)\,,$$

where R is the stellar radius and S_λ is the surface flux density. In this BEAST, we use the PARSEC evolutionary tracks (Bressan et al. 2012) and the merged stellar atmosphere model of the local thermal equilibrium (LTE) grid from Castelli & Kurucz (2004) and the non-LTE TLusty OSTAR and BSTAR grid from Lanz & Hubeny (2003, 2007) for hot stars (see Figure 2 in Gordon et al. 2016). The shortest wavelength in our final model SED is 90Å. As one of the future improvements, we will expand the BEAST stellar model by adding other stellar atmosphere models to cover a wider range of stars (e.g., Westera et al. 2002; Bergemann et al. 2012; Rauch et al. 2013), and using newer stellar evolutionary tracks (e.g., Rosenfield et al. 2016).

2.3.3 Dust model

A successful model of an observed stellar SED requires modeling emission spectra of stars as well as absorption spectra of the intervening dust. Emergent light from a star is extinguished by interstellar dust before reaching to the observer. The degree to which the emergent light is extinguished is a strong function of wavelength. Extinction curves from the FUV to the NIR have been measured along many sightlines in the Milky Way (MW) (Cardelli et al. 1989; Fitzpatrick 1999; Valencic et al. 2004; Gordon et al. 2009), as well as in the Magellanic Clouds (Gordon & Clayton 1998; Misselt et al. 1999; Maíz Apellániz & Rubio 2012) and M31 (Bianchi et al. 1996). Most sight-lines in the Magellanic Clouds behave very differently than in the Milky Way $R(V)$-dependent relationship (Gordon et al. 2003). For example, the extinction curves in the Small Magellanic Cloud (SMC) star-forming bar show nearly linear dependence on λ^{-1}. Also, there is no strong 2175 Å extinction bump in the extinction curves of the SMC star-forming bar.

It has been found that the observed extinction curves in the Local Group lie between the average MW extinction curve (e.g., Cardelli et al. 1989; Fitzpatrick 1999) and the average SMC star-forming bar extinction curve (Gordon et al. 2003). Thus, Gordon et al. (2016) introduced a mixture model that effectively interpolates between a Milky Way extinction model ("$\mathcal{A}$" component) and a SMC Bar extinction model ("$\mathcal{B}$" component). The mixture model is

$$k_\lambda(R(V), f_\mathcal{A}) = f_\mathcal{A} \left[\frac{A(\lambda)}{A(V)}\right]_\mathcal{A} + (1 - f_\mathcal{A}) \left[\frac{A(\lambda)}{A(V)}\right]_\mathcal{B}, \tag{2.4}$$

where $A(V)$ is the extinction in magnitudes in the Johnson V band, $f_\mathcal{A}$ gives the fraction of the $\mathcal{A}$-type extinction, and thus $(1 - f_\mathcal{A})$ the fraction of the $\mathcal{B}$-type extinction. The $R(V)$ of the mixture extinction curve model is given by

$$R(V)^{-1} = f_\mathcal{A} R_\mathcal{A}(V)^{-1} + (1 - f_\mathcal{A}) R_\mathcal{B}(V)^{-1}, \tag{2.5}$$

where we fix $R_\mathcal{B}(V) = 2.74$ (Gordon et al. 2003). Our primary set for dust model parameters is $\theta_\text{dust} = \{A(V), R(V), f_\mathcal{A}\}$.

By applying the dust mixture model into an unextinguished SED (Equation 2.4), we can obtain a model monochromatic flux (F_λ^Mod) of a star at a distance d as follows:

$$F_\lambda^\text{Mod}(\theta) = \frac{L_\lambda(\theta_\text{star})\, 10^{-0.4\, A(V)\, k_\lambda(R(V), f_\mathcal{A})}}{4\pi d^2} \tag{2.6}$$

where

$$\begin{aligned} \theta &= \{\,\theta_\text{star}, \theta_\text{dust}, d\,\} && (2.7) \\ &= \{M, t, Z, A(V), R(V), f_\mathcal{A}, d\}. && (2.8) \end{aligned}$$

The fundamental principle of the SED fitting is to compare these model fluxes with photometric observations. Figure 2.5 gives a graphical representation of how the model SEDs are computed showing the intrinsic spectrum, the effects of dust, the extinguished spectrum, and the band integrated SED. However, the actual SED fitting process involves more complexities, which we discuss in the next two subsections.

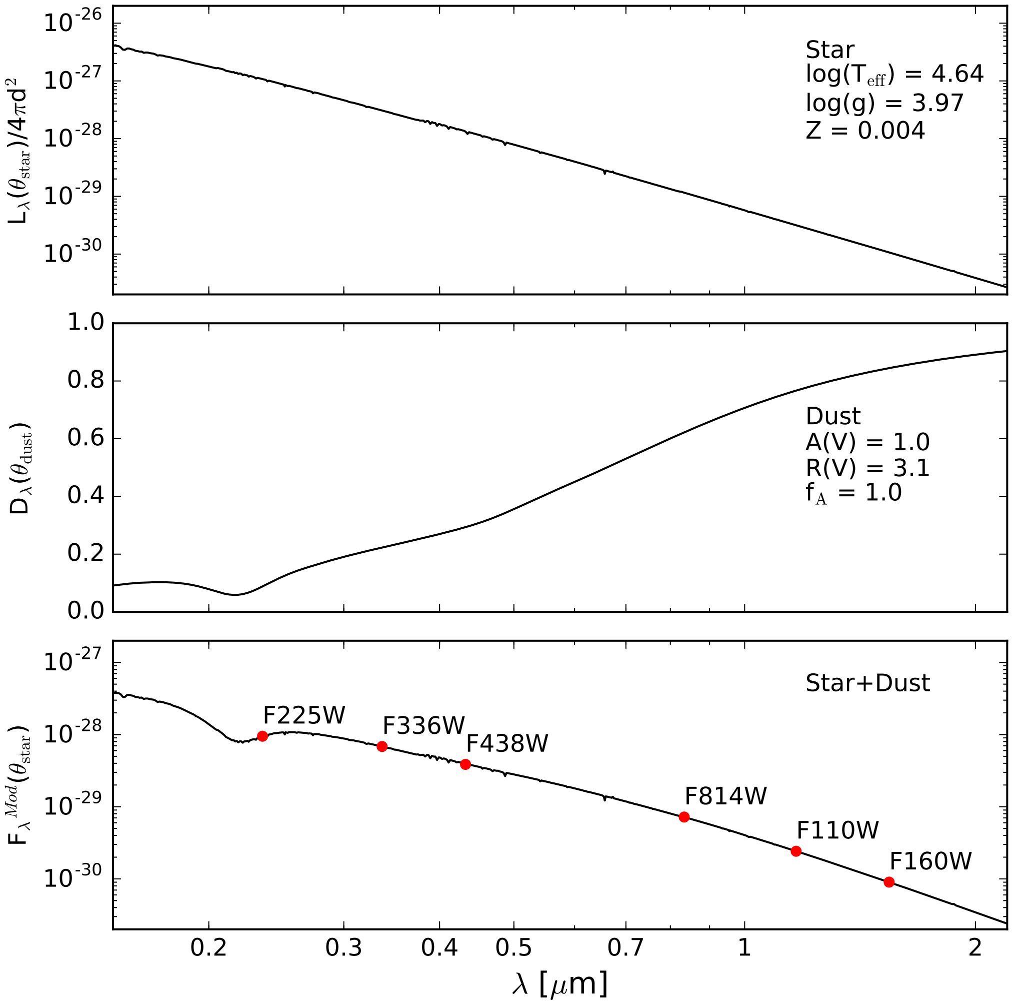

Figure 2.5 The computation of a BEAST model SED for a dust extinguished star is shown graphically. The top panel gives the stellar spectrum, the middle panel shows the extinction by dust, and the bottom panel plots the full extinguished stellar spectrum. As an example, we show the integrated SEDs for the 6-filter bandpasses (solid circles) in the bottom panel.

2.3.4 Priors

The BEAST SED fitting includes the options of using prior distributions on the parameters of the set of stellar and dust models. When parameters are well understood, we specify physically motivated priors to improve the statistical accuracy of the fitting, particularly in the limit of noisy data. Our well-established knowledge about the stars and dust in a galaxy from previous studies generally serve as a good approximation to what our posterior beliefs should be. For example, it is known that a stellar initial mass function (IMF) favors the production of low mass stars (see the review of Bastian et al. 2010), resulting in more low mass stars. To reflect the expected distribution of real stars, we can select proper priors on stellar mass and age to be consistent with a given initial mass function and SFH, and apply those priors to the model grid points by assigning corresponding weights. Figure 2.6 shows an example of mapping of the stellar mass and age priors into the $\log(T_{\rm eff})$ versus $\log(L)$. We note that the resulting posterior distribution follows the prior distributions in case of low signal-to-noise measurements.

2.3.5 Noise Model

Another virtue of a successful SED modeling includes appropriate modeling of observational effects. Observational uncertainties of stars in external galaxies result from a combination of photon noise and crowding. To properly account these observational effects in our SED fitting, we construct a full observational "noise model" by performing extensive artificial star tests (ASTs).

Specifically, we construct the full noise model for individual dust-reddened stellar models by running N-filter ASTs. We insert a single artificial star with a known SED into the observed image and re-run photometry in the same way we did for real stars. We repeat this many times to draw statistical information for each model. These ASTs capture complexities due to the non-linear interaction between the photon and crowding noise, allowing us to generate a noise model describes the differences between the input and output magnitudes in all filters (Equation 2.9), and the covariances between the offsets in different filters (Equation 2.10). The noise model describes correlations between filters as a covariance

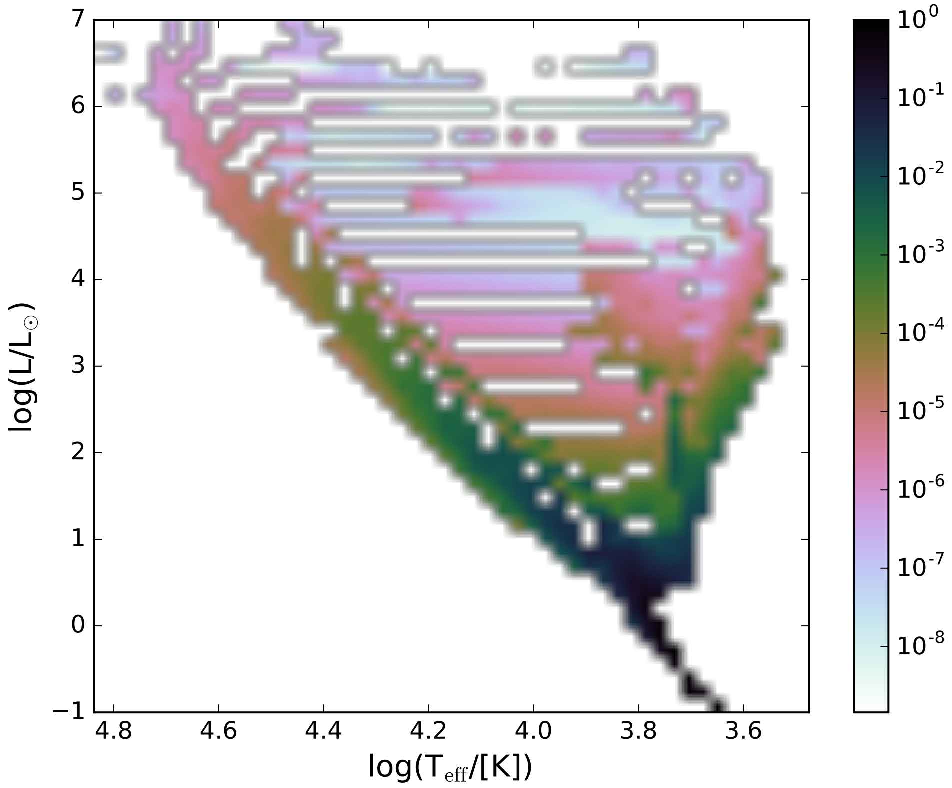

Figure 2.6 An example of mapping of the stellar mass and age priors into the $\log(T_{\rm eff})$ versus $\log(L)$. Darker (lighter) colors denote higher (lower) prior probabilities.

matrix $\mathbb{C}(\theta)$.

The bias $\mu_i(\theta)$, describing combined photon and crowding noise, in a given band i is

$$\mu_i(\theta) = \frac{1}{N} \sum_k \left(F^k_{R,i} - F_M(\theta) \right), \tag{2.9}$$

and the covariance between bands i and j is

$$\mathbb{C}^2_{ij}(\theta) = \frac{\sum_k^N \left(\mu^k_i - \langle \mu_i(\theta) \rangle\right) \left(\mu^k_j - \langle \mu_j(\theta) \rangle\right)}{N-1}, \tag{2.10}$$

where F^k_R are recovered fluxes of N realizations and $F_M(\theta)$ is an input model flux. If one assumes that different bands are independent, the off-diagonal terms are equal to zero. Gordon et al. (2016) show that including the covariance in the SED fitting improves accuracy and precision. We also include the absolute flux calibration for the given filter sets following Bohlin et al. (2014). We refer the reader to Gordon et al. (2016) and Bohlin et al. (2014) for further details.

2.4 The BEAST Settings for NGC 4214

In this section, we discuss applying the BEAST to NGC 4214; NGC 4214 has very different physical conditions from M31, and thus the proper priors on the stellar, dust, and noise models should be different from those presented in Gordon et al. (2016) for M31. We also modify the dust model below the FUV to X-ray, where the normal BEAST extinction curves based on observational data cannot be applied correctly.

2.4.1 Stellar Model

In this study, we specifically use the updated PARSEC evolutionary tracks (Tang et al. 2014) that fully describe massive stars (up to 350 $M_\odot$) for low metallicity ($0.001 \leqslant Z \leqslant 0.004$). As we discuss in Section 2.3.2, we map the stellar atmospheric properties onto this stellar evolutionary model. The coverage of our stellar model on the parameter space ($\log(T)$, $\log(L)$, $\log(g)$, and $\log(M_{\rm ini})$) is shown in Figure 2.7.

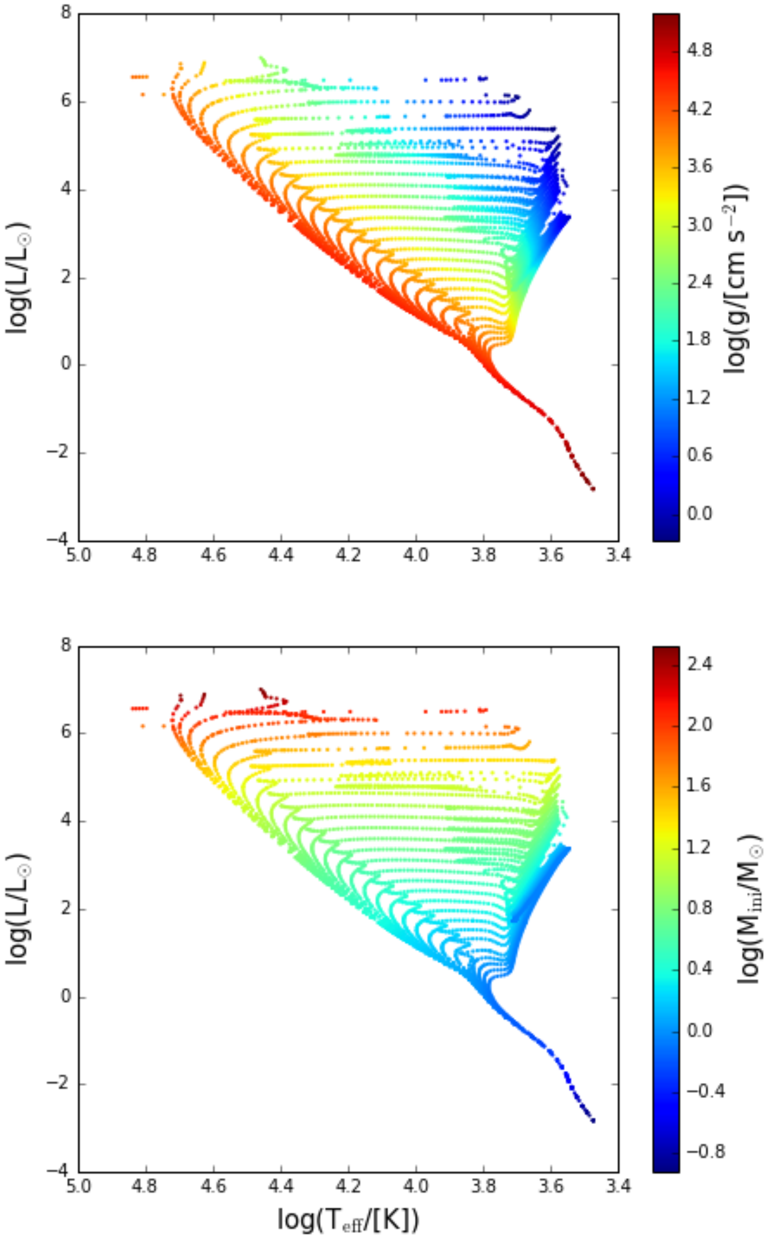

Figure 2.7 The coverage of the stellar model used in the BEAST is shown in a Hertzsprung-Russell diagram color-coded by $\log(g)$ and $\log(M_{\rm ini})$.

2.4.2 Dust Model

The BEAST utilizes the mixture dust model, constructed from well-sampled FUV to NIR observations. However, inferring the absorption of LyC photons requires knowledge of the extinction curves in the extreme UV, where there is currently no observational data. Rather than simply extrapolating the extinction curve to short wavelengths (which produces a steep rise in extinction to short wavelengths as seen in Figure 2.8), we adopt theoretical extinction curves below the Lyman limit, using curves from Weingartner & Draine (2001) and Draine (2003). This carbonaceous-silicate grain model successfully reproduces observed interstellar extinction, scattering, and infrared emission (Li & Draine 2001). We obtain the $R(V)$-dependent model extinction curves with $2 \leq \mathrm{Rv} \leq 6$ by extrapolating and interpolating the theoretical MW extinction curves provided for $R(V)$ values of 3.1, 4.0, and 5.5. To merge the theoretical curves onto the BEAST extinction curves between 912 Å $< \lambda <$ 1695 Å, where the observational uncertainty is significant (Fitzpatrick 1999), we compute a weighted mean between the curves. The weight linearly varies on the BEAST curves from zero at 912 Å to one at 1695 Å. The opposite weight for the theoretical extinction curves is applied. Performing the weighted average produces a smooth transition from the BEAST to the model curves. We repeat the same process for the SMC Bar extinction curve with a fixed $R(V)$ of 2.74 as well.

2.4.3 Priors

We construct prior distributions on the parameters of the set of stellar models that are suitable for NGC 4214. In addition to the BEAST's standard prior distributions (Section 2.3.4), we put much stronger priors on a number of other parameters that are well known. These include the distance to NGC 4214 (3.04 Mpc: Dalcanton et al. 2009), the Milky Way foreground extinction ($A(V) = 0.06$ mag; Schlafly & Finkbeiner 2011), and metallicity ($Z = 0.004$, which appears not to vary across the galaxy; Kobulnicky & Skillman 1996). While the older stars may have a different metallicity, it is a reasonable to assume that the youngest stars have metallicity comparable to what is seen in the surrounding HII regions. For the internal dust, we assume uniform priors on $A(V) =$ between 0.0 and 8.0, and on $R_{\mathcal{A}}(V)$

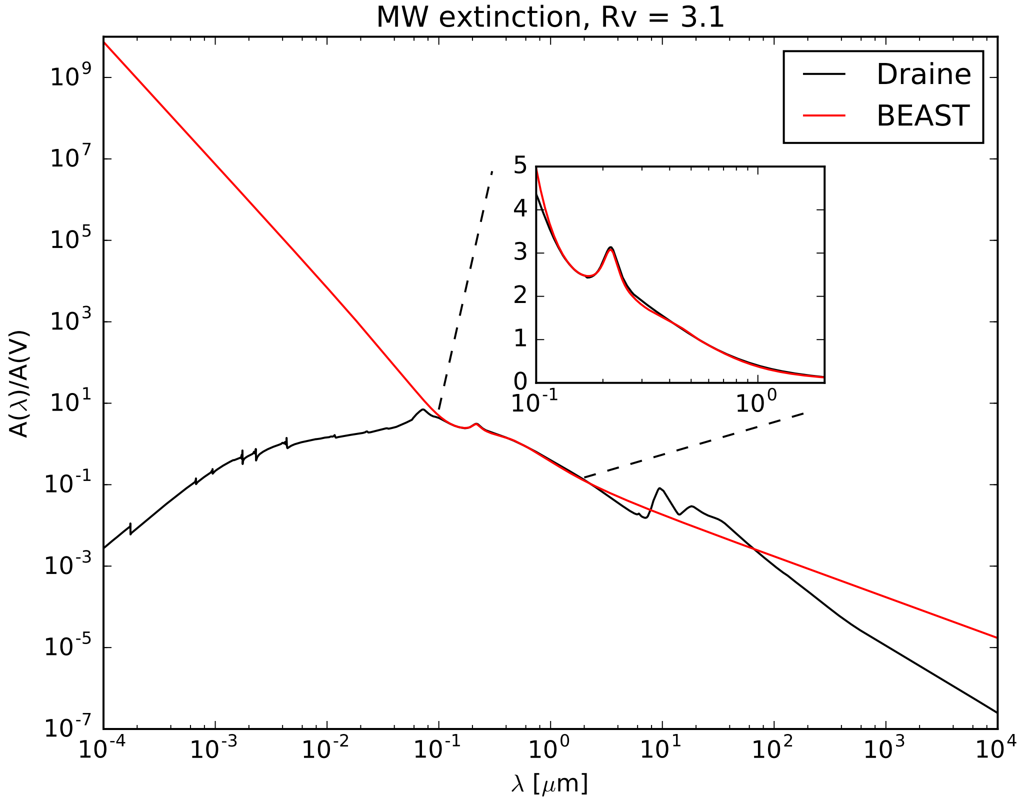

Figure 2.8 Below the Lyman limit, the behavior of the original BEAST extinction curves, which based on observations at wavelengths longer than FUV, is obviously different from the model extinction curves (Weingartner & Draine 2001; Draine 2003). The BEAST extrapolates the extinction curves at wavelengths shorter than FUV, where there is no available observational data. This results in the unphysical rise in the extinction curves towards the Lyman continuum regime. On the other hand, the model extinction curves increase smoothly as wavelength decreases, peak at around 750 Å and then decrease. Thus, we modify the BEAST curves to adopt the Draine curves below the 912 Å. Our final extinction curves have three regimes: (1) the original BEAST curve only regime ($\lambda > 1695$ Å), (2) the transition regime from the BEAST curve to the model curve (912 Å $< \lambda < 1695$ Å), and (3) the model curve only regime ($\lambda < 912$ Å).

between observed values 2.0 and 6.0. Finally, we use a binary fraction of 0.3, and select priors on stellar mass and age to be consistent with a Kroupa IMF (Kroupa 2001) with a constant SFH.

2.4.4 Noise Model

The properties of the noise model depend strongly on stellar number density, given that crowding usually dominates over photometry uncertainties. We therefore compute the noise model in bins of stellar number density, which we define as the number of stars per arcsec^2. This density is calculated based on 20 nearest neighbors using only stars with 20 mag $<$ F438W $<$ 24 mag, for which detections are highly complete in F438W. Figure 2.9 presents the resulting stellar number density map for NGC 4214. Using this map, we calculate the noise model in eight stellar number density bins between 0 and ∼33 stars per arcsec^2, logarithmically spaced.

For each stellar number density bin, we sample the input fake stars from the model SED grid to guarantee that the noise model is calculated for realistic populations of stars. First, we trim the model grid to only keep the models with fluxes $> 0.2\times\mathrm{flux}_{\mathrm{min,obs}}$ in at least four bands. This choice removes models that are too faint to be detected in our observations, saving computational time. This trimming removes models with bolometric luminosities fainter than ∼3.16 $L_\odot$. Note that by including models with 5 times fainter than the observed faintest stars, we are able to account for up scattering of faint stars. We select ∼630 unique model SEDs, which cover the entire parameter space of interest uniformly (see Figure 2.10). We require 20 independent realizations for each fake star to have a reasonably well measured mean offset between the true and measured fluxes. The equal number of fake stars in each stellar number density bin ensures the same quality of noise model at all stellar number density ranges. In total, we use 100,800 ASTs (= 8×630×20) to construct the full noise model for individual dust-reddened stellar models by running *simultaneous* 6-filter ASTs. We then interpolate to the noise model for arbitrary stellar models. In our noise model, we also take the full covariance and the model-independent absolute flux calibration into account .

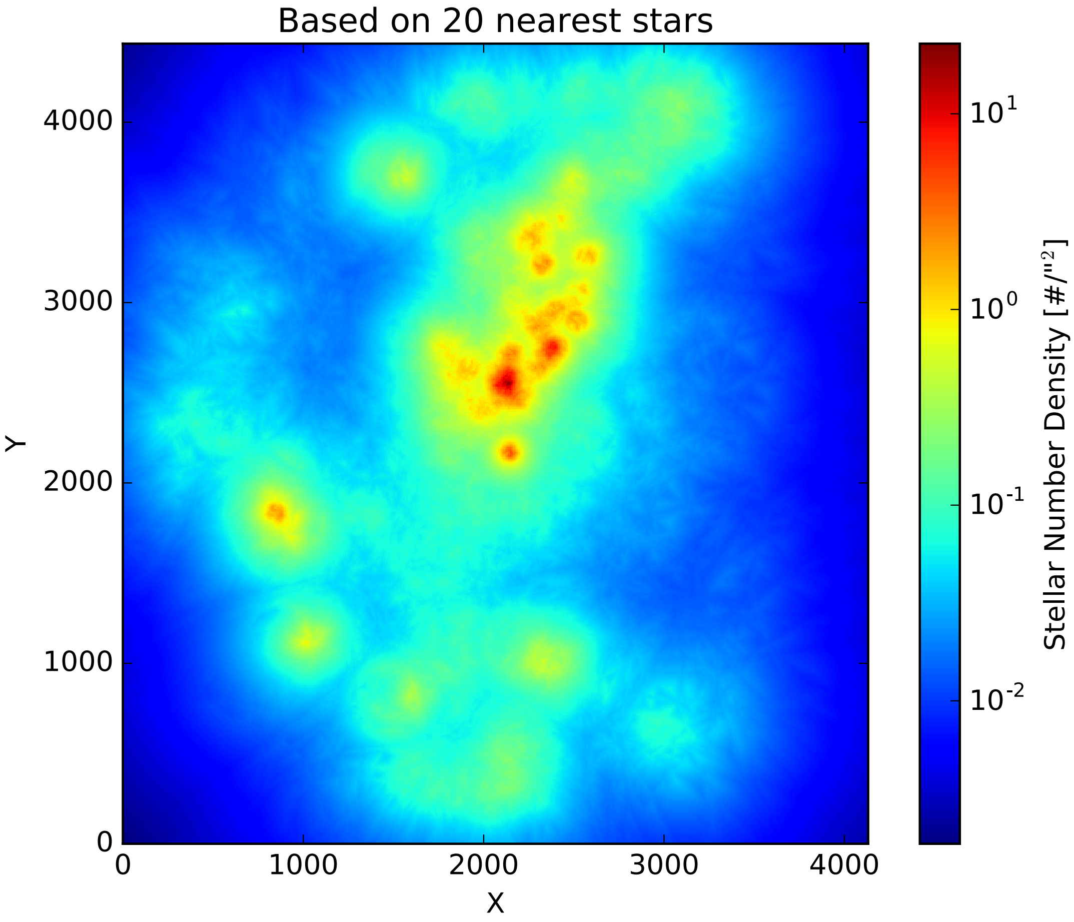

Figure 2.9 The stellar number density map based on 20 nearest neighbors. We only use stars with 20 mag < F438W < 24 mag, over which the detection is complete in F438W.

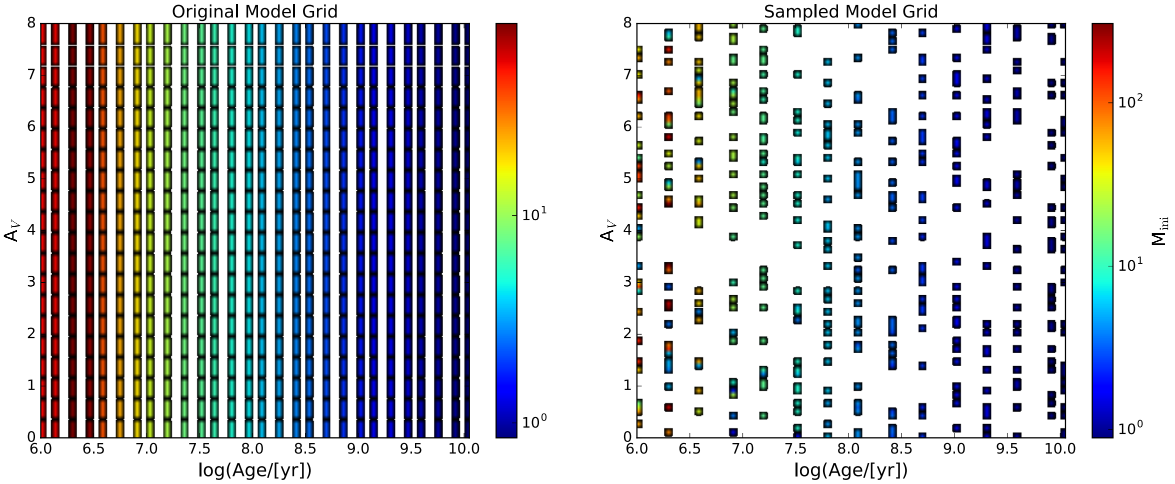

Figure 2.10 The left panel shows the stellar age and $A(V)$ distribution of our original model grid. The right panel shows the stellar age and $A(V)$ distribution of the selected model grid, color-coded by stellar initial mass. From the original model grid, we uniformly sample the fake stars to make sure that we search for the entire stellar parameter space.

2.5 Results

Figure 2.11 shows an example of the BEAST SED fitting for a massive young star in NGC 4214 (36 $M_\odot$ and 3.5 Myr). In the top panel, solid circles are observations and the colored lines show the 50th percentile models; blue dashed line, green solid line, and red thick line represent the stellar only model, stellar with dust model, and stellar with dust including the observational bias model, respectively. The shaded envelope indicates the 68% confidence interval of the full model (i.e., stellar+dust+bias). The impact of the bias in the photometric measurements is clearly seen in the IR and illustrates the importance of a full physical and observational model for this type of fitting.

In the bottom panels, we show the 1D posterior PDFs for $A(V)$, log(M$_{\rm ini}$), log(t), and log($T_{\rm eff}$) parameters. This star is fit as a massive young star without any confusion. The 50%±33% values of each parameter are given numerically as well as graphically (magenta lines) in the 1D pPDF plots. In the following figures and analysis, we report 1σ uncertainties for each parameter, estimated from the 16th and 84th percentile values. Table 3.1 describes all columns in our catalog. The full catalog is available in FITS format from MAST[1].

In Figure 2.12, the left two panels show color-magnitude diagrams (CMDs) color-coded by the expectation values for $\log(T_{\rm eff})$ and $A(V)$. One can see that bright, blue main-sequence (MS) stars have high effective temperature while faint MS stars and red giant branch (RGB) stars have lower effective temperature, as expected. In general, about 81% of stars in NGC 4214 show low dust extinction ($A(V) < 1$ mag), as expected for a low-metallicity system. However, there are some intrinsically hot, but significantly extincted ($A(V) > 1.5$ mag) stars, which is also expected for young stars that are still partially embedded in their nascent molecular clouds. These stars move along the reddening vector on the CMD and show up at the redder, fainter part of the MS.

The right two panels in Figure 2.12 show 1σ uncertainties for each parameter. Uncertainty in $\log(T_{\rm eff})$ is low (< 0.1 dex) at most temperatures, except for the range between $3.8 < \log(T_{\rm eff}) < 4.2$. This temperature range suffers most from the degeneracy between the dust and stellar temperature (Romaniello et al. 2002). In this temperature range, even stars that have the identical dust-free color can map into several different stellar temperatures (see Figure 6 in Romaniello et al. 2002). For this study, the lowest temperature of interest is ∼30,000 K, corresponding to B0 spectral type stars, which is about two times higher than $\log(T_{\rm eff})$ of 4.2, and thus well outside the range of significant temperature uncertainties.

Uncertainty in $A(V)$ is larger than that in $\log(T_{\rm eff})$. In particular, fainter stars tend to suffer from high uncertainties in $A(V)$. Among cool stars with $\log(T_{\rm eff}) < 3.8$, ∼45.6% of them report high fractional uncertainty in $A(V)$ ($> 30\%$), while they still show low absolute uncertainties in $\log(T_{\rm eff})$. We found that these cool (or faint) stars are not detected in the UV, making it hard to constrain the dust column density. When we include the stars with $3.8 < \log(T_{\rm eff}) < 4.2$, which show significant $\log(T_{\rm eff})$ uncertainties (> 0.1 dex), this percentage increases up to 72.5%.

Fortunately, massive young stars suffer less from large uncertainties in $A(V)$, because most of them are detected in all 6 filters. Furthermore, their median $A(V)$ value is ∼0.5 mag, thus even with $> 30\%$ fractional uncertainty one can avoid significant absolute uncertainties

---

[1] http://address

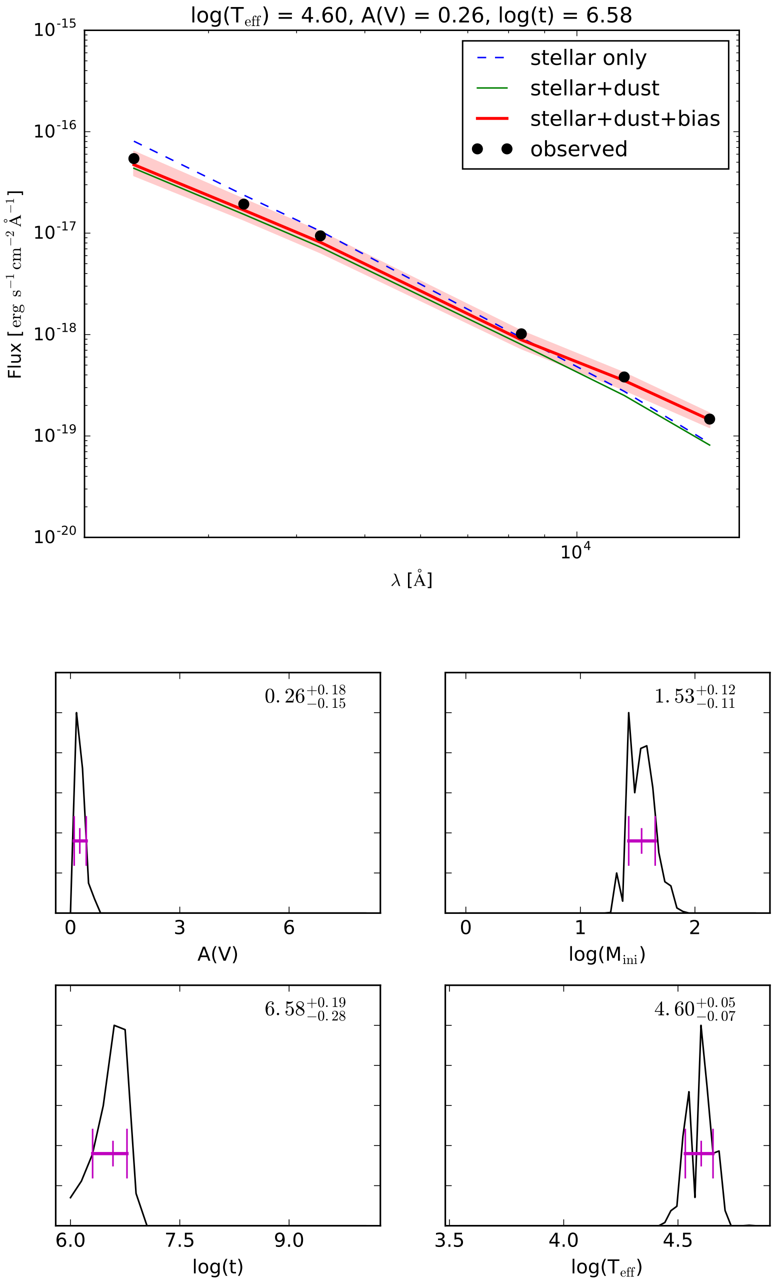

Figure 2.11 The fitting results for an individual star in NGC 4214 are shown. While this figure illustrates the fit to an individual source, it is for a hot main-sequence star that is the sources of interest. The 50th percentile model is shown along with shaded colored regions indicating the range of models that fit within 1σ. The models shown are the full model including the observational bias (stellar+dust+bias), the physical model alone (stellar+dust), and the stellar model alone (stellar). The impact of the bias in the photometric measurements is clearly seen in the IR and illustrates the importance of a full physical and observational model for this type of fitting. The 50%±33% values are given numerically as well as graphically in the 1D pPDF plots. The 1D pPDF plots give the normalized probabilities ranging from 0 to 1, but the y-axis scale ranges from 0 to 1.2.

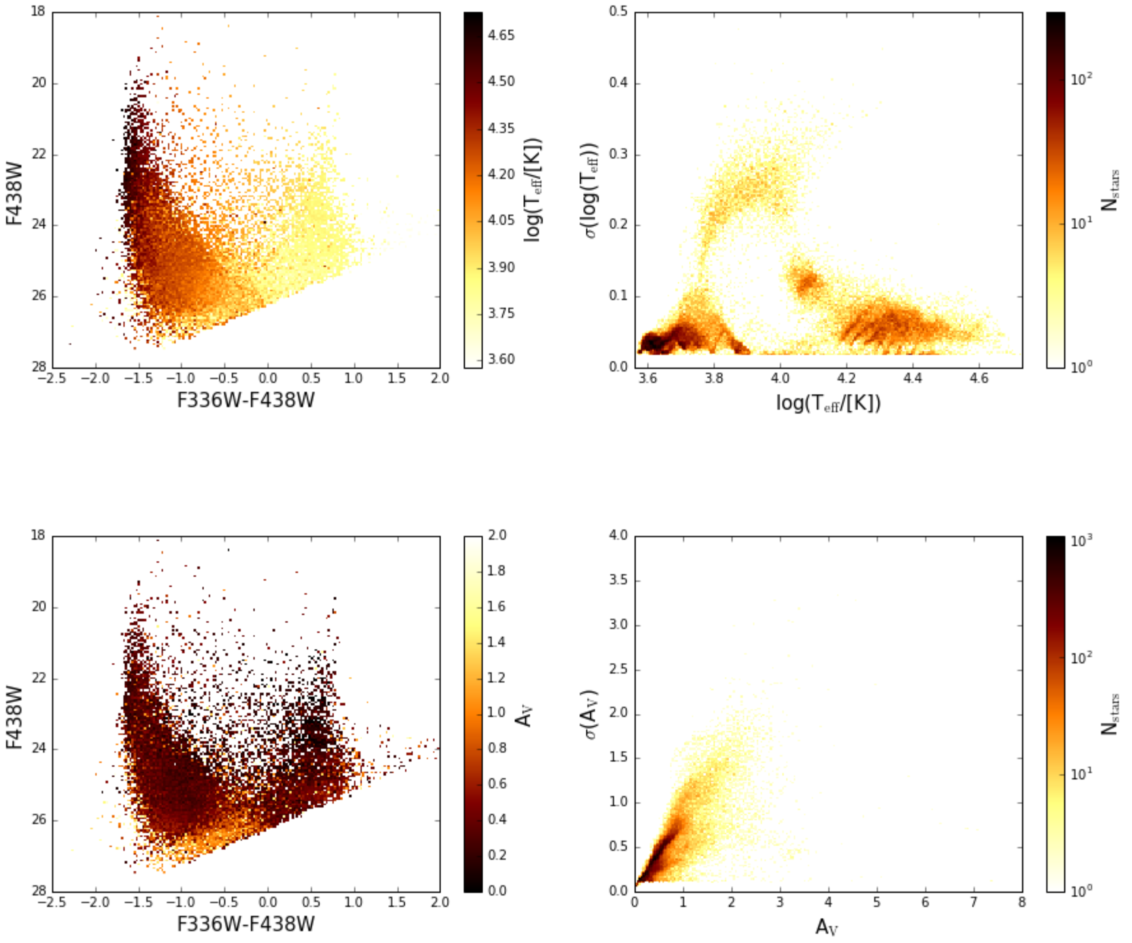

Figure 2.12 The CMD color-coded by the expected values for $\log(T_{\rm eff}/[{\rm K}])$ (left). The 1σ uncertainty on $\log(T_{\rm eff}/[{\rm K}])$ (right). *Bottom:* The CMD color-coded by the expected values for $A(V)$ (left). The 1σ uncertainty on $A(V)$ (right).

in deriving the LyC flux. In our sample, the 4-band detection requirement likely excludes some of highly extincted young stars. However, the BEAST predicted FUV flux agrees very well with the real GALEX FUV measurement, suggesting the sample is complete for this study (see Section 2.5.1).

Figure 2.13 compares the spatial distribution of $A(V)$ to 24 μm emission (*Spitzer* MIPS; Dale et al. 2009) from dust heated by stellar populations. On the derived $A(V)$ map, one can see imprints of two distinct footprints; a smaller footprint for WFC3/IR and a larger footprint for WFC3/UVIS. Most stars in our catalog are RGB stars, which are confined to the smaller WFC3/IR footprint. These stars are detected in 4 or more bands with any combination of UV, optical and IR. However, there are some stars that are only associated with the larger WFC3/UVIS footprint. These stars have to be detected in all F225W, F336W, F438W, and F814W to fulfill the $\geq$ 4-band detections criterion, leading to a bias towards UV-bright stars. Thus these stars are well fitted by massive hot star models. Indeed, this bias is obvious in the stellar mass maps (see Figure 2.15) as well. We measure the escape fraction both with and without these stars in Section 2.7, and find that their contribution to the ionizing radiation is negligible.

In Figure 2.13, there is a strong spatial correlation between the derived $A(V)$ map and the observed 24 μm emission. Although the 24 μm observation lacks the angular resolution for the detailed comparison, it is clear that higher $A(V)$ values are found in the same regions where the 24 μm emission is stronger, validating our SED fitting technique. While the overall extinction in NGC 4214 is not severe, the extinction is significant in the central SF complexes and some of the small SF knots. High extinction pixels outside these SF regions result from cool stars with high dust column density. These stars likely lie behind the layer of dust. To further explore the correlation between the ISM structure and stellar populations, we construct dust maps for two different stellar populations: one from hot stars with $\log(\mathrm{T_{eff}}) \geq 4.4$, and the other from stars cooler than $\log(\mathrm{T_{eff}}) = 4$. The former samples dust associated with hot young stars, and the latter samples the spatially distributed population of RGB stars.

The dust maps in Figure 2.14 are useful diagnostics of the structure of the ISM, giving insights into how ionizing radiation may escape. The top panel presents the dust column density in front of hot stars ($\log(\mathrm{T_{eff}}) \geq 4.4$). Hot stars are mostly concentrated in the galactic center, and sparsely distributed outside that region. In the NW SF complex, the dust distribution indicates the prominent shell structure in the gas, where we see low extinction in front of the cluster of hot stars and high extinction at the boundaries of the SF complex. Maiz-Apellaniz et al. (1998) also found that the dust in the NW complex is decoupled from the central star clusters, and is located at the boundary. These shells at the boundary are produced when strong stellar feedbacks, such as stellar winds, jets and supernovae, expel the residual ISM from the nascent molecular clouds. The $A(V)$ map, therefore, supports spatial decoupling between evolved (i.e., the first supernova went off) massive stars and the surrounding ISM (Maiz-Apellaniz et al. 1998; MacKenty et al. 2000). This process also naturally leads to “holes” through which ionizing photons can escape. Thus, we can expect high escape fraction from the NW SF complex.

The bottom panels of Figure 2.14 shows the dust column density in front of cooler stars ($\log(\mathrm{T_{eff}}) < 4$). Outside the SF regions, the dust column density is low, and the dust is smoothly distributed across the entire galaxy. However, the dust distribution toward the SF regions, where most massive stars are located, has high extinction and a more complex morphology. Since these cooler (and mostly older) stars uniformly sample line-of-sights across the galaxy, the clumpy morphology of the dust in front of them is an indication of the intrinsically clumpy ISM structure in NGC 4214.

In the top panel of Figure 2.15, we display the stellar initial mass map. Most massive ($> 10\ M_\odot$) stars are confined to the three main SF complexes in the galactic center where Hα is also emitted (see Figure 2.4). This centralized location is well consistent with the enhanced recent SF in the galactic central regions (Williams et al. 2011).

This trend is also consistent with the results from the stellar cluster analysis of Úbeda et al. (2007) and composite spectrum analysis from Hermelo et al. (2013). Sollima et al. (2014) recovered the SFH for the Central complex and reported a strong peak of SFR at age of ∼8 Myr. Although the averaged age of the SE complex seems to be slightly younger (1–2 Myr) than that of the Central complex (e.g., Leitherer et al. 1996; MacKenty et al. 2000; Úbeda et al. 2007), the Central complex harbors more O/B stars than the NW and SE complexes by a factor of ∼2 and 1.25, respectively. In addition, compact Hα morphology of the SE complex suggests no spatial decoupling between the ISM and embedded stars, which would prevent ionizing photons from escaping the complex. Thus, we expect more ionizing photons emerging from the Central complex than the SE complex.

The central concentration of massive stars should be imprinted in the stellar temperature map. We select the hottest stars ($\log(\mathrm{T_{eff}}) \geq 4.4$) in the galaxy and examine their spatial distribution (bottom panel of Figure 2.15). As expected, the hottest stars are also clustered mostly in the central SF regions, i.e., co. These highly-localized hot and massive (and thus young) stars will be the ionizing sources in NGC 4214. That means the ionizing photon production in NGC 4214 is highly localized. Furthermore, these stars are spatially

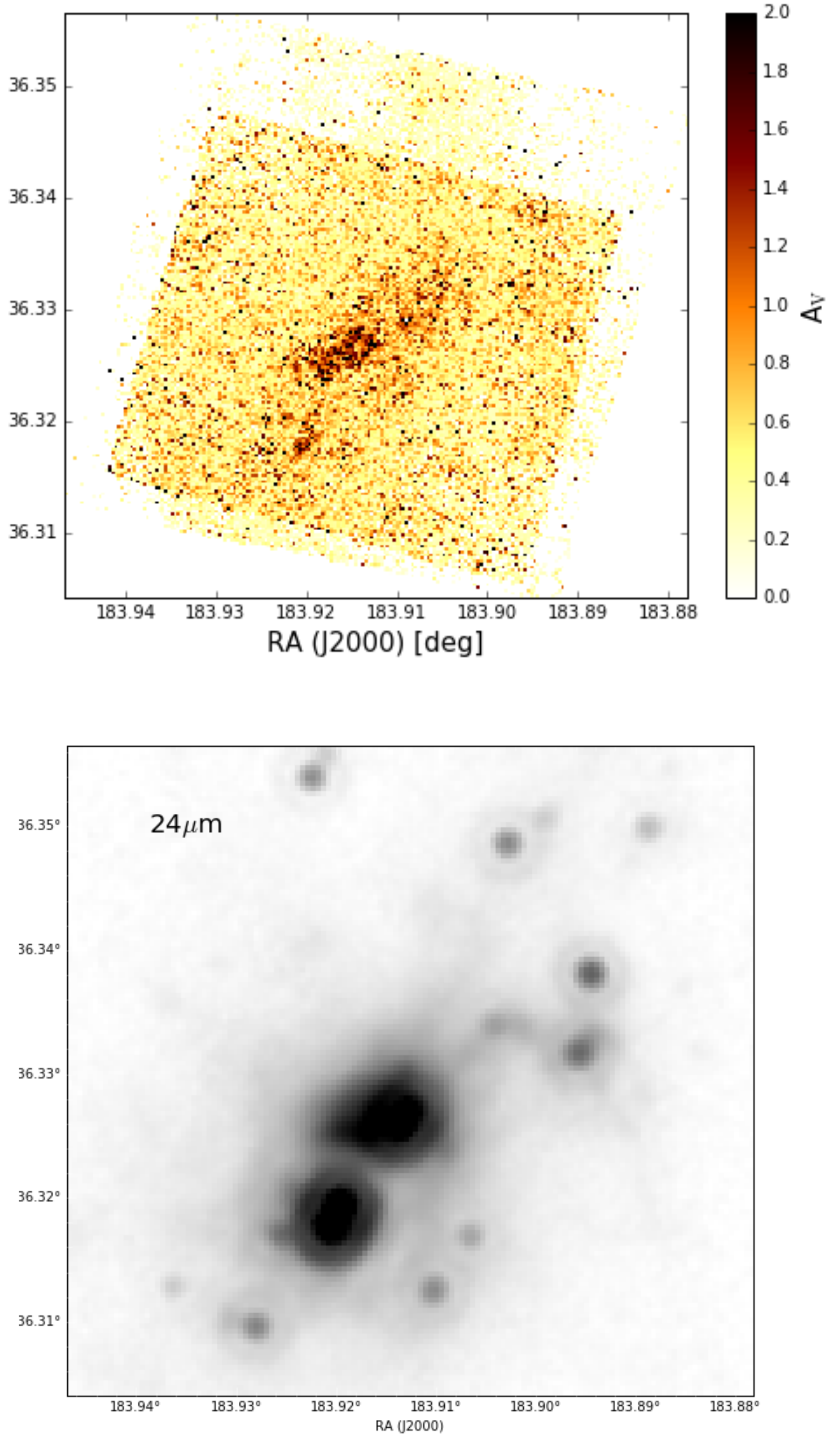

Figure 2.13 Maps of $A(V)$ (top) and MIPS 24μm emission (bottom). These maps show good spatial correlation, indicating the presence of dusty SF regions in the galactic center.

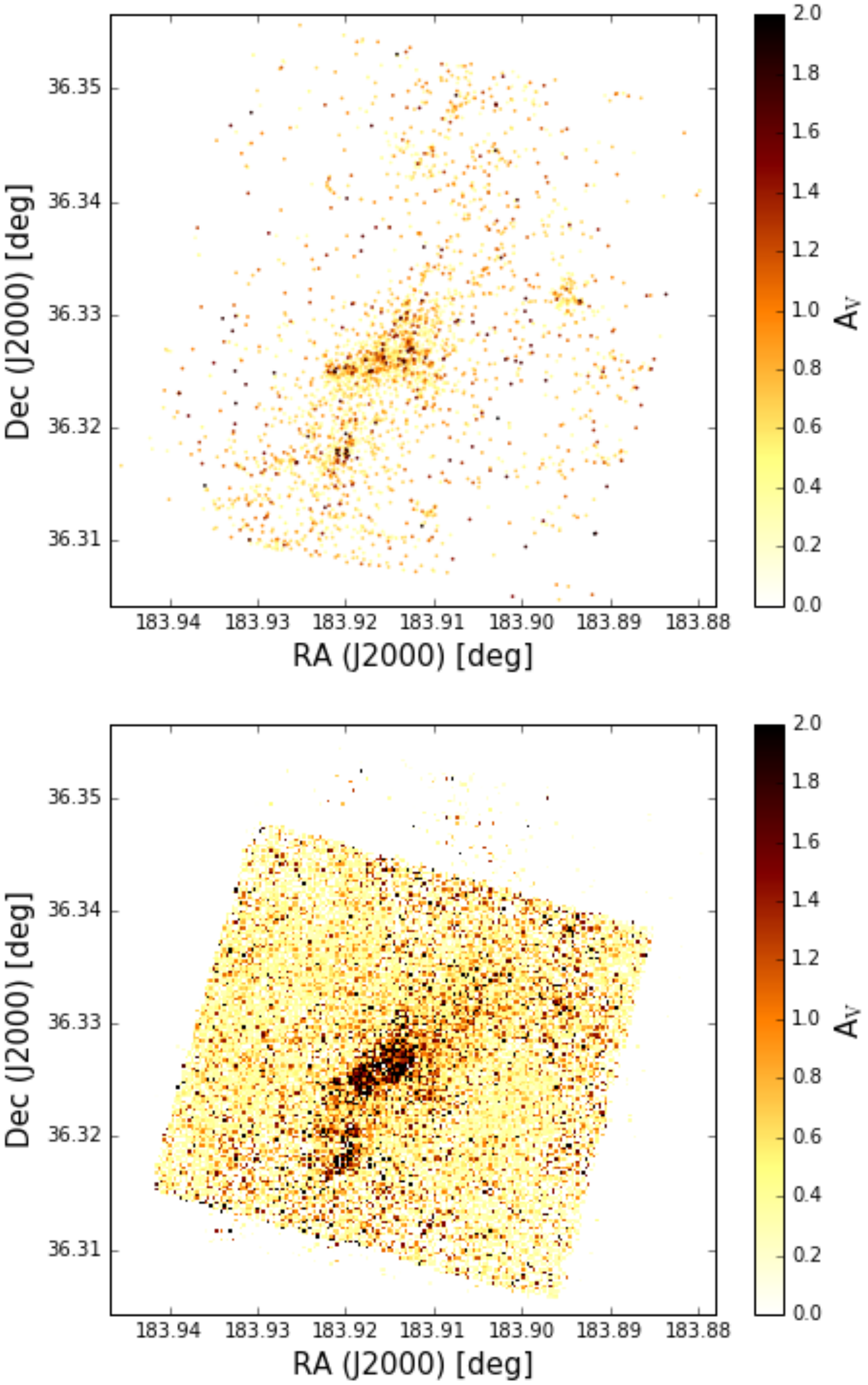

Figure 2.14 Maps of $A(V)$ for stars with different stellar temperatures. The top panel shows the dust distribution of in front of stars with $\log(T_{\mathrm{eff}}) \geq 4.4$, corresponding to early B-type star. The bottom panels shows the dust distribution of in front of stars cooler than $\log(T_{\mathrm{eff}}) = 4$.

coherent with the hydrogen gas tracer, Hα emission (Figure 2.4), and the dust tracer, 24 μm emission (Figure 2.13). This coherence suggests that both the photoionization and dust absorption are significantly localized, implying local variation in the escape fraction as well. We therefore choose to divide NGC 4214 into distinct SF regions, based on the Hα emission morphology, and we measure the escape fractions for individual SF regions in addition to the global escape fraction for the galaxy. We discuss this in detail in Section 2.6.1.

2.5.1 Verifying the UV Flux Production

We now infer both dust-free and reddened fluxes at UV wavelengths from the stellar parameter fits. We first identify the individual stars producing FUV and LyC photons. In Figure 2.16, we present the CMDs color-coded by unreddened FUV magnitude (top panel) and the intrinsic ionizing photon production rate $\dot{N}_{\rm int}$ (bottom panel), where $\dot{N}_{\rm int}$ is computed over wavelengths from 90 Å to 912 Å [2]. For each star, we convolve the stellar model with the GALEX FUV bandpass and a LyC tophat filter to calculate the FUV and LyC fluxes. We repeat this process for the unreddened model as well. As expected, bright main sequence (MS) stars have the largest FUV and LyC fluxes. Among the MS stars ($\log(g) \geq 4.0$), there is a factor of 10^4 and 10^{11} variation in FUV flux and $\dot{N}_{\rm int}$ (respectively) from the hottest to the coolest detected stars. RGB stars produce $\sim 10^4$ times fewer ionizing photons than even the coolest MS stars.

It is clear that massive MS stars are likely to be responsible for most of the UV and LyC flux in NGC 4214. However, we still need to verify whether the stars in Figure 2.16 capture essentially all of UV flux. To test this, in Figure 2.17 we plot the cumulative distribution of UV flux and $\dot{N}_{\rm int}$ produced by individual stars, as a function of $\log(\mathrm{T_{eff}})$. We find that stars that are responsible for 99% of the GALEX FUV flux have $\log(\mathrm{T_{eff}}) \gtrsim 4.08$, corresponding to A-type MS stars, while stars producing 99% of the LyC photons have higher temperatures, $\log(\mathrm{T_{eff}}) \gtrsim 4.41$, corresponding to B0-0.5 MS stars. The number of detected stars contributing to LyC photons is small; ~5% of detected stars in NGC 4214

---

[2] The number of ionizing photons within wavelengths < 228 Å (corresponding to He II ionization energy of ~54.42 eV) is less than ~3% of the total $\dot{N}_{\rm int}$ due to the small number of stars with $\log(\mathrm{T_{eff}}) \gtrsim 4.7$ that emit significant energy beyond 4 Rydberg.

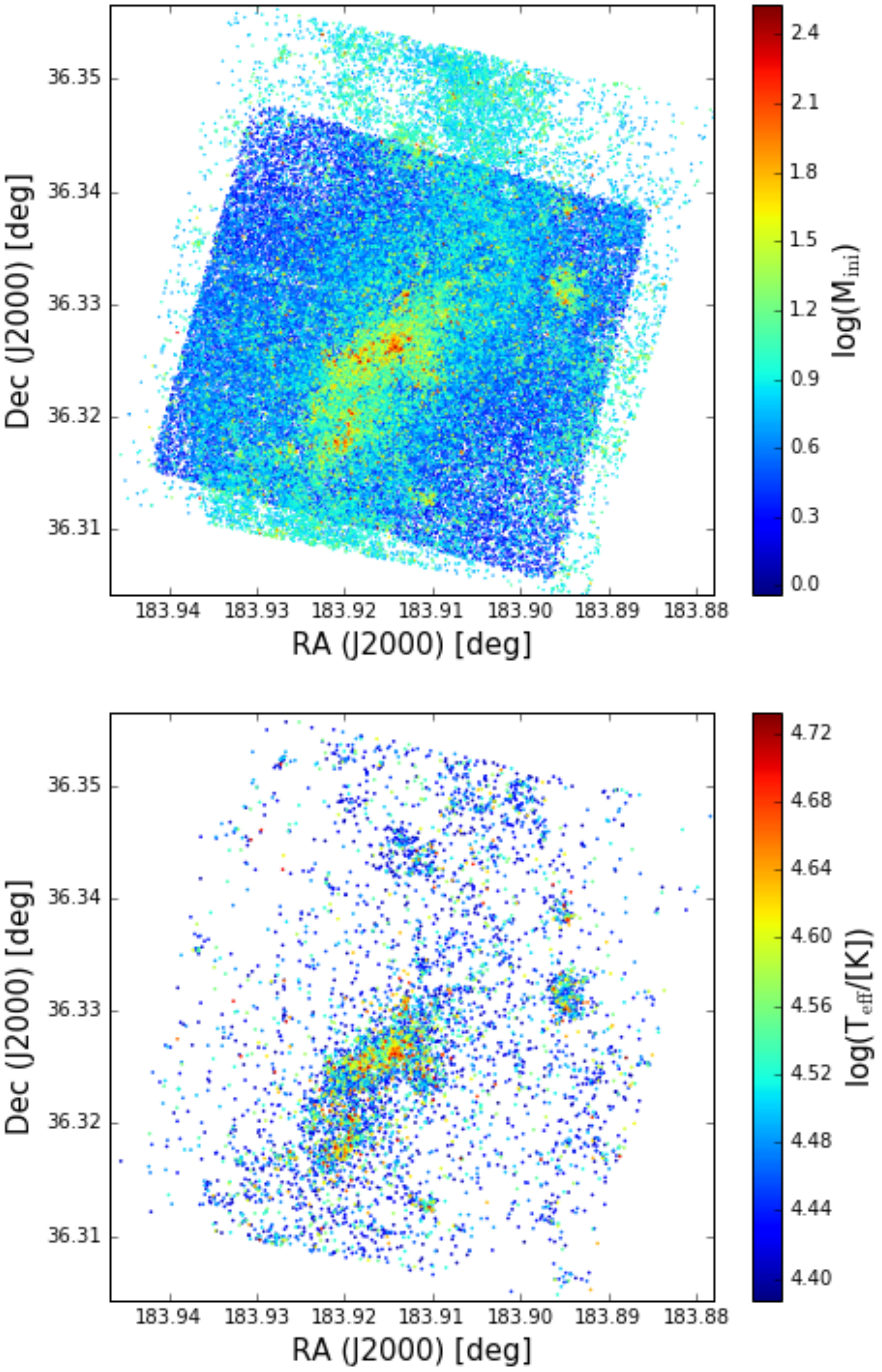

Figure 2.15 Maps of stellar initial mass and temperature. The top panel shows the stellar initial mass distribution. The bottom panels shows the stellar temperature distribution of in front of stars cooler than $\log(T_{\text{eff}}) = 4$.

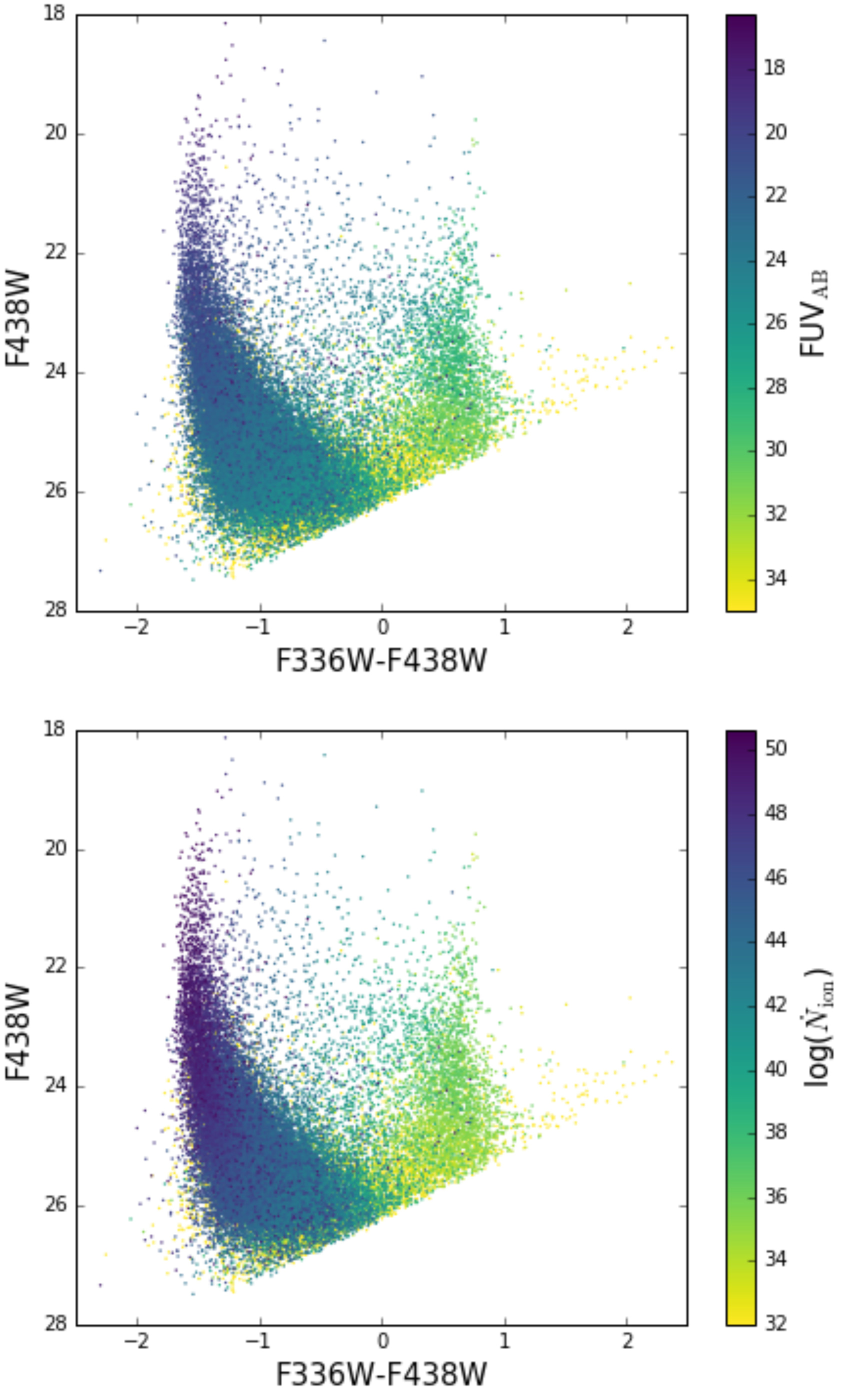

Figure 2.16 CMDs color-coded by FUV magnitude (left panel) and by the intrinsic ionizing photon production rate $\dot{N}_{\mathrm{int}}$ (right panel). This figure indicates how much FUV and LyC fluxes are produced by individual stars. As expected, bright main sequence stars produce the largest FUV and LyC fluxes.

produce all LyC photons.

For reference, we present the F438W magnitude versus $\log(T_{\rm eff})$ for MS stars ($\log(g) > 4$) in the bottom right panel of Figure 2.17. It shows the depth of the dataset needed to secure sufficient flux coverage for the ionizing sources. At around F438W = 26.26 mag, the number of observed stars starts to decrease, and nearly all stars hotter than $\log(T_{\rm eff}) = 4.41$ are brighter than this magnitude. In addition, the F438W 50% completeness magnitudes in all stellar number density bins are fainter than 26.26 mag. Thus, our sample seems to be complete for obtaining the LyC flux. For the GALEX FUV flux, it seems stars fainter than F438W = 26.26 mag contribute to fair amount of the observed FUV flux. Therefore, our sampling of GALEX FUV emitters might not be complete.

We test our degree of incompleteness, and verify our UV flux recovery in Figure 2.18, where we compare the reddened FUV flux prediction with the actual GALEX FUV observations (contours). Using the FUV fluxes of the individual stars, we generate maps of the expected GALEX FUV image. For direct comparison with the GALEX observation, we degrade the predicted high resolution FUV map with the GALEX FUV image's FWHM of 4.2". First of all, the FUV observation and the BEAST prediction agree very well morphologically. The predicted FUV map recovers both the global shape and the small structures for individual SF complexes seen in the GALEX image. The excellent morphological agreement between the actual observation and our prediction suggests reliable predictions in the FUV, and strongly suggests that our reconstruction is likely to hold at shorter wavelengths below the Lyman limit where our sample seems to be complete. From the predicted FUV map, we compute the total magnitude by considering only the pixels above the GALEX FUV flux limit[3]. The total FUV magnitude is ∼15.45 mag after the MW extinction correction, which is ∼40 times fainter than the observed value (11.47±0.05 mag; Lee et al. 2011). This shows that our sample is not complete for the FUV flux as expected. If we sum the reddened FUV fluxes from the individual stars (i.e., no degrading), the total magnitude is ∼11.15 mag after correcting for the MW extinction.

In Figure 2.19, we also present the $\dot{N}_{\rm int}$ map with the same spatial resolution with the

---

[3] For the exposure time of 2003 seconds, the FUV flux limit is 23 $\rm mag_{AB}$, corresponding to 2.98×10^{-17} erg cm^{-2} s^{-1} Å^{-1}.

GALEX FUV map for easy comparison. Morphologically, the $\dot{N}_{\rm int}$ map correlates with the FUV map, confirming that FUV bright stars also produce most of ionizing photons. Production of ionizing photons in the galaxy is highly localized, as expected from the maps of stellar mass and temperature (Figure 2.15).

2.6 UV Absorption by Gas and Dust

We have calculated the LyC photons produced by individual stars, and mapped the intrinsic LyC photon production rate. We now consider the two major mechanisms by which ionizing radiation can be absorbed – gas and dust. We account the neutral gas absorption by the recombination Hα emission line, and the dust absorption by using the SED fitting, as we describe in detail below.

2.6.1 Gas Absorption Traced by Hα

We trace the absorption of LyC photons by gas through the subsequent emission of hydrogen recombination lines by the ionized gas. The number of ionizing photons consumed by photoionization ($\dot{N}_{\rm gas}$) can be measured through the Hα luminosity. The conversion factor between Hα luminosity and ionizing photon production rate is well established for standard radiative transfer assumptions (Kennicutt & Evans 2012). The extinction-corrected Hα luminosity can be converted into the number of ionizing photons consumed by the surrounding hydrogen gas (Hummer & Storey 1987; Kennicutt 1998). Under the assumption of Case B recombination for $T_{\rm e} = 10^4$ K and $n_{\rm e} = 10^2$ cm^{-3},

$$\dot{N}_{\rm gas} = 7.31 \times 10^{11} L({\rm H}\alpha). \tag{2.11}$$

We derive an extinction-corrected Hα map using HST narrow-band images of Hα (F657N) and Hβ (F487N) lines from GO-11360 (PI: O'Connell). We first subtracted scaled continuum images in the appropriate filters (F814W and F438W, respectively) from drizzled Hα and Hβ emission images. A scaling factor for each continuum image was determined by minimizing absolute residuals in regions where stellar continuum is dominant (i.e., where nebular emission is negligible). We also accounted the [NII] contribution using the [NII]/Hα ratio of

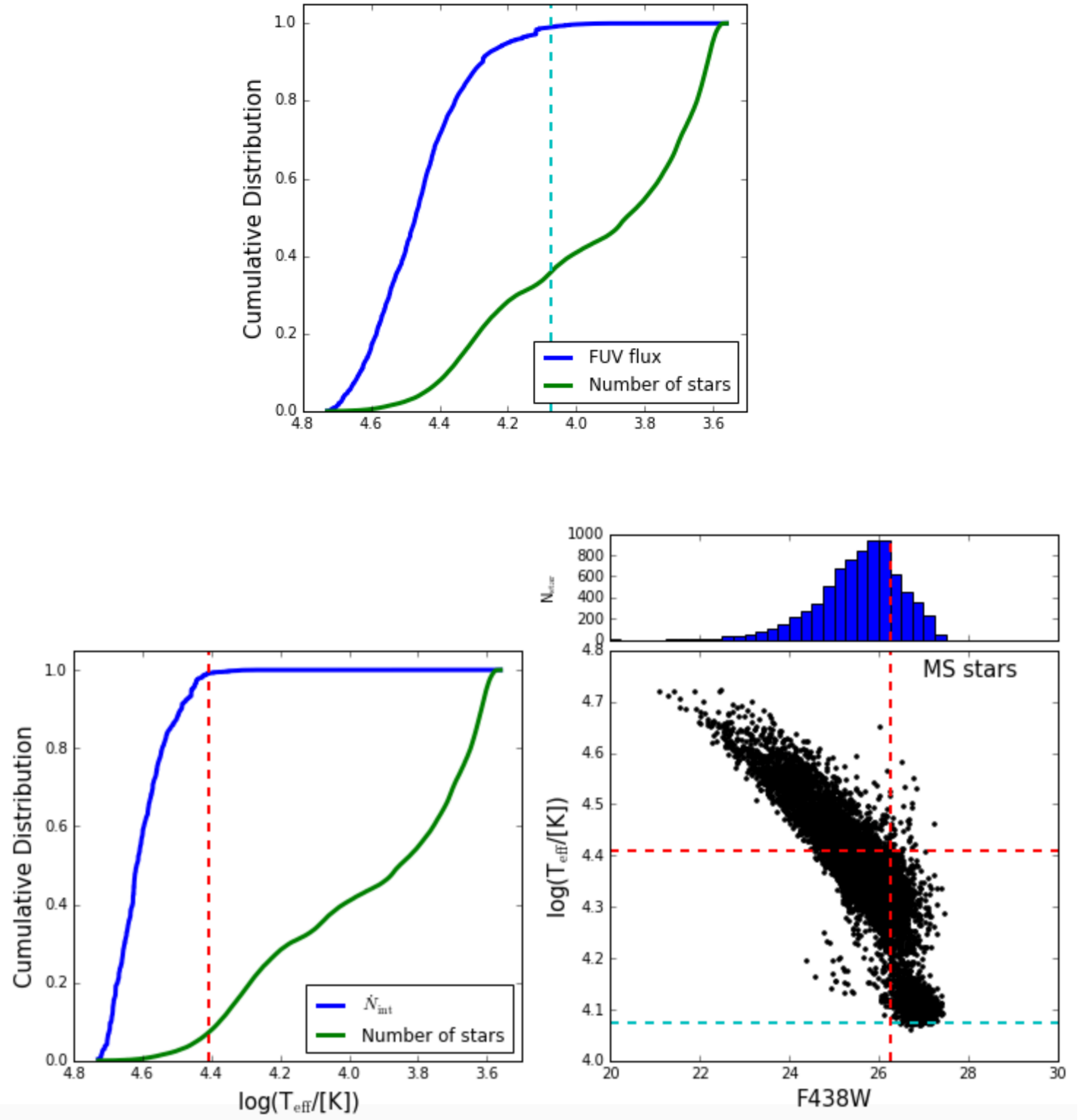

Figure 2.17 Cumulative distributions of FUV flux (top panel) and $\dot{N}_{\rm int}$ (bottom left) as a function of log(T$_{\rm eff}$). The bottom right panel shows the F438W magnitude versus log(T$_{\rm eff}$) for MS stars. These plots suggest the depth of our data is perfectly adequate for the LyC study, and so nearly for the FUV study. We draw a cyan (red) dashed line at reaching to 99% of FUV flux ($\dot{N}_{\rm int}$).

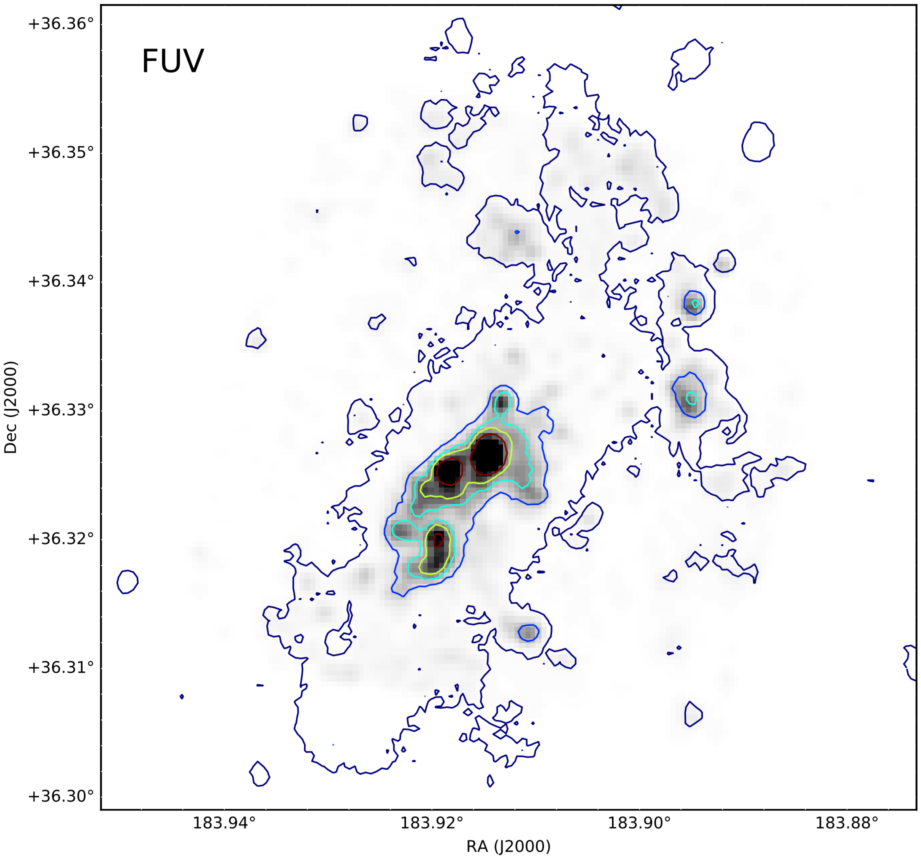

Figure 2.18 Comparison of the reconstructed FUV map, derived from the BEAST, with actual GALEX FUV observations (contours). They show an excellent agreement.

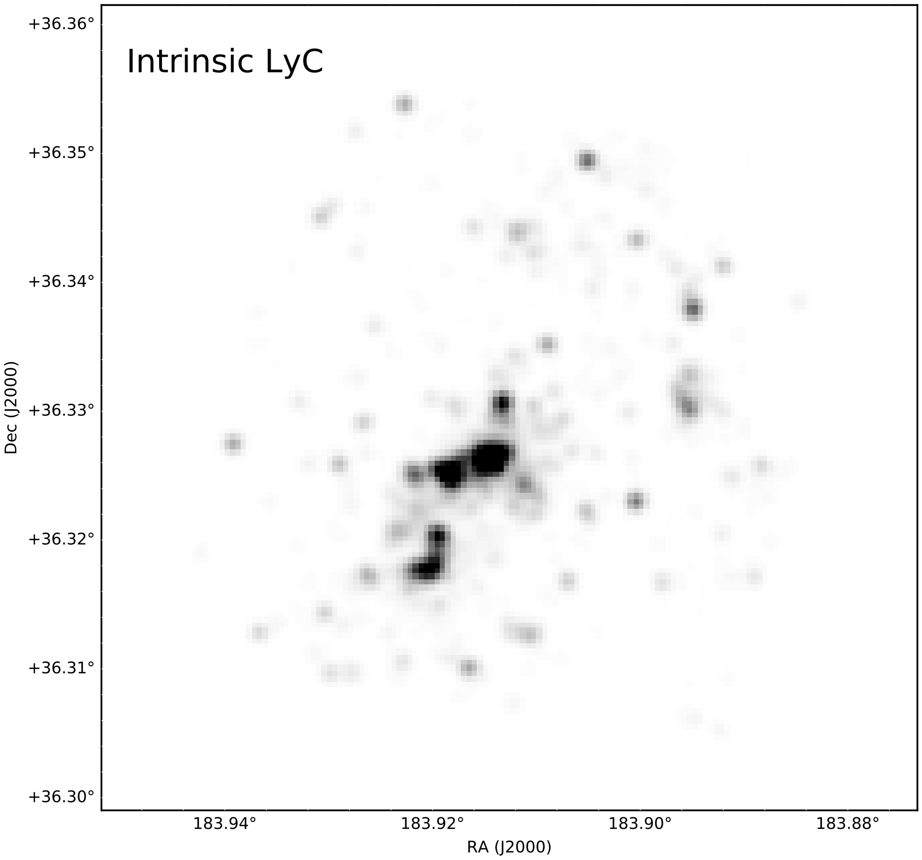

Figure 2.19 The predicted map of the intrinsic ionizing photon production rate ($\dot{N}_{\rm int}$).

0.117 (Kobulnicky & Skillman 1996). We then combine these continuum-subtracted emission images to calculate an extinction map using the Balmer decrement Hα/Hβ, and correct the Hα emission-line map for extinction. Figure 2.21 presents the extinction-corrected Hα image. We convert this to a number of ionizing photons absorbed by the surrounding neutral gas ($\dot{N}_{\text{gas}}$) using Equation 2.11. The converted total number of ionizing photons is $\dot{N}_{\text{gas}} \simeq 1.3 \times 10^{52}$ per second with ~11% uncertainty, which results from the propagation of the uncertainty in continuum subtraction.

As we briefly discussed earlier, all the determinants of the escape fraction are highly localized. To properly account the escape fraction, we thus need to correctly designate stars that actually ionize the surrounding hydrogen gas and heat the surrounding dust. If we knew the 3D distribution of the ISM and ionizing sources, it might be possible to track propagation of ionizing photons by solving complex radiative transfer equations, and thus we might be able to make the escape fraction map with full HST resolution. However, this approach is not possible with observational data without extremely simplified assumptions.

Therefore, we choose to measure the escape fraction for individual SF regions. These single SF regions should capture both the local production of ionizing photons and their interaction with the surrounding gas and dust within that SF region. We identify individual SF regions based on Hα emission morphology, on the theory that the boundary of each ionized HII region is a good tracer of the SF region's extent. In Figure 2.21, we mark 13 identified SF regions on top of the extinction-corrected Hα image.

2.6.2 Dust Absorption Traced by SED Fitting

We infer the absorption by dust along the line-of-sight from the same SED fitting used to infer the intrinsic LyC flux. The difference between the intrinsic and dust reddened SED in the observed HST filters is attributed to photons being absorbed by the dust. To extrapolate this absorption to the LyC regime, we must assume a form for the extinction curve that extends to below the Lyman limit. As we described earlier (Section 2.4.2), we use a mixture model based solely on observations (Fitzpatrick (1999) for the MW extinction curves and Gordon et al. (2003) for the SMC Bar extinction curves) above $\lambda > 1695$ Å.

On the other hand, we use theoretical extinction curves from Weingartner & Draine (2001) below the Lyman limit. Between 912 Å, $< \lambda <$ 1695 Å, where the observational uncertainty is significant (Fitzpatrick 1999), we smoothly transition from the theoretical to the observed extinction curves by computing a weighted mean between the observational and theoretical curves, where the weight linearly varies from 90 at 912 Å, to 1 at 1695 Å, for the BEAST's default curves and from 1 to 0 for the theoretical extinction curves (see Figure 2.8).

In the BEAST, we apply this modified extinction curve to unreddened model SEDs for individual stars using their inferred dust properties. To calculate the number of residual ionizing photons from being absorbed by dust along the line-of-sight, we integrate the attenuated SEDs between 90 Å $< \lambda <$ 912 Å. By subtracting these residual ionizing photons from the intrinsically produced ionizing photons, we measure how many ionizing photons were absorbed by the intervening dust while traveling towards us ($\dot{N}_{\rm dust}$). In Figure 2.20, we show the map for residual ionizing photons after dust absorption.

2.7 The Escape Fraction Measurement

To measure the escape fraction, we need the amount of ionizing photons produced and consumed within a galaxy both by neutral gas and the dust (see Figure 2.1). We have presented the measurement of the intrinsic ionizing photon production rate for individual stars from the SED fitting in Section 2.5.1. We have calculated absorption of these photons by gas and dust in Section 2.6.

Once we have all these measurements, we compute the ionizing photon escape fraction as follows in each SF region:

$$f_{\rm esc} = \frac{\dot{N}_{\rm int} - \dot{N}_{\rm gas} - \dot{N}_{\rm dust}}{\dot{N}_{\rm int}}. \tag{2.12}$$

As we briefly mentioned in Section 2.5, we calculate $f_{\rm esc}$ as a function of position due to highly localized distributions of ionizing stars, gas, and dust. In the equation, the two terms, $\dot{N}_{\rm int}$ and $\dot{N}_{\rm gas}$, have no dependence on the geometry. This is because the first term is derived from the intrinsic stellar property, and the second term is measured from the isotropic Hα recombination line. Therefore, we can assume these two values reflect the 4π sr property, and our assumption of spherically symmetric emission is reasonable. On the other hand,

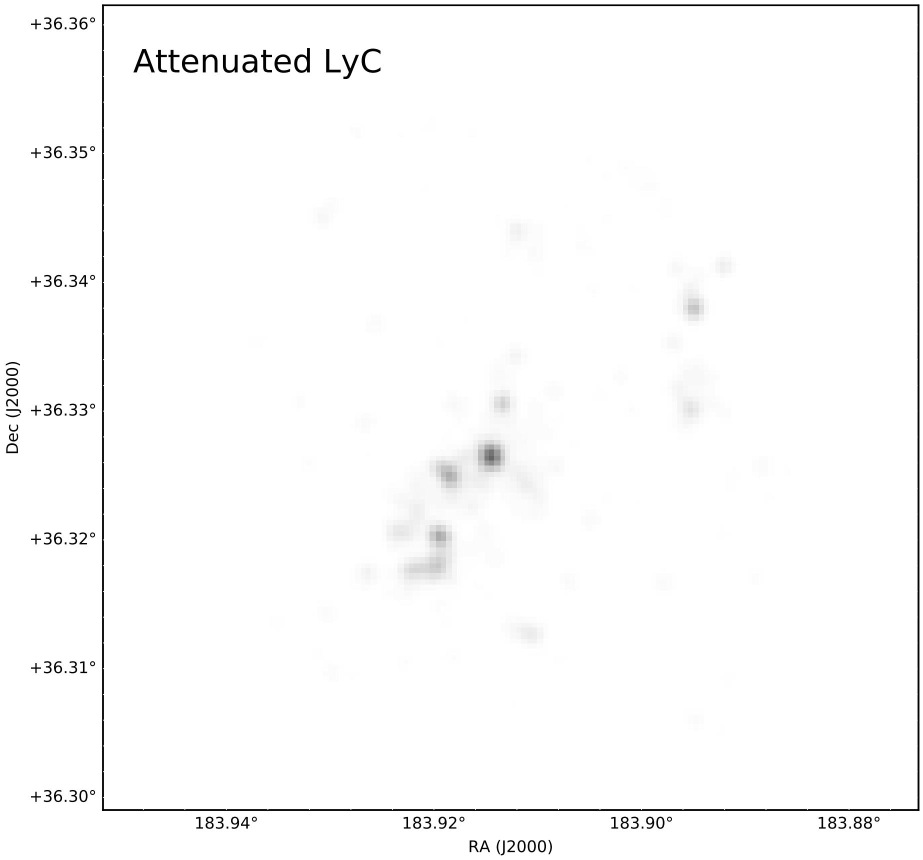

Figure 2.20 The predicted map of the residual ionizing photons after dust absorption, i.e., $\dot{N}_{\rm int}$ - $\dot{N}_{\rm dust}$. This map is in the same color scale with the $\dot{N}_{\rm int}$ map. Clearly, not many ionizing photons can make it to us.

$\dot{N}_{\rm dust}$ is measured based on the dust column density in front of individual stars, meaning we only know the line-of-sight dust distribution.

The measurement of escape fraction may depend on the orientation of observations, because the direction of opening holes is determined by the initial ISM geometry. Along originally optically-thin regions, stellar feedback would create low-density holes or channels more easily compared to originally optically-thick regions. Thus, if the observer is well-aligned with the low-density channels in a galaxy, the observer would measure a high escape fraction for that galaxy, and vice versa. Difficulty is that we only measure the dust column density along the line-of-sight, but it could have different dust extinction in other directions.

To overcome this limitation, we can adopt a covering factor ($f_{\rm cov}$) for a SF region. The covering factor represents how much fraction of the HII region's surface is covered by the surrounding ISM. For example, the $f_{\rm cov}$ of 0.5 means that half of the HII region is homogeneously covered by the ISM, while another half is uncovered allowing the ionizing photons to escape without obscuration. Thus, the covering factor can be expressed as the ratio of dust emission to intrinsic star light. Adopting the covering factor is reasonable, because HII regions are typically matter-bounded. When applying $f_{\rm cov}$, the term $\dot{N}_{\rm dust}$ in Equation 2.12 has to be replaced with $f_{\rm cov} \times \dot{N}_{\rm dust}$.

Hermelo et al. (2013) estimated the covering factors for SF complexes in NGC 4214 by modeling their dust SEDs leaving $f_{\rm cov}$ as a free-parameter in their fitting. Their best-fit models for a metallicity of 0.2 $Z_\odot$ suggest $f_{\rm cov}$ of 0.3 for the Central and NW SF complexes, and 0.6 for the SE SF complex, respectively. Since their measurements were based on low angular resolution IR observations (Spitzer, Herschel, Planck, and IRAM), $f_{\rm cov}$ is not available for individual SF regions. Thus we apply $f_{\rm cov}$ of 0.3 for the Central, NW SF complexes, and the one SF region (region 9) nearby the Central complex as well. For five SF regions in the SE complex (regions 3a–3e), we adopt $f_{\rm cov}$ of 0.6. For the rest of SF regions, we apply both 0.3 and 0.6 to get the lower and upper limits on the escape fraction. We list these measured escape fractions for each SF region in Table 2.7.1. The intrinsic ionizing photon production rates for individual SF regions are also listed in the same Table.

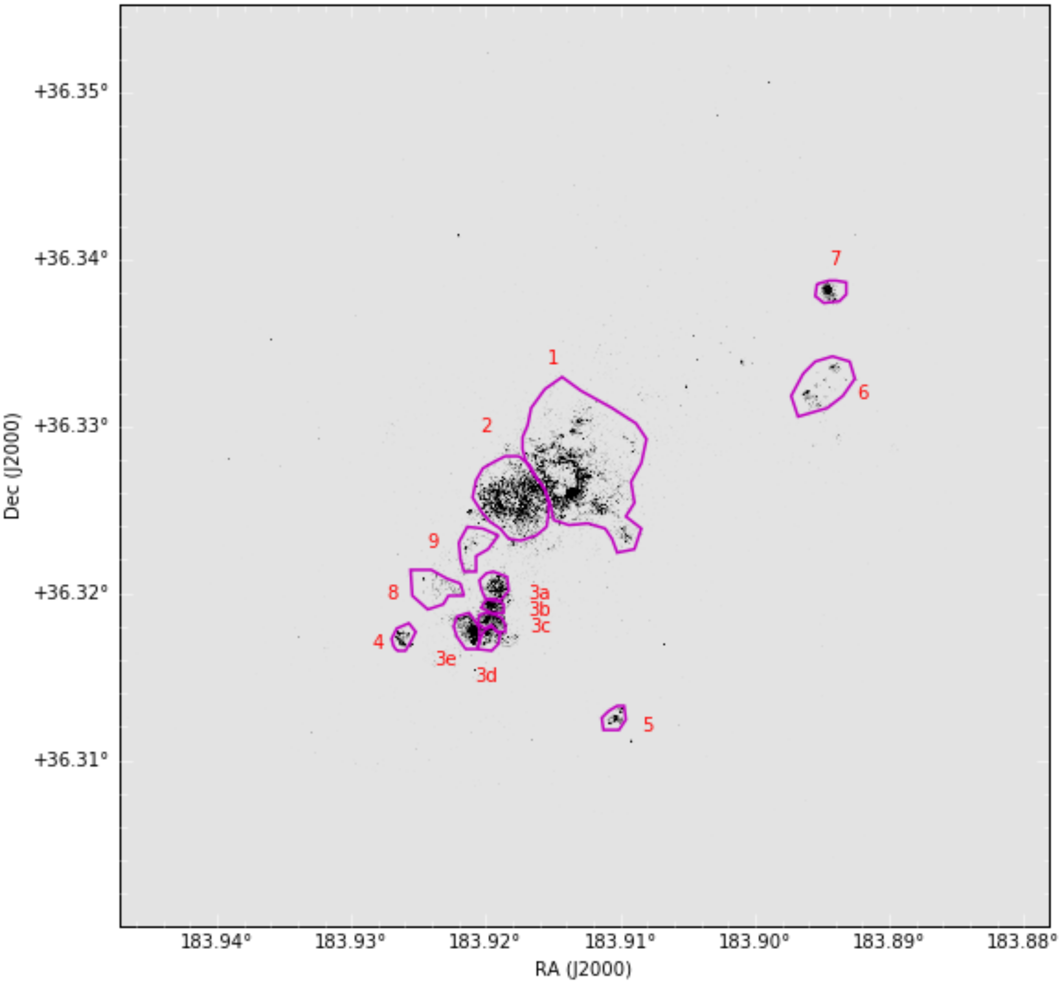

Figure 2.21 The extinction-corrected Hα Map. To derive this map, we first subtracted scaled continuum images in the appropriate filters (F814W and F438W, respectively) from drizzled Hα and Hβ emission images. We also accounted the [NII] contribution using the [NII]/Hα ratio of 0.117 (Kobulnicky & Skillman 1996). We then combine these continuum-subtracted emission images to calculate an extinction map using the Balmer decrement Hα/Hβ, and correct the Hα emission-line map for extinction. We also mark individual SF regions for which we measure the escape fractions.

2.7.1 Local Escape Fraction Map for NGC 4214

We present the map of the line-of-sight escape fraction of ionizing photons for NGC 4214 in Figure 2.22. We denote results for individual SF regions by overplotting their boundaries with lines colored to represent their escape fractions. The local escape fractions vary spatially, with some regions having essentially no escape ($f_{\rm esc} \sim 0$), and others having $f_{\rm esc}$ as large as 20%. The escape fraction is high in the superbubbles, i.e., the NW (11.37%) and Central (15%) SF complexes (regions 1 and 2). Morphologically, these regions have clear shells that indicate a large opening angle towards us, consistent with their high escape fractions. The SF region 9, located near the superbubbles, also shows relatively high escape fraction of 6.86%. The highest escape fraction (20%) is found in the SF region 3a, which harbors the youngest stars (∼2–4 Myr; Úbeda et al. 2007; Hermelo et al. 2013). In addition, this region has a narrow crack in front of the central stars, seen in Hα emission (Figure 2.2), which is likely a very young low density hole. Because of its young age, this high escape fraction may occur as the SF region start expelling the surrounding ISM.

The SF regions marked by blue-colored lines have zero escape fractions, These are in the SE SF complex (3b–3e), and in SF regions 4, 5, 6, 7, and 8. These regions show either high dust content or a small number of ionizing sources. The lack of detected massive stars might be due to highly embedded SF (e.g., the SE SF complex). These regions seem to be fully covered by the gas and dust in directions towards us. Considering the age (∼2–4 Myr), these SF regions, especially the SE complex (3b–3e), have not evolved enough to undergo the significant stellar feedback to spatially decouple the stars from the ISM. Or, it is possible that low-density holes are facing the opposite direction. The inclination of the galaxy, i =44 degrees (Walter et al. 2008), might misplace the preferred directions, usually along the minor axis, of low-density holes in our line-of-sight.

2.7.2 Global Escape Fraction of NGC 4214

To obtain a proper global escape fraction (i.e., integrated over 4π sr, not just along the line-of-sight), it is necessary to consider the covering factors of each SF region. Thus, we integrate all the intrinsic ionizing photons ($\dot{N}_{\rm int}$), ionizing photons consumed by photoion-

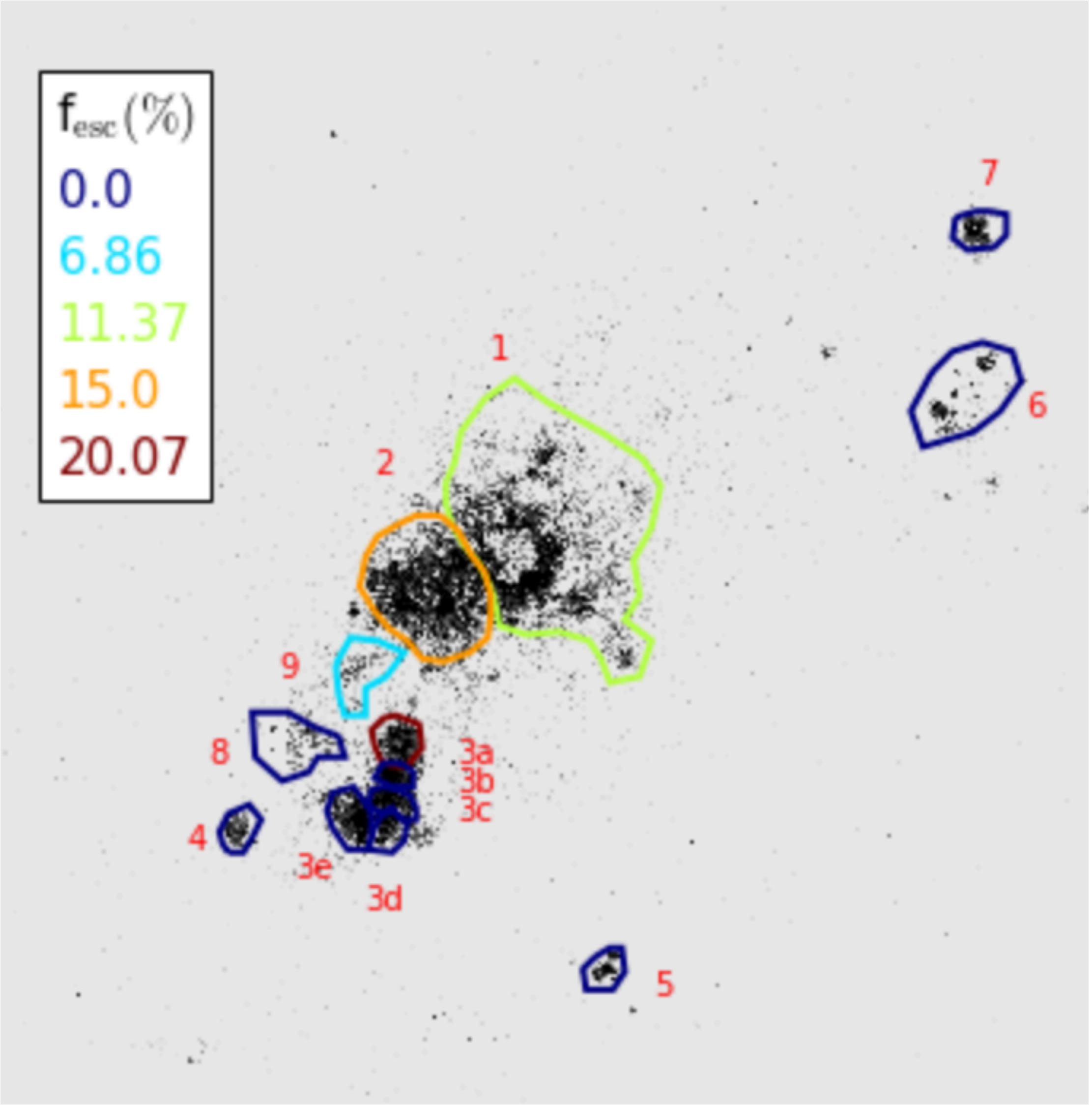

Figure 2.22 Map of the escape fraction of ionizing photons. We only show a zoomed-in portion of the Hα image. Solid lines denote the individual SF regions, and are color-coded by their measured escape fractions. The local escape fraction varies from 0% to ~20%.

Table 2.1. Local Escape Fraction for Each SF Region.

SF Region[a]	f_{cov}[b]	f_{esc}[c](%)	$\dot{N}_{\text{int}}$ (s^{-1})
1 (shell)	0.3	$11.38^{+5.83}_{-7.13}$	5.16×10^{51}
2 (shell)	0.3	$15.00^{+12.18}_{-14.96}$	3.63×10^{51}
3a (small hole)	0.6	$20.08^{+4.67}_{-3.84}$	1.32×10^{50}
3b (compact)	0.6	$0.00^{+0.00}_{-3.71}$	5.28×10^{45}
3c (compact)	0.6	< 0.74	4.37×10^{48}
3d (compact)	0.6	< 1.42	4.73×10^{47}
3e (compact)	0.6	< 3.98	2.69×10^{50}
4 (compact)	0.3–0.6	$0.00^{+0.00}_{-8.03}$	2.40×10^{48}
5 (compact)	0.3–0.6	< 0.29	3.20×10^{48}
6 (compact)	0.3–0.6	< 1.90	2.69×10^{50}
7 (compact)	0.3–0.6	< 0.85	9.02×10^{46}
8 (weak)	0.3–0.6	< 1.92	8.89×10^{48}
9 (weak)	0.3	$6.86^{+1.09}_{-1.01}$	1.33×10^{50}

Note. — The escape fraction of ionizing photons and adopted covering factor for each SF regions in NGC 4214.

[a] Numbering for each SF region with its noticeable Hα morphology.

[b] The covering factor from Hermelo et al. (2013).

[c] The escape fraction along the line-of-sight.

ization ($\dot{N}_{\rm gas}$), and ionizing photons absorbed by dust ($f_{\rm cov} \times \dot{N}_{\rm dust}$). We then compute the global escape fraction using Equation 2.12.

The global escape fraction varies from 2.65% to 21.03% based on the choice of $f_{\rm cov}$ values, with a median value of ~11.84%. The lowest value is obtained when assuming a conservative high $f_{\rm cov}$ of 0.6 across the entire galaxy. This lowest escape fraction is higher by a factor of ~13 than the previous measurement (Grimes et al. 2009). The discrepancy between these two studies indicates how significantly traditional approaches based on spatially-averaged spectroscopy or imaging can result in underestimating the escape fraction.

We also calculate the global escape fraction for the dust-free case. The dust-free $f_{\rm cov}$ value provides an approximation of the value for high-z counterparts of NGC 4214 during cosmic reionization. A galaxy like NGC 4214 at the epoch of reionization would have lower metallicity, leading to lower dust content. Thus, this extreme dust-free case is not totally unrealistic. The global escape fraction for the dust-free case is ~46%, releasing $\sim 1.11 \times 10^{52}$ ionizing photons per second.

2.7.3 Uncertainty in the Escape Fraction Measurement

We evaluate the uncertainties for the $f_{\rm esc}$ measurement. There are three dominant sources for the uncertainty: sed fitting, continuum subtraction from narrow-band images, and choice of covering factor.

First, we estimate the uncertainty from SED fitting. The BEAST provides 1D PDFs both for $\dot{N}_{\rm int}$ and $\dot{N}_{\rm dust}$ for individual stars. In a given SF region, we draw these values 10,000 times for all star inside that SF region based on their PDFs, resulting in 10,000 measurements of the escape fraction. To get the uncertainty in the escape fraction for that SF region, we compute 16th and 84th percentile values from the distribution of these 10,000 measurements. These asymmetric uncertainties are reported in Table 2.7.1.

Second, the uncertainty in $\dot{N}_{\rm gas}$ that resulting from continuum subtraction is ~11%. Because the scaling for continuum subtraction is a single value for the entire image, the uncertainty due to continuum subtraction introduces systematic error in the escape fraction measurement. The contribution of this error into the uncertainty in the escape fraction ranges from ∼1% to ∼11%.

Finally, there is an uncertainty from the choice of $f_{\rm cov}$. We note that this source of uncertainty would also systematically increase or decrease the escape fraction measurement. In this study, the $f_{\rm cov}$ values are used to properly measure the global escape fraction. Unfortunately, the uncertainty for the best-fit $f_{\rm cov}$ values are not presented in Hermelo et al. (2013). Thus, we present the global escape fraction within a range according to the choice of $f_{\rm cov}$ values listed in Table 2.7.1.

There are two additional, but minor uncertainties to these we discussed above. These are the effects of nonphotoionized diffuse gas in the galactic halo and dust scattering. In NGC 4214, the fraction of nonphotoionized gas in the total Hα emission is negligible (4%; Calzetti et al. 2004). The dust extinction we measure by modeling the observed SEDs includes both absorption and scattering. If there is no scattering, more LyC photons could reach to us. However, at the same time, no LyC photons would scatter into our direction. Since ∼83,000 individual stars basically sample ∼83,000 individual line-of-sights, we can assume our line-of-sight samplings would cancel out these two competing processes. Therefore, we neglect the uncertainties due to these two minor effects.

2.8 Summary and Future Directions

We have developed a new technique for measuring the ionizing photon escape fraction with unprecedented spatial resolution. With the aid of multi-wavelength (NUV, optical, and NIR) broad-band imaging obtained by HST, we have modeled SEDs of resolved stars within NGC 4214 to infer their intrinsic stellar properties, as well as the intervening dust. We have used these to predict the UV emission from the galaxy. We find excellent agreement with GALEX FUV measurements, giving us confidence in our estimates of LyC flux as well. We employ these fits to construct maps of ionizing photon production across the galaxy.

We have simultaneously measured the number of photons absorbed through ionization using hydrogen emission lines in HST narrow-band imaging. We combine the emission and absorption measurements to map the escape fraction across the galaxy. This new technique can be used for any well-resolved galaxy without requiring spatial averaging, simplifying assumptions about dust/ISM geometry along the line-of-sight, and challenging observations below the Lyman limit.

We find significant spatial variation in the local $f_{\rm esc}$. We also found the global $f_{\rm esc}$ of $\sim$11.84% that is $\sim$60 times higher than the previous measurement (Grimes et al. 2009), supporting the importance of sufficient spatial resolution in the escape fraction measurement.

While this current work provides the first ionizing photon escape fraction map for NGC 4214 with unprecedented spatial resolution, while also adding the sixth local measurements of $f_{\rm esc}$, we still need a larger sample to obtain a true understanding of the mechanism for escape of ionizing photons and its relationship between the escape fraction and the galactic environments (e.g., galaxy mass, star formation intensity, gas column density, metallicity). Detailed analyses of the local variation of the escape fraction are essential for understanding the degree to which physical properties of individual galaxies determine their contribution to cosmic reionization.

NGC 4214 is by no means the only system to which this approach can be applied. There are $\sim$40 galaxies within 5 Mpc that already have the needed NIR (or NUV) and optical data in the HST archive. For some of these, small additions of emission line and/or NUV (or NIR) imaging would make them natural targets for extending this work to a large sample. Stellar masses of these target galaxies range from $\sim 10^5$ to 10^9 $M_\odot$. Low mass galaxies, which are too faint to be detected at high redshift even with the JWST, would provide a particularly valuable constraint on the galaxy mass dependence of the ionizing photon escape fraction. Figure 2.23 describes the basic properties of possible target galaxies.

If galaxies indeed release ionizing photons through low-density holes, galaxies with compact star formation will tend to leak more ionizing photons, since stronger feedback, which blows the surrounding ISM out, is likely to be accompanied by stronger star formation (e.g., Heckman et al. 2011; Alexandroff et al. 2015). Numerical studies also suggest the dependence of the escape fraction on stellar feedback (e.g., Kimm & Cen 2014; Paardekooper et al. 2015). To test likely mechanisms for the escape of ionizing photons, star formation intensity and the ionization parameter are, in particular, interesting local properties to explore. Local star formation intensity can be used as an indicator of the stellar feedback strength, while ionization parameter mapping (e.g., [OIII]/[OII] or [SIII]/[SII] map as a proxy) traces optical depth to ionizing photons. There have been some observational efforts to find any

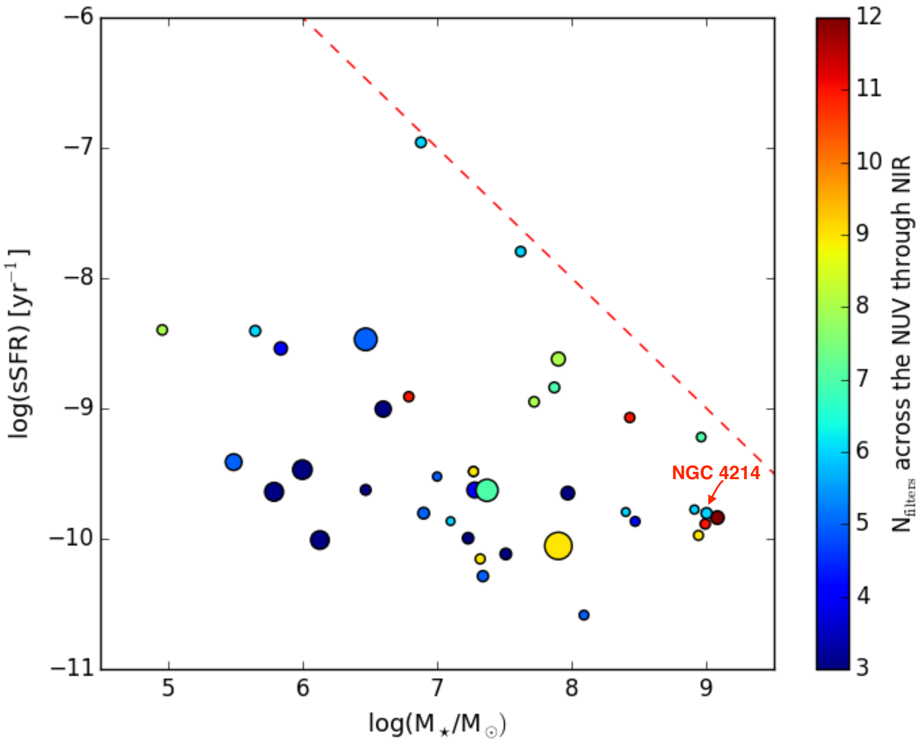

Figure 2.23 Properties of 39 target galaxies including NGC 4214. Stellar mass vs. specific star formation rate, color-coded by the numbers of any HST observation across the NUV through NIR. Symbol size is inversely proportional to distance to the galaxy. The red-dashed line shows an extrapolation of the mass-sSFR relation for green pea galaxies (M $\sim 10^{8.5} - 10^{10}$ $M_\odot$with the lowest SFR of $M_\odot$ yr^{-1}; Cardamone et al. 2009) to lower-mass galaxies. Nearby dwarf galaxies have lower stellar mass, metallicity, and emission-line flux than green peas. Galaxies that are covered entirely with the full wavelength coverage from NUV to NIR would be the best laboratories.

trends between the ionizing photon escape fraction and other physical galactic properties, such as ionization state, galaxy mass, and star formation surface density (e.g., Nakajima & Ouchi 2014; Alexandroff et al. 2015). However, the actual relationships remain inconclusive due to the small samples of galaxies with measured escape fractions. Adding escape fraction measurements for $\sim$40 nearby dwarf galaxies would alleviate the small number statistics.

Furthermore, spatially-resolved escape fraction maps will sample a variety of local environments (e.g., star formation intensity and gas surface density) even within a single galaxy. By comparing the local escape fraction to various local physical properties in individual small regions for our entire nearby galaxy sample, we will obtain enough data points to perform detailed statistical analyses. Therefore, with maps of the escape fraction for nearby galaxies, it would be possible to draw statistically meaningful conclusions, and establish robust relationships between the escape fraction and other physical properties. If we find any strong relationships, we will then estimate the escape fractions for LyC leakers at higher redshifts using those relationships.

M31, imaged from HST in 6-filters from the UV through NIR (PHAT; Dalcanton et al. 2012), offers an additional system that would allow even more detailed analyses. Although M31 is not an analog of early star-forming galaxies, it is a large well-resolved ($\sim$117 million stars; Williams et al. 2014) galaxy containing a range of star formation intensities and metallicity. Due to its proximity, M31 also has been mapped in many other wavelengths. This large set of ancillary data for M31 provides rich information about local ISM properties, and thus helps us to better understand the process of local ionizing photon leakage.

Such a project could provide strong observational constraints on the escape fraction of ionizing photons, one of the critical final pieces of the cosmic reionization puzzle.

Chapter 3

SPIRAL ARMS IN M81

This chapter was published as Y. Choi et al. 2015, ApJ, 810, 9, and is reproduced by permission of the AAS.

Stationary density waves rotating at a constant pattern speed Ω_P would produce age gradients across spiral arms. We test whether such age gradients are present in M81 by deriving the recent star formation histories (SFHs) of 20 regions around one of M81's grand-design spiral arms. For each region, we use resolved stellar populations to determine the SFH by modeling the observed color-magnitude diagram constructed from archival *Hubble Space Telescope* F435W and F606W imaging. Although we should be able to detect systematic time delays in our spatially resolved SFHs, we find no evidence of star formation propagation across the spiral arm. Our data therefore provide no convincing evidence for a stationary density wave with a single pattern speed in M81, and instead favor the scenario of kinematic spiral patterns that are likely driven by tidal interactions with the companion galaxies M82 and NGC 3077.

3.1 Introduction

More than half of the galaxies in the Local Universe show spiral patterns highlighted by young stars (e.g., Nair & Abraham 2010; Lintott et al. 2011). However, the origin of these patterns remains an open question. Several theories have been suggested to explain the underlying mechanisms connecting spiral patterns and star formation. Two models in particular are the most widely accepted: the global density wave theory for long-lived arms (Lindblad 1960; Lin & Shu 1964) and the local gravitational instability model for short-lived transient arms (e.g., Goldreich & Lynden-Bell 1965; Julian & Toomre 1966; Sellwood & Carlberg 1984; Sellwood 2011; Elmegreen 2011). The density wave theory explains active star formation in the coherent spiral arms as being a result of gas compression by a density wave propagating through a galactic disk. In contrast, the local gravitational instability model predicts that star formation is stochastic, showing no clear age gradients across the spiral arm. However, a wide range of observed appearances of spiral structures, from grand-design to flocculent, implies that a single model may not fully explain the formation and evolution of all type of spiral patterns. For a detailed review of spiral structures, we refer the reader to Dobbs & Baba (2014) and references therein.

Although multiple mechanisms may be responsible for the variety of spiral patterns observed, it is straightforward to test the spiral density wave theory in individual systems. Specifically, one should be able to find a systematic spatial ordering among SF/gas tracers with different timescales (e.g., H I for the cold dense gas, 24 μm for obscured stars, and Hα for the young stars) within spiral arms that are supported by quasi-static density waves (Roberts 1969). In this model, one assumes that density waves are propagating through a galactic disk with a constant angular pattern speed, and that the corotation radius, $R_{\rm cr}$, is defined to be where the spiral pattern speed becomes the same as the rotational speed of the disk. Inside $R_{\rm cr}$, materials move faster than the density waves, and vice versa outside $R_{\rm cr}$. When atomic or diffuse gas enters into a spiral arm (i.e., falling into a spiral potential well), it experiences a shock. The resulting compression naturally leads to the formation of molecular clouds, enhancing star formation. Newly formed stars disperse the surrounding molecular clouds through stellar feedback and continue to move away from the spiral arm. The resulting signature of this process is a spatial sequence of cold molecular gas, obscured star formation, massive young O/B stars, and evolved stars from the upstream to the downstream inside $R_{\rm cr}$, and the same sequence, but with the opposite angular variation, outside $R_{\rm cr}$.

With grand-design spiral galaxies, many efforts have been made to measure such angular offsets among different SF/gas tracers. However, findings and conclusions on the angular offsets have conflicted even for the same galaxies (e.g., M51 and M74). While Foyle et al. (2011) found no evidence for a systematic ordering of different tracers in these galaxies, Tamburro et al. (2008) and Egusa et al. (2009) detected the expected systematic angular offsets as a function of galactic radius. However, the amplitudes of the measured angular offsets are different from each other and thus the estimated timescales for the total star formation processes are also different. For example, Tamburro et al. (2008) and Egusa et al. (2009) reported different SF timescales of 1–4 Myr and 5–30 Myr based on the angular offset measurements between H I and 24 μm and CO and Hα, respectively. Among various possible causes for the differences, Louie et al. (2013) showed that the discrepancies are mainly caused by differences in the choice of SF/gas tracers used to measure the angular offsets. They also concluded that CO emission traces the compressed gas better than H I 21 cm emission, since a portion of H I emission may come from the photo-dissociated gas rather than the direct precursor of SF. In addition, 24 μm emission may also be contaminated by the underlying older stellar populations, which are not associated with the recent SF activity (e.g., Murphy et al. 2011; Leroy et al. 2012).

In this work, we test the density wave theory by looking for evidence of star formation propagation across the spiral arm in M81 using CMD-based SFH analysis, rather than using angular offset measurements among different SF/gas tracers. This approach avoids any complications related to the choice of SF/gas tracers or to the details of emission peak finding techniques and angular offset measurements from observations of gas emission.

We carry out this analysis in M81, which is one of the largest disk galaxies in the Local Volume. It is nearly face-on ($i = 59°$; de Blok et al. 2008) and has 2 symmetric grand-design spiral arms with low foreground extinction ($A_V = 0.266$; Schlegel et al. 1998). Thus, M81 is a good laboratory to test theories of spiral formation in detail. To compare our SFH analysis with predictions from the density wave theory, we adopt a high quality H I rotation curve from THINGS (de Blok et al. 2008) and explore a variety of pattern speeds reported in the literature for M81. The average of the $R_{\rm cr}$ values found in the literature is ~11.24 kpc (see Table 3.1), and the corresponding pattern speed is ~19 km s^{-1}kpc^{-1} when combined with the rotation curve. Throughout this paper, we assume a distance of ~3.8 Mpc (i.e., $m - M = 27.9$), which was derived based on deep resolved photometry of the outer disk of M81 (Williams et al. 2009). At this this distance, an angular separation of $1''$ corresponds to physical distance of ~18.5 pc.

In Section 3.2, we briefly describe properties of the M81 imaging data used in this study. Section 3.3 gives a description of our methodology for deriving the spatially-resolved SFH of spiral arms. In Section 3.4, we present and discuss our results. We summarize our

Table 3.1. A list of $R_{\rm cr}$ values for M81 found in the literature. Since different measurements were made under different assumptions about distance to M81, we converted all values to those at the distance of 3.8 Mpc. The mean $R_{\rm cr}$ is ∼11.24 kpc.

Reference	$R_{\rm cr}$ (kpc)
Gottesman & Weliachew (1975)	12.26–13.25
Rots (1975)	12
Roberts et al. (1975)	11.5
Visser (1980)	13
Sakhibov & Smirnov (1987)	>12.86
Elmegreen et al. (1989)	9.84
Lowe et al. (1994)	10.52
Westpfahl (1998)	9.8
Kendall et al. (2008)	12.67
Tamburro et al. (2008)	9.23
Feng et al. (2014)	9.5

conclusions in Section 3.5.

3.2 Data

We use 29 fields of optical M81 archival data (Proposal ID 10584; Zezas). All fields were imaged in at least two filters (F435W and F606W, including some F814W observations in outer fields). These fields are contiguous and cover the entire optical extent of the galaxy. After making bias and flat-field corrections using the STScI ACS pipeline OPUS, photometry was performed with the ANGST pipeline (Dalcanton et al. 2009). The pipeline is optimized for stellar photometry on ACS images using the ACS module within the DOLPHOT photometric package (Dolphin 2000). Briefly, the cosmic rays were identified on a combined single drizzled image using the `multidrizzle` task (PyRAF; Koekemoer et al. 2003) before measuring flux of individual stars. DOLPHOT modifies the Tiny Tim PSF (Krist 1995) to account for the effects on the PSF shape of the telescope temperature changes during orbit. To quantify systematic differences between the model and true PSF, DOLPHOT determines aperture corrections using the most isolated stars in each field. A detailed description of the photometry technique can be found in Dalcanton et al. (2009). The final catalog utilized in this study contains objects flagged as stars with S/N > 4 in both F435W and F606W filters that pass the sharpness cuts, $(\texttt{sharp}_{\rm F435W} + \texttt{sharp}_{\rm F606W})^2 < 0.075$, and the crowding cuts, $\texttt{crowd}_{\rm F435W} + \texttt{crowd}_{\rm F606W} < 0.6$. These cuts ensure high quality photometry by selecting point-like sources that are not significantly affected by crowding (Gogarten et al. 2009). Using DOLPHOT, we also perform artificial star tests to estimate photometric completeness and uncertainties as a function of magnitude.

We use the H I image from THINGS (Walter et al. 2008) to identify the location of M81's gaseous spiral arms. THINGS provides high-quality 21 cm emission line maps with an angular resolution of $\sim 6''$ and spectral resolution of 2.6 km s^{-1}. The beam size of the robust weighted H I maps is $\sim 7''.5$, corresponding to ~140 pc at the distance of 3.8 Mpc. Figure 3.1 shows the H I map overlaid with the footprints of 29 HST fields. We also use the Hα (KPNO; Hoopes et al. 2001) and 24 μm (Spitzer; Dale et al. 2009) images to provide a quick comparison between gas/SF tracers in Section 3.3.1 (see Figure 3.2).

3.3 The Spatially Resolved Star Formation History

3.3.1 Defining Spiral Arms and Selection of Stars

To define the spiral arms, we first deproject the H I image assuming a position angle of 330° and inclination of 59° (de Blok et al. 2008) (left panel in Figure 3.2) and then select density maxima positions by picking the center of contours within the spiral arms. After translating each (x, y) position to polar coordinates (r, θ), we fit the selected density maxima positions with a logarithmic function of the form $\ln(r) = \ln(a) + b\,\theta$. The azimuthal angle (θ) increases with the direction of galactic rotation, which is counterclockwise for M81 since we assume a trailing spiral pattern. The pattern is almost a perfect logarithmic spiral and the derived pitch angle of the H I gas arm, $i = \arctan(|b|)$, is $\sim 15°$, which is in good agreement with

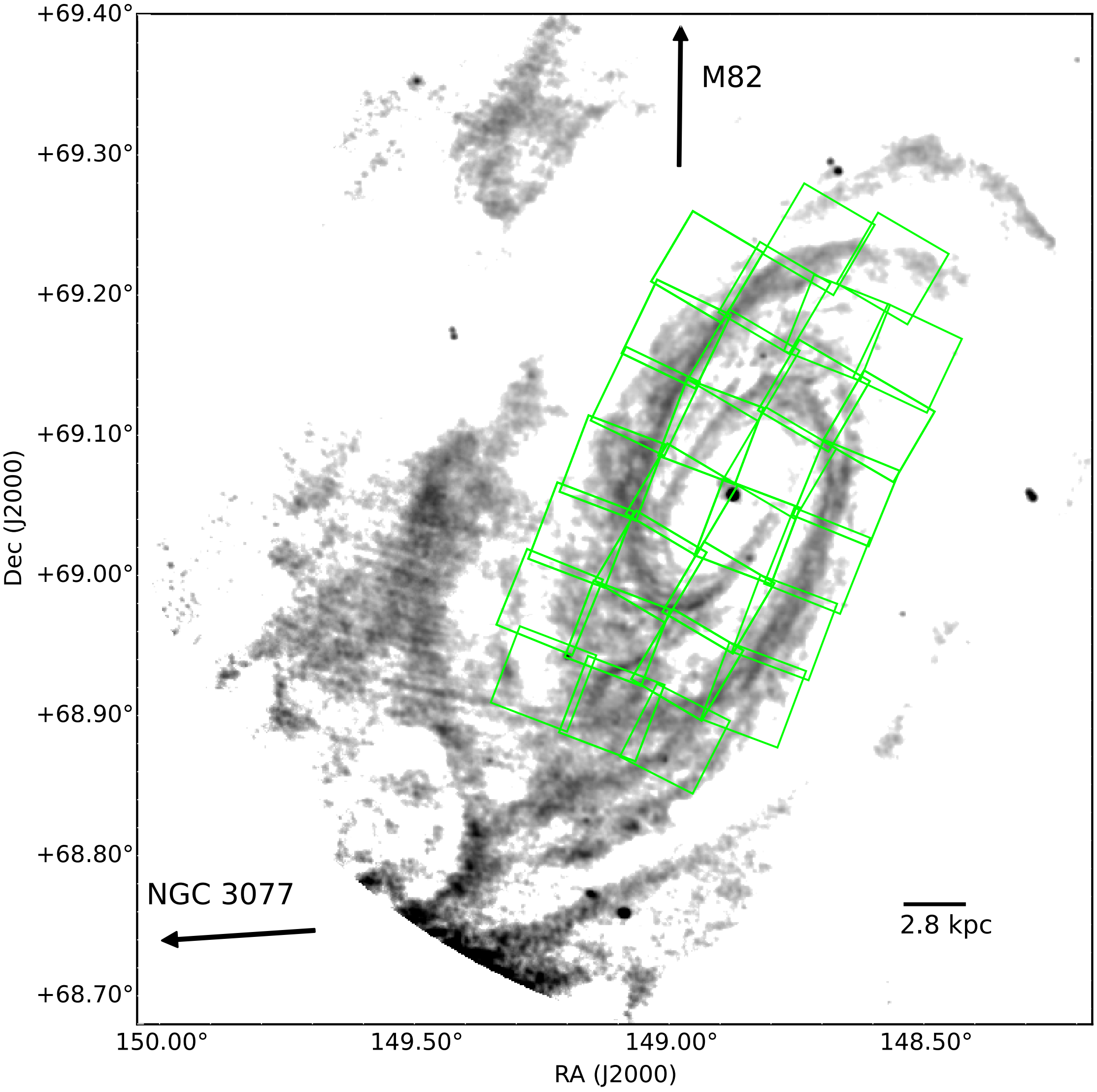

Figure 3.1 The HST footprints (green boxes) of 29 fields, which cover the entire optical extent of M81, are superposed on the H I image (THINGS; Walter et al. 2008). H I emission is extended far beyond optical emission. North is up. East is left. The arrows point out the directions toward companions, M82 and NGC 3077. Tidal bridges connecting M81 and companions are prominent while the tidal features are not seen in the optical.

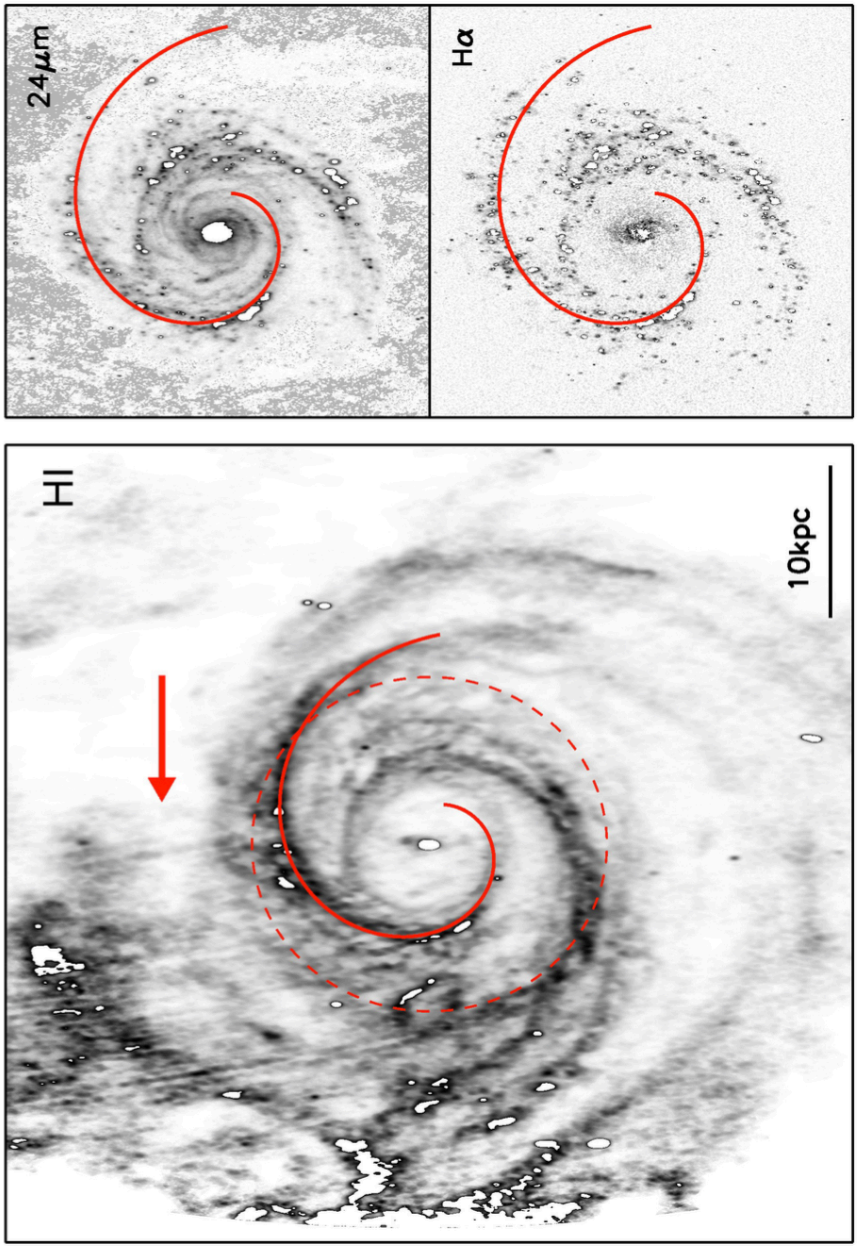

Figure 3.2 Deprojected image of M81 in H I (left, from Walter et al. 2008), 24 μm (right top, from Dale et al. 2009), and Hα (right bottom, from Hoopes et al. 2001). An arrow denotes the direction of galactic rotation when assuming a trailing spiral pattern. On each image, we overplot the best-fit logarithmic spiral pattern derived from the H I (red solid line) of the NE arm that we analyze in this work. We also mark the reported average corotation radius at ~11.24 kpc on the H I image (dashed circle).

previous studies (e.g., Rots 1975; Kennicutt 1981; Lowe et al. 1994; Puerari et al. 2014). We adopt this best-fit logarithmic spiral as the peak of the gaseous spiral arms.

M81 has 2 strong spiral arms, separated by ∼180°. We focus on the NE arm (highlighted with the red solid line in Figure 3.2), which does not have a strongly streamed feature in the H I map compared to the other stretched arm (SW arm). This choice should minimize the effects of any ongoing tidal interaction on SFH, although the SW arm has a similar pitch angle in the H I gas map. The best-fit logarithmic spiral is also overlaid on the deprojected 24 μm (right top) and Hα (right bottom) images. Although the observed peaks of both Hα and 24 μm emission are mostly seen downstream of the best-fit spiral arm, they are scattered and discrete. This observational discreteness can cause complexity and ambiguity in measuring and interpreting the angular offsets among different SF tracers. Note that in both the H I and Hα maps, the spiral pattern is hardly seen in the inner galactic region ($r \lesssim 3$ kpc), possibly indicating the inner Lindblad resonance. In contrast, the 24 μm image shows a signature of short spiral arms in the inner galactic region in addition to the grand-design spiral arms, as first recognized both in the 3.6 μm and 8 μm images by Kendall et al. (2008) and explored in more detail by Feng et al. (2014). The driving forces of these short spiral arms is beyond the scope of this paper.

Figure 3.3 shows our 20 (5 × 4) analysis regions around the best-fit logarithmic spiral arm. Individual regions are bounded by dashed circles, which denote galactic radii of ∼5.6 kpc, ∼8.4 kpc, and ∼11.2 kpc, and solid curves, which define 5 spiral-shaped stripes. These 20 regions enable us to obtain the spatially resolved SFHs around the spiral arm using sufficient numbers of stars in each region, leading to reliable SFHs. We first define 5 spiral-shaped stripes along the best-fit logarithmic spiral arm based on the perpendicular distance from the best-fit spiral arm (from –700 to +700 pc with a constant width of 280 pc). The total width of 1.4 kpc is wide enough to catch the potential age gradients across the spiral arm predicted by the density wave theory (see Section 3.4.2 for timescales of interest). Each spiral-shaped stripe is then further divided into 4 different bins based on the distance to the galactic center (from ∼2.8 kpc to ∼13.8 kpc with a constant radial length $\Delta r \sim$ 2.8 kpc). The innermost and outermost radial boundaries are chosen to limit the analysis to the regions where the bulge components are negligible and the spiral pattern is clear.

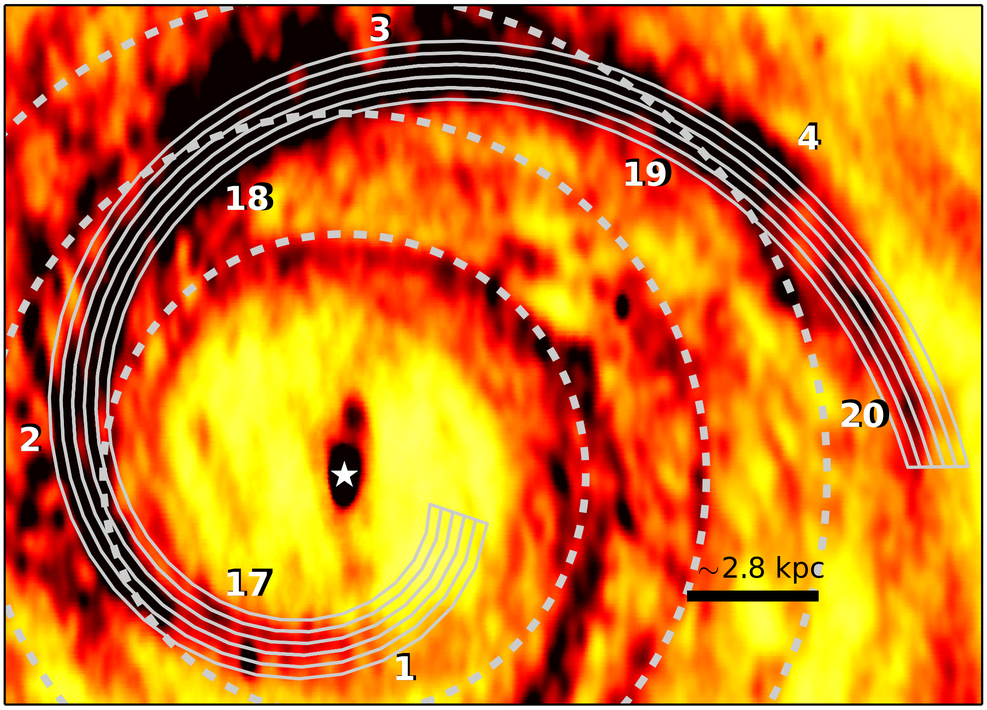

Figure 3.3 The 20 analysis regions around the spiral arm are overlaid on the deprojected H I map. Individual regions are bounded by dashed circles and solid curves. Dashed circles are located at ~5.6 kpc, ~8.4 kpc, and ~11.2 kpc from the galactic center. To clarify our numbering system, we show nominal numbers for regions located at the most leading and most trailing stripes.

By choosing $\Delta r \sim 2.8$ kpc, the boundary between the third and the fourth bins is aligned with the reported average R_{cr} of ∼11.24 kpc, and thus the fourth bin is likely outside R_{cr}. Therefore, in the case of $\Omega_{\rm P} = 19$ km $\rm s^{-1}kpc^{-1}$, one can avoid the potential ambiguity arising from the coexistence of two oppositely propagating SF within a single bin. However, for a pattern speed faster (slower) than 19 km $\rm s^{-1}kpc^{-1}$, corotation radius lies within the third (fourth) radial bin. We assign nominal numbers to these 5 × 4 regions. Smaller numbers are assigned to stripes with larger azimuthal angle (i.e., the leading side within $\rm R_{cr}$, but the trailing side beyond $\rm R_{cr}$). Within each stripe, the numbers increase with increasing galactic radius.

The numbers of stars, 50% photometric completeness limits (derived from artificial star tests), and the areal coverage for individual regions are listed in Table 3.2. All regions have almost the same depth and similar areal coverage (2–3 $\rm kpc^2$). The observed CMDs of each region are shown in Figure 3.4. Each column represents different radial bins, with galactic radius increasing from the left to the right columns. Each row represents different spiral-shaped stripes. The azimuthal angle decreases from top to bottom. For example, when adopting $\Omega_{\rm P} = 19$ km $\rm s^{-1}kpc^{-1}$, in the first 3 columns that are the radial bins likely inside $\rm R_{cr}$, top panels are for the leading side of the arm and bottom panels are for the trailing side of the arm, and vice versa in the last column, which is the radial bin likely outside $\rm R_{cr}$.

3.3.2 Deriving the Star Formation Histories

In all regions, there are sufficient main sequence stars for age-dating. The SFH of each region is derived using the MATCH package (Dolphin 2002), which has been applied to many studies (e.g., Williams et al. 2009; Gogarten et al. 2009; McQuinn et al. 2010; Williams et al. 2011; Weisz et al. 2011; McQuinn et al. 2012; Weisz et al. 2014; Lewis et al. 2015). The fundamental principle behind MATCH is to find a set of synthetic CMDs that best reproduce the observed CMD, using a maximum likelihood method assuming Poisson-distributed data. We use the Padova isochrone set (Girardi et al. 2002) with updated models (Marigo et al. 2008; Girardi et al. 2010) for the CMD fitting. In the actual fitting process, stars brighter than a 50% completeness limit are used. We run MATCH with a fixed distance of $m - M =$

Table 3.2 Numbers of stars, 50% photometric completeness limits in F435W and F606W bands, the areas covered, and the best-fit $A_{\rm V}$ and $dA_{\rm V}$ values for individual regions.

Region	N$_{stars}$	F435W (mag)	F606W (mag)	Area (kpc^2)	Av (mag)	dAv (mag)
1	14,850	27.07	26.93	2.93	0.30	0.9
2	22,650	27.15	27.02	3.11	0.30	0.8
3	18,476	27.30	27.26	3.05	0.30	0.4
4	6,578	27.49	27.48	3.41	0.25	0.1
5	16,776	27.00	26.84	3.03	0.35	0.5
6	15,978	27.20	27.07	3.01	0.40	0.8
7	16,729	27.31	27.28	2.95	0.35	0.5
8	6,288	27.50	27.49	3.06	0.20	0.3
9	17,326	27.02	26.90	3.12	0.20	0.8
10	12,488	27.25	27.15	2.90	0.35	1.1
11	12,438	27.37	27.34	2.84	0.30	0.6
12	4,801	27.50	27.51	2.70	0.25	0.2
13	11,942	27.06	26.89	3.17	0.30	0.9
14	13,220	27.23	27.12	2.75	0.45	0.8
15	7,656	27.40	27.35	2.80	0.35	0.4
16	3,350	27.55	27.57	2.36	0.20	0.3
17	12,879	27.06	26.90	3.18	0.35	0.6
18	14,890	27.21	27.13	2.65	0.35	1.0
19	6,351	27.43	27.39	2.71	0.20	0.6
20	2,983	27.61	27.58	2.01	0.15	0.6

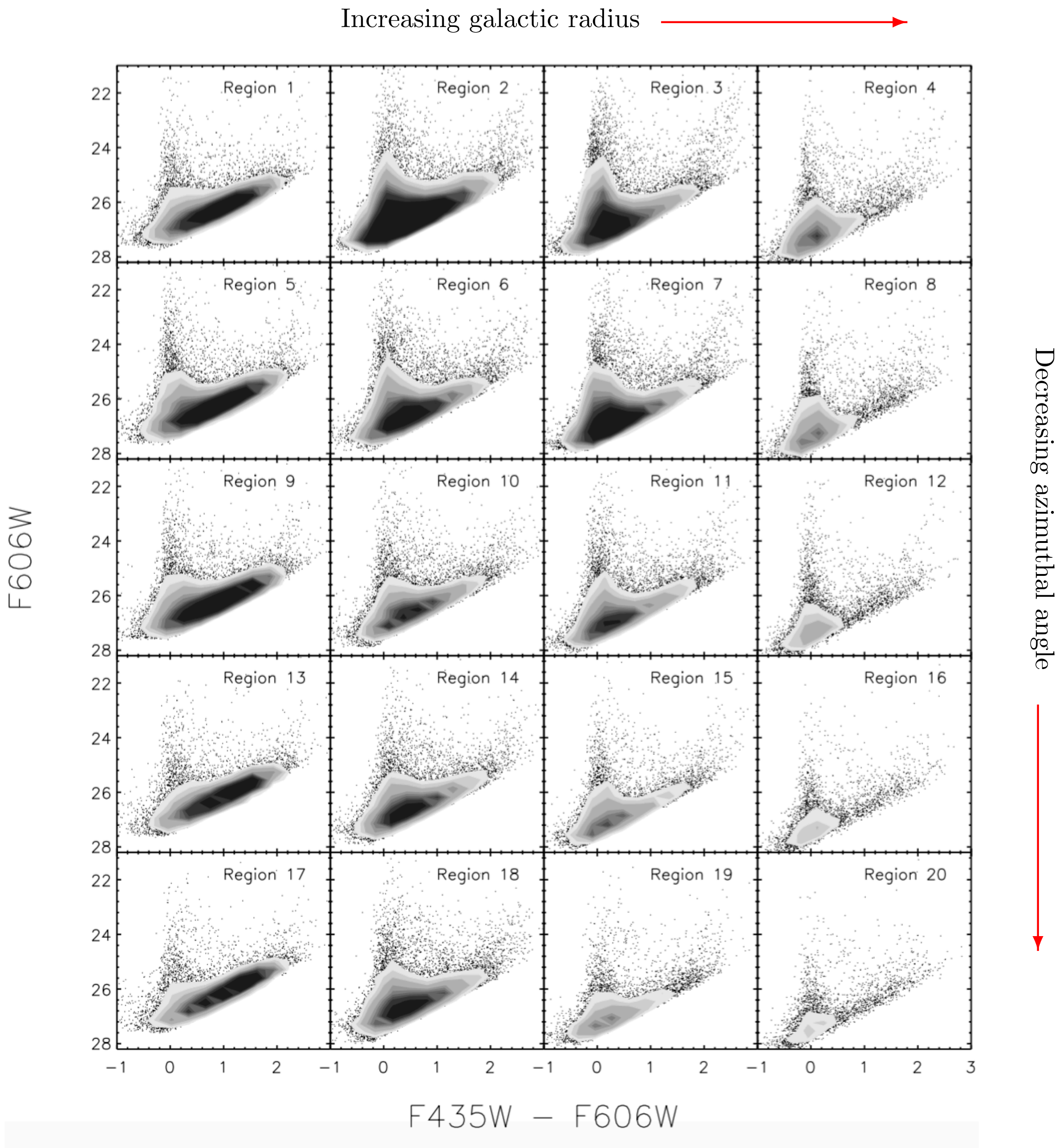

Figure 3.4 Observed CMDs of 20 regions. Each column represents the different radial bins in the spiral arm. The galactic radius increases from left to right. Within each radial bin, azimuthal angle decreases from top to bottom panels. All CMDs have significant populations of upper main sequence stars, which are critical for constraining recent SFH.

27.9, a Kroupa initial mass function (Kroupa 2001), and a binary fraction of 0.35, and then solve for the best-fit foreground extinction (A_V), differential extinction (dA_V, internal to the galaxy), and linear combination of SFR and [Fe/H] as a function of age. We allow the foreground extinction to range from 0.05 to 0.55 mag with a step size of 0.05 mag and the differential extinction to range from 0 to 1.5 mag with a step size of 0.1 mag.

We use equally spaced logarithmic time bins between log(t/yr) = 6.6 and 10.15 with an increment of 0.15 dex. In addition, we require the metallicity to increase monotonically with time, since the observed CMDs are dominated by the upper main sequence which contains little information to constrain metallicity. This metallicity constraint enables us to derive a SFH with a physically plausible metallicity evolution. We estimate the random uncertainties of SFHs by using the Hybrid Monte Carlo (MC) sampling technique described in Dolphin (2013). By creating random samples following the probability density of SFH solutions, the Hybrid MC technique overcomes the issue seen in uncertainties computed from the traditional bootstrap MC resampling, which underestimates the random uncertainties of SFH for time bins with low or zero SFR. The systematic uncertainties, which are dominated by the uncertainty in stellar evolution models (Dolphin 2012), are only important when comparing the absolute SFH to other galaxies or simulations, but can be safely ignored when comparing regions where CMDs have similar depths within a single galaxy, since all regions will be affected similarly.

Figure 3.5 presents an example of the best-fit CMD from MATCH, along with the observed CMD, the residual after subtracting the model from the data, and the residual weighted by the variance in each CMD bin (residual significance CMD; see Dolphin 2002). Good agreement between the model CMD and the observed CMD indicates that the derived SFH is acceptable. The best foreground extinction and differential extinction fits are given in the last two columns in Table 3.2. The mean of the best foreground extinction fits is 0.295 mag, and it is consistent with the value of $A_V = 0.266$ mag from Schlegel et al. (1998). The mean of the best differential extinction fits is 0.61 mag. The highest differential extinction value (~1 mag) in each stripe is found in the second radial bin where dust emission is strongest within the arm (Herschel; Bendo et al. 2010). Without considering differential extinction, we found the best-fit $A_V = 0.45$, which is consistent with the value that was found for the arm region in Williams et al. (2009), in which differential extinction was not taken into account.

3.4 Result and Discussion

3.4.1 Recent Star Formation History

All regions show similar SFHs at ages > 0.2 Gyr within the uncertainties, as would be expected if old stellar populations have been well mixed azimuthally on timescales longer than the dynamical time and/or mixed radially through radial migration (e.g., Sellwood & Binney 2002; Haywood 2008; Roškar et al. 2008). Fortunately, the timescales in which we are interested are less than $\sim$0.15 Gyr; M81 has a rotation speed of $\sim$230 km s^{-1}, and a reported pattern speed ranging from $\sim$17–25 km $s^{-1}kpc^{-1}$ (Gottesman & Weliachew 1975; Rots 1975; Roberts et al. 1975; Visser 1980; Sakhibov & Smirnov 1987; Elmegreen et al. 1989; Lowe et al. 1994; Westpfahl 1998; Kendall et al. 2008; Tamburro et al. 2008; Feng et al. 2014). Given the width of our defined spiral arm, we expect stars to move through our analysis region in less than $\sim$150 Myr at all galactic radii, even where the relative velocity between the density wave and the material is modest ($\sim$30 km s^{-1}). Therefore, we focus only on the recent SFHs.

Figure 3.6 shows the SFHs of individual regions during the past 150 Myr. In general, the overall SF is weaker at the outer two radial bins, most likely due to the low gas surface density (i.e., the decline in the gas surface density with galactic radius). In the outermost radial bin, a weaker shock might also be responsible for lower SFR around the corotation radius, due to the small relative speed between the gas and the density wave, if it exists. For clarity, we multiply SFRs of the outermost radial bin (last column panels in Figure 3.6) by 5. The dashed line indicates the average SFR over the past 150 Myr in each region. All regions show clear evidence of young stars.

3.4.2 Star Formation Propagation

Density wave theory predicts age gradients across spiral arms. Dobbs & Pringle (2010) explored the spatial distribution of young star clusters with different ages ($\sim$2–130 Myr) for

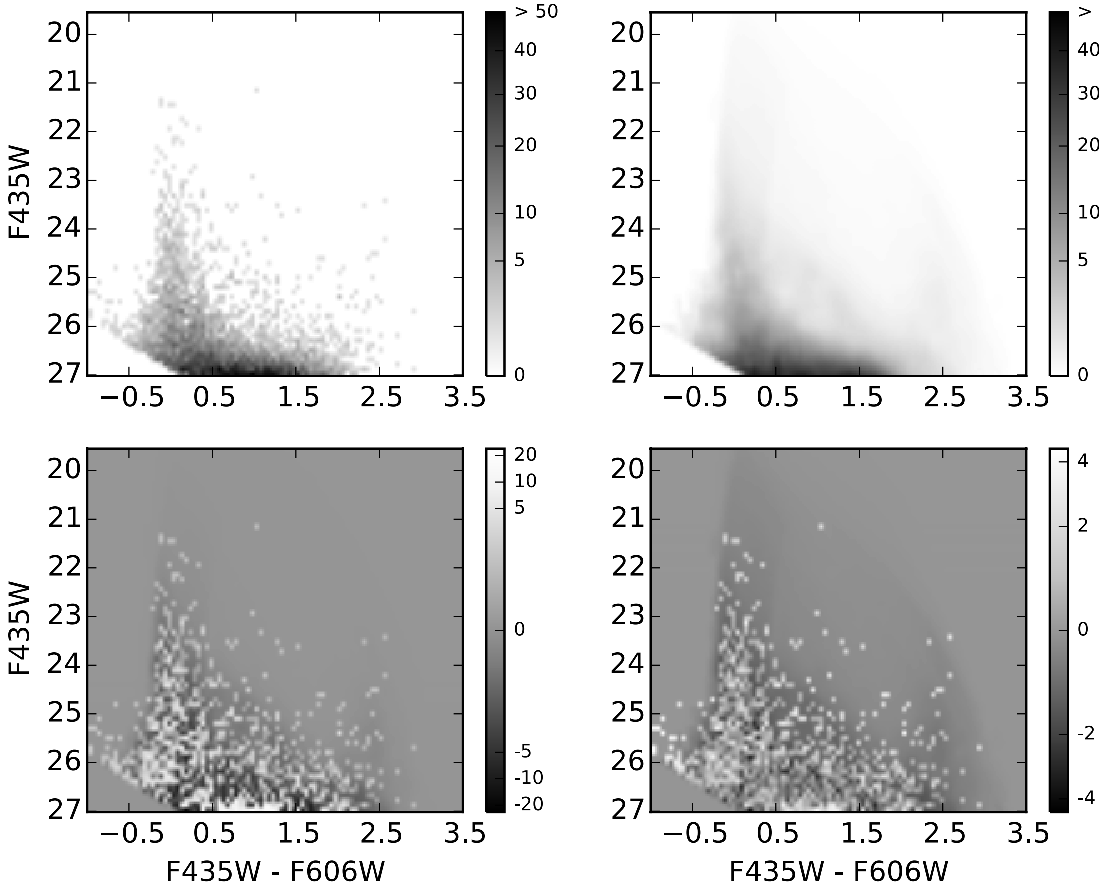

Figure 3.5 Example of the best-fit CMD from MATCH. Upper left: the observed CMD. Upper right: the best-fit model CMD. Bottom left: the residual of data-model CMD. Brighter colors for CMD bins where the model underproduce stars. Bottom right: the residual significance (i.e., variance-weighted residual).

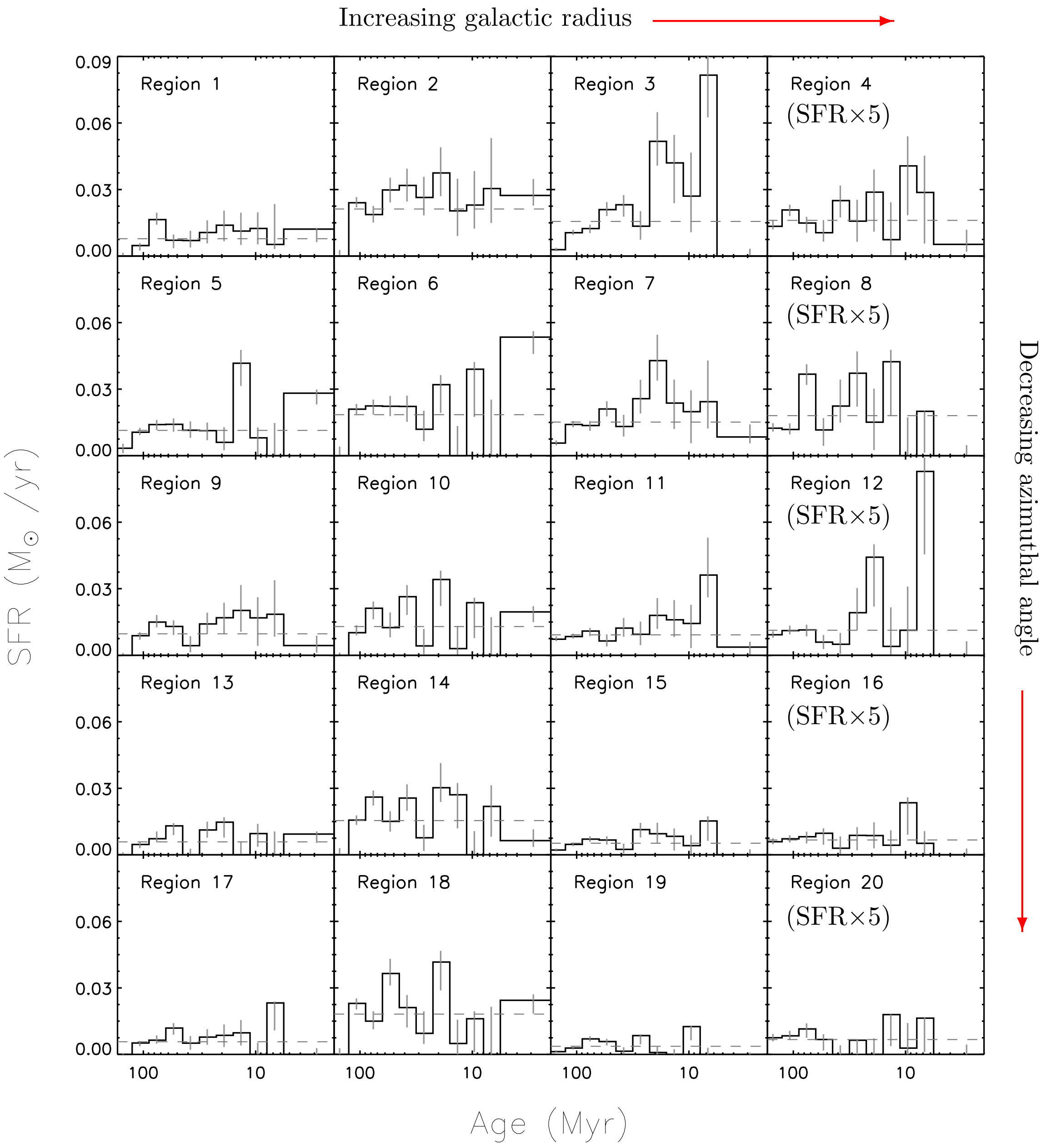

Figure 3.6 The SFHs over the past 150 Myr. Panel order is the same as Figure 3.4. For clarity, we multiply SFRs of the outermost radial bin (last column panels) by 5. The dashed line marks the average SFR over the past 150 Myr in each region.

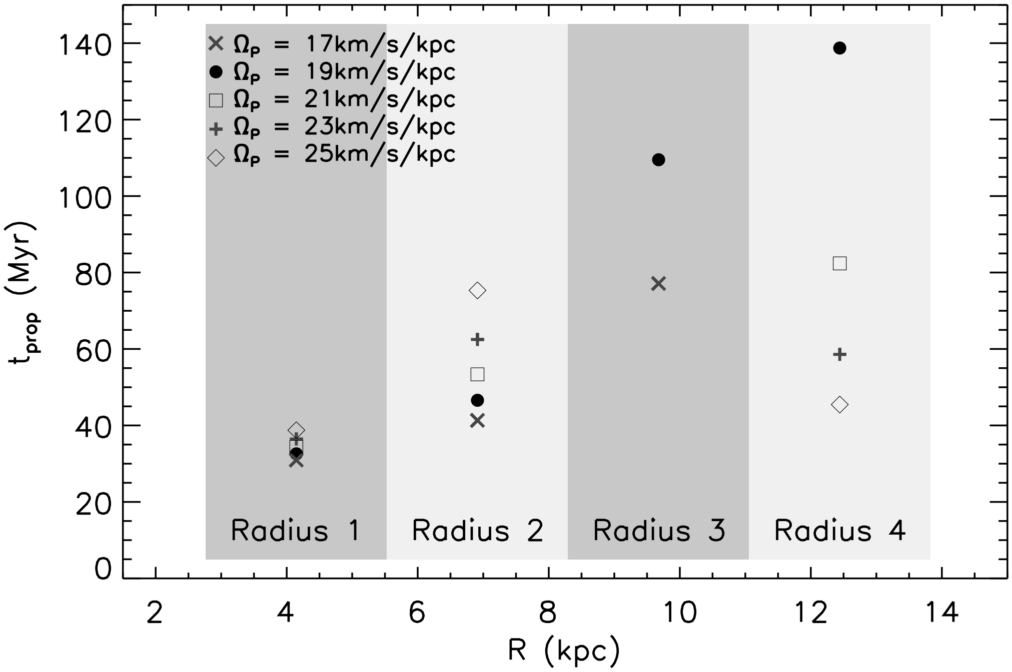

Figure 3.7 Predicted timescale of SF propagation across the entire 5 spiral-shaped stripes as a function of galactic radius, for a variety of pattern speeds: 17 km $s^{-1}kpc^{-1}$ (crosses), 19 km $s^{-1}kpc^{-1}$ (filled circles), 21 km $s^{-1}kpc^{-1}$ (open squares), 23 km $s^{-1}kpc^{-1}$ (pluses), and 25 km $s^{-1}kpc^{-1}$ (open diamonds). Shaded boxes denote the extents of the four radial bins. For $\Omega_{\rm p}$ = 19 km $s^{-1}kpc^{-1}$, corotation occurs at ∼11.24 kpc, which is well aligned with the boundary between the third and fourth radial bins. For $\Omega_{\rm p}$ = 17 km $s^{-1}kpc^{-1}$, corotation radius lies within the fourth radial bin while corotation radius for the other three pattern speeds (21, 23, and 25 km $s^{-1}kpc^{-1}$) lies within the third radial bin.

four different galaxy models; a galaxy with a stationary density wave, a barred galaxy, a flocculent galaxy, and an interacting galaxy. Their model galaxy with a stationary density wave shows an obvious trend in age of star clusters across its spiral arm, which is a clearly differentiated feature from their other model galaxies. If M81's spiral pattern is truly driven by a traditional density wave, then we expect to find a peak in SF that shifts in age as one moves azimuthally away from the spiral arm. The direction of the shift in age, and its amplitude, depends on the relative angular velocity between the gas and the density wave, which itself depends on galactic radius.

To explore whether the recent SFHs of M81's spiral arm are consistent with SF propagation predicted by a steady density wave with a single pattern speed, we compare the derived SFHs with the expected age trend across the spiral arm in each radial bin for a given single pattern speed. The expected timescale ($\Delta\, t$) for a given width of azimuthal angle ($\Delta\theta$) is estimated based on a given single pattern speed and the rotation curve amplitude ($\mathrm{V_C}(r) \approx$ 200–250 km s^{-1} at the radii we analyze; de Blok et al. 2008):

$$\Delta\, t(r) \quad = \quad \frac{\Delta\theta\,(r)}{\Omega\,(r) - \Omega_{\,\mathrm{p}}}\,, \tag{3.1}$$

where $\Omega\,(r) \equiv \frac{V_{\mathrm{C}}(r)}{r}$.

Figure 3.7 shows the estimated timescale for SF to propagate through the width of each analysis regions as a function of galactic radius for 5 different pattern speeds, $\Omega_{\,\mathrm{p}} = 17$, 19, 21, 23, and 25 km $\mathrm{s}^{-1}\mathrm{kpc}^{-1}$. In principle, the timescales varies with galactic radius such that it increases toward the $\mathrm{R_{cr}}$, becomes infinity at the $\mathrm{R_{cr}}$, and decreases beyond the $\mathrm{R_{cr}}$. The direction of the SF propagation outside $\mathrm{R_{cr}}$ is expected to be opposite to that inside $\mathrm{R_{cr}}$. In the case of $\Omega_{\,\mathrm{p}} = 19$ km $\mathrm{s}^{-1}\mathrm{kpc}^{-1}$, $\mathrm{R_{cr}}$ is well aligned with the boundary between our third and fourth radial bins, and thus we are able to calculate the average timescales to cross our defined spiral arm in all radial bins, which are about 32 Myr, 47 Myr, 109 Myr, and 137 Myr for each radial bin (from inner to outer). These timescales are long enough for SF to emerge from dense molecular clouds, which is believed to occur on timescales of ∼5–30 Myr (e.g., Elmegreen 2000; Ostriker et al. 2001; Egusa et al. 2009). However, as we mentioned above, for a pattern speed faster (slower) than 19 km $\mathrm{s}^{-1}\mathrm{kpc}^{-1}$, $\mathrm{R_{cr}}$ lies within the third (fourth) radial bin. When $\mathrm{R_{cr}}$ falls within one of our radial bins, we expect two waves of SF propagating in opposite senses in that single radial bin. Thus, we do not provide the expected timescales for that radial bin (third bin for $\Omega_{\rm p} = 21$, 23, 25 km $\rm s^{-1}kpc^{-1}$, and fourth bin for $\Omega_{\rm p} = 17$ km $\rm s^{-1}kpc^{-1}$) due to the ambiguity mentioned in Section 3.3.1.

Because of the uncertainty in the pattern speed and the fact that we do not know a priori in which stripe the SFR is expected to peak, we need to test for consistency with a variety of pattern speeds and possible time shifts in the onset of SF. Although our defined 20 regions cover the high-density region of the H I gaseous spiral arm, the outer edge of our trailing side stripe does not necessarily mark the spot where SF is initiated by a shock.

In Figure 3.8, we therefore compare our derived SFHs with the predicted SF propagation for 5 different pattern speeds and at least 6 different time shifts in the onset of SF to find any systematic trend in the enhanced SF peaks across the spiral arm. Each panel presents the SFHs of 5 adjacent spiral-shaped stripes within a single radial bin, with the azimuthal angle decreasing from top to bottom (i.e., from leading side to trailing side inside $\rm R_{cr}$, and vice versa outside $\rm R_{cr}$); each grayscale panel therefore corresponds to an entire column of Figure 3.6. Region numbers are given in the y-axis for clarity. The SFH of each region is normalized to its average SFR over the past 150 Myr to look for correlations between SFR enhancements and viable propagating spiral pattern models, and is presented in grayscale where darker (lighter) colors indicate higher (lower) SFR than the average SFR.

In each panel, a solid curve traces the ages of the stellar populations that are predicted to have formed right at the edge of our trailing side spiral-shaped stripe (i.e., a zero time shift in the onset of SF) and moved across the spiral arm if there were a stationary density wave with a given single pattern speed. Dashed (dotted) lines denote the positive (negative) time shifts of 10, 30, 50, 70, and 90 Myr, meaning SF occurred before (after) entering our analysis region.

Comparing the grayscale to the model lines, the enhanced SF peaks across the spiral arm show no clear systematic trend in all radii to support a steady density wave with a single pattern speed. Instead, the recent SFHs are fluctuating and stochastic. Our finding is robust against both adopting a variety of pattern speeds (i.e., the different SF propagation timescales found in each row of panels) and applying ranges of time shift in the onset of SF (i.e., the dashed and dotted lines in each panel). For the innermost radial bin, there

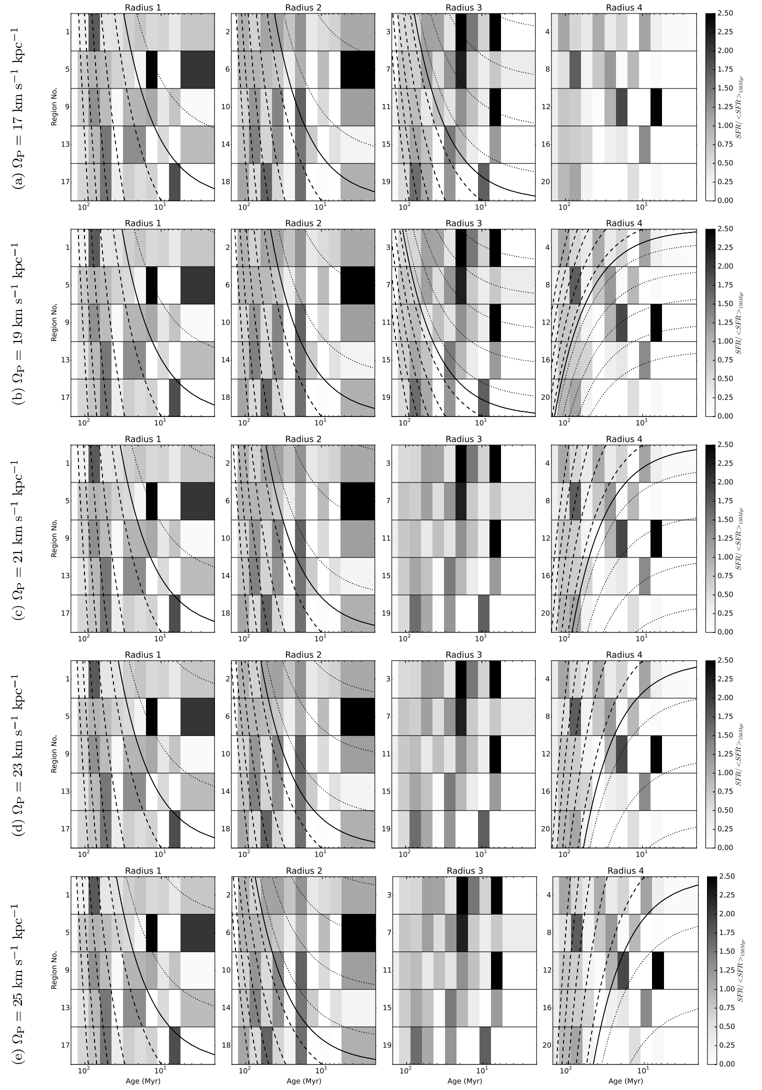

(a) $\Omega_{\rm P} = 17$ km s^{-1} kpc^{-1}

(b) $\Omega_{\rm P} = 19$ km s^{-1} kpc^{-1}

(c) $\Omega_{\rm P} = 21$ km s^{-1} kpc^{-1}

(d) $\Omega_{\rm P} = 23$ km s^{-1} kpc^{-1}

(e) $\Omega_{\rm P} = 25$ km s^{-1} kpc^{-1}

Figure 3.8 Comparison between our SFHs and the SF propagation predicted by the steady density wave theory. The comparison was carried out in individual radial bins (increasing in galactic radius from left to right) for 5 different pattern speeds (shown in each row): (a) $\Omega_{\rm p}$ = 17 km s^{-1}kpc^{-1}, (b) $\Omega_{\rm p}$ = 19 km s^{-1}kpc^{-1}, (c) $\Omega_{\rm p}$ = 21 km s^{-1}kpc^{-1}, (d) $\Omega_{\rm p}$ = 23 km s^{-1}kpc^{-1}, and (e) $\Omega_{\rm p}$ = 25 km s^{-1}kpc^{-1}. Within each panel, each row shows the SFH in a given spiral-shaped stripe; the number of the stripe refers to regions defined in Figure 3.3. The SFHs of individual regions are normalized to their average SFR over the past 150 Myr. Grayscale shows the enhanced (darker) or depressed (lighter) SF events compared to the average SFR in each region. The solid curve traces the expected dominant stellar ages across the spiral arm by assuming the onset of SF at the edge of our trailing side spiral-shaped stripe. The dashed (dotted) curves consider positive (negative) time shifts of 10, 30, 50, 70, and 90 Myr. We do not provide the predicted SF propagation in radial bins that are located at corotation, where no dominant propagation is expected. In these plots, a propagating spiral density wave would show enhanced SF that tracks one of the curves in all four radial bins of a single row corresponding to the true pattern speed. We see no evidence for this expected behavior.

is a weak trend that fits with a time shift of 50 Myr for any given pattern speed cases. However, a SFH with much higher time resolution would be required to determine which pattern speed fits the best with which time shift; our SFH time resolution, especially in older age bins, is not sufficient enough to constrain this. In addition, the amplitudes of some enhanced SF peaks associated with the trend are not strong.

A successful propagation model must also work at all radii for a single pattern speed. However, there are no clear trends in the outer radial bins that could be explained by any of these curves with the time shift of 50 Myr that possibly fits the innermost radial bin. For example, in the third radial bin, there is one possible trend that shows better agreement either with a zero time shift for $\Omega_{\rm p}$ = 17 km s^{-1}kpc^{-1} or with $\Omega_{\rm p}$ = 19 km s^{-1}kpc^{-1} with a time shift of –10 Myr. However, these trends are too weak to support any specific pattern speeds and value of time shift, and are not reflected at other radii. Thus, we detect no evidence for the age gradients that would have been expected for SF propagation by a traditional spiral density wave.

Our results agree with Schweizer (1976), and also with Foyle et al. (2011), who measured angular offsets between H I and 24 μm in M81's spiral arm, and found no systematic ordering as a function of galactic radius. Our results also agree with other recent studies that found no significant observational evidence favoring the density wave theory in other nearby grand-design spiral galaxies. For example, Ferreras et al. (2012) found no offsets between Hα and NUV-optical color in NGC 4321. Martínez-García & González-Lópezlira (2013) also failed to detect color gradients in the grand-design two-armed spiral galaxies NGC 578, NGC 1703, NGC 4603, NGC 4939, NGC 6907, and NGC 6951.

3.4.3 Tidally induced grand-design spiral arm?

The absence of a systematic trend in our recent SFHs indicates that the grand-design spiral structure of M81 is not the result of the gas response to long-lived density waves with a single pattern speed. In fact, stationary spiral waves have never been reproduced without imposing very specific conditions in numerical simulations, and spiral patterns are found to be transient/recurrent features (e.g., Sellwood 2011; Fujii et al. 2011; Wada et al.

2011; Grand et al. 2012; Baba et al. 2013; Sellwood & Carlberg 2014). D'Onghia et al. (2013) recently showed that non-linear growth of self-induced spiral structures by swing amplifiication can demonstrate 'apparent' long-lived spiral arms in their simulation of an isolated galaxy. They suggested that 'apparent' long-lived global spiral patterns are merely products of connected self-perpetuating local segments, which are in local dynamical balance between shear and self-gravity. However, the self-perpetuating spiral arms that are locally fluctuating with time do not necessarily exhibit the systematic radial dependence of the relative amplitude of spiral arms that were found in the observed mass surface density map of M81 (e.g., Elmegreen et al. 1989; Kendall et al. 2008).

A snapshot of the current bisymmetric spiral patterns of M81 might be a result of the superposition of two or more $m = 2$ modes with distinct pattern speeds (Sellwood & Carlberg 2014). If M81's grand-design spiral arms consist of the superposition of two or more modes lasting 5–10 galactic rotations, then it is reasonable to expect two or more distinct SF propagations across the spiral arm. However, we find no such features in Figure 3.8. This does not mean that we can decisively rule out this mechanism, since there are possibilities that the relevant pattern speeds are out of our search range or that the superposition of multiple modes would partially erase/overwrite the each other's age gradients, increasing complexity in the resulting SFH.

As an alternative model for grand-design two-armed galaxies, Toomre & Toomre (1972), Kormendy & Norman (1979), Hernquist (1990), and Bottema (2003) argue that all non-barred grand-design galaxies with typical rotation curves (i.e., flat rotation curves) are likely to be the result of interactions with nearby companions since they frequently reside in the interacting systems showing tidal features such as bridges and tails. These conditions fit M81; it has no strong bar, but has companion galaxies.

Such an interaction is clearly taking place in M81, making tidal interactions a compelling mechanism for driving its spiral arms. Numerical simulations (e.g., Thomasson & Donner 1993; Yun 1999) suggested tidal interactions to explain the current H I gas distribution in the M81 group (Appleton et al. 1981). According to Yun's simulation (Yun 1999), M81 underwent the closest passage about 220 Myr and 280 Myr ago by its companion galaxies M82 and NGC 3077, respectively. In addition, many observational studies (e.g., Yun et al.

1994; Chandar et al. 2001; Pérez-González et al. 2006; de Mello et al. 2008; Konstantopoulos et al. 2009; Santiago-Cortés et al. 2010; Hoversten et al. 2011; Lim et al. 2013) have found evidence for tidally induced SF in both M81 and its companion galaxies: ages of compact star clusters and star-forming regions range ∼100–500 Myr. Although we also detected enhanced SF at ages between 200 to 350 Myr in all 20 regions, the associated systematic errors are significant since the stars sensitive to this SF peak are near the 50% completeness limit of the data, and therefore this result would require additional observations to confirm with confidence.

Recent studies (e.g., Oh et al. 2008; Dobbs et al. 2010; Struck et al. 2011; Oh et al. 2015) explored the physical properties of simulated galaxies having tidally induced symmetric two-armed grand-design spiral arms. These tidally excited grand-design spirals are almost logarithmic and typically kinematic density waves, which are the result of nested elliptical stellar orbits induced by tidal perturbation. These kinematic density waves do show radial variation of their pattern speed. However, slower differential rotation than the material disk enables the kinematic spirals to survive for a timescale of ∼1 Gyr (Oh et al. 2008). Speights & Westpfahl (2011) estimated the pattern speed of M81's spiral structure and indeed detected its radial dependence, indicating the spiral pattern does actually follow differential rotation.

Although Dobbs et al. (2010) modeled M51 with an interacting companion (NGC 5195), there are some similarities that we can apply to the M81 group as well. During detailed comparison of their model galaxy to HST observations of M51, they noticed that two passages by the companion galaxy at different times are able to reproduce observed kink/bifurcations in the spiral arm besides a well-defined two-armed spiral pattern. A kink/bifurcation is formed where the younger arm, induced by the second passage, and the older arm, induced by the first passage, are connected. Since M81 is also believed to have experienced two tidal interactions separated by ∼60 Myr with two companion galaxies, M82 and NGC 3077, one would expect to observe a similar feature in M81. In fact, bifurcation is seen in the deprojected H I image (Figure 3.2) at around the corotation radius, but the gas density of the bifurcated arm at outer radius is not as high as that of the main NE arm that we have analyzed. The SW arm shows more complicated features, such as at least two bifurcations.

The existence of the bifurcation indicates the main arm by the earlier passage should be prominent by the time of the later passage. Therefore, if the bifurcation in M81 is a real product of the two separate passages, we are able to infer that the spiral structure of M81 has survived for at least ~280 Myr. Williams et al. (2009) conducted a SFH analysis for their M81-deep (~2 mag deeper than our data) field in the outer disk, and also suggested that the M81's spiral arms are at least 100 Myr old.

3.5 Summary & Conclusions

In this paper, we investigated the validity of the stationary density wave theory to explain the grand-design spiral structure in M81. We analyzed resolved stellar populations in 20 regions around the logarithmic spiral arm, and derived star formation histories of individual regions using CMD-fitting. Our approach avoids many uncertainties inherent in using discrete SF/gas tracers to measure the angular offsets across the spiral arms.

To test the assumption that the spiral structure of M81 is driven by a stationary density wave with a single pattern speed, we estimated the timescales for the disk material to cross the spiral arm as a function of galactic radius based on the relative velocity between the rotation curve and a given single pattern speed ranging from 17–25 km $\mathrm{s}^{-1}\mathrm{kpc}^{-1}$. We then compared the predicted SF propagation with the potential age gradient imprinted in our derived SFHs across the spiral arm. The resulting SFHs shows no systematic age gradient across the spiral arm at all radii. Rather the SFHs are stochastic over the timescales of interest. This result provides convincing evidence that the grand-design spiral structure of M81 is not supported by the stationary density wave with a single pattern speed, but instead is likely supported by a tidally induced kinematic waves due to the interactions with companion galaxies. In addition, we also discuss the bifurcation as additional evidence supporting the tidally induced kinematic density waves in M81, which will wind up slowly and eventually decay. In conclusion, our recent SFH results agree with other studies that have found observational evidence against the traditional density wave theory in other nearby grand-design spiral galaxies (e.g., Foyle et al. 2011; Ferreras et al. 2012; Martínez-García & González-Lópezlira 2013).

Chapter 4

CURRENT AND FUTURE WORK: RGB STELLAR OVERDENSITY IN M31

In this chapter, we briefly present preliminary results of an ongoing research on the galactic structure of M31. The underlying structure of a galaxy can be traced by old stellar populations. To trace the galactic structure of M31, we construct a red giant branch (RGB) star number density map from the Panchromatic Hubble Andromeda Treasury (PHAT) photometry. We measure two significant RGB overdensities in M31 at ∼5 and 10 kpc to the galactic center. We also find the stellar mass enhancement in the same regions. We will continue to investigate the origin of the RGB overdensities in M31.

4.1 Introduction

M31 is the nearest spiral galaxy to our Milky Way (785 kpc; McConnachie et al. 2005). However, it is hard to determine the global structure of M31 due to its high inclination ($i \simeq 78°$). M31 is known for the main10 kpc SF feature. This feature is clearly seen in SF/gas tracers (e.g., Baade & Arp 1964; Hodge 1979; Braun 1991; van den Bergh 1991; Haas et al. 1998; Loinard et al. 1999; Nieten et al. 2006; Gordon et al. 2006; Gil de Paz et al. 2007; Kirk et al. 2015). Block et al. (2006) suggested that a head-on collision with a companion galaxy, most likely M32, could produce ring structures in M31. The collision origin rings are expected to be propagating density waves. Recently, Lewis et al. (2015) showed that the SF in the 10 kpc ring has been continued for at least ∼500 Myr, and found no significant dispersion in the 10 kpc ring. This suggests that the 10 kpc ring structure is long-lived, thus not favoring the collision origin.

Another feature at 5 kpc has been reported in various studies. This 5 kpc feature is found at the end of bar along the major axis (Beaton et al. 2007). Davidge (2012) detected an overdensity of AGB stars in this feature and suggested two possible origins: (1) a relic satellite galaxy seen through the M31 disk, or (2) a fossil SF region. Dorman et al. (2015)

measured the highest velocity dispersion in this region, indicating that the 5 kpc feature is likely a dynamical origin. In addition, Gregersen et al. (2015) observed significant metal enrichment in this region.

Although observational data have been accumulated, the origin of these two prominent features are not understood well. In Dalcanton et al. (2012), we detected a sign of RGB overdensities both at 5 and 10 kpc from incomplete data set. To figure out their origin, we look at the RGB overdensity with complete PHAT data and WISE image. Throughout this work, we assume a distance modulus for M31 of 24.47 (785 kpc; McConnachie et al. 2005), where $1''$ corresponds to a physical size of 3.81 pc ($1^\circ \sim 13.7$ kpc).

4.2 Data

In this study, we use a subset of the near-IR (NIR) photometry from the PHAT survey (Dalcanton et al. 2012). PHAT is a multi-cycle program imaging about one-third of M31's star-forming disk in the near-UV (F275W, F336W), optical (F475W, F814W), and NIR (F110W, F160W) with the Advanced Camera for Surveys (ACS) Wide Field Channel (WFC) and the Wide Field Camera 3 (WFC3). Figure 4.1 shows the PHAT footprints on the WISE W1 [3.4μm] mosaic image (see Section 4.3.1 for the details). The PHAT survey region is divided into 23 "bricks". Each brick consists of 3×6 WFC3/IR pointings, with overlapping WFC3/UVIS and ACS/WFC exposures. Since the PHAT data cover a large part of M31, from the bulge to the outer disk, the dataset provides an opportunity to explore the global structure of the M31 disk using resolved stellar populations. The final PHAT photometry catalog includes ∼117 million resolved stars from the simultaneous six-filter photometry (Williams et al. 2014).

4.2.1 RGB Stars in the PHAT Survey

RGB stars are excellent tracers of morphology and evolution of a galaxy. They are abundant and intrinsically bright in the IR, where dust obscuration is minimized. They are also low mass stars ($\sim 2\ M_\odot$), making them good tracers of the total stellar mass for ages older than ∼1 Gyr. Thus, using RGB stars, we can probe the old underlying stellar distribution even

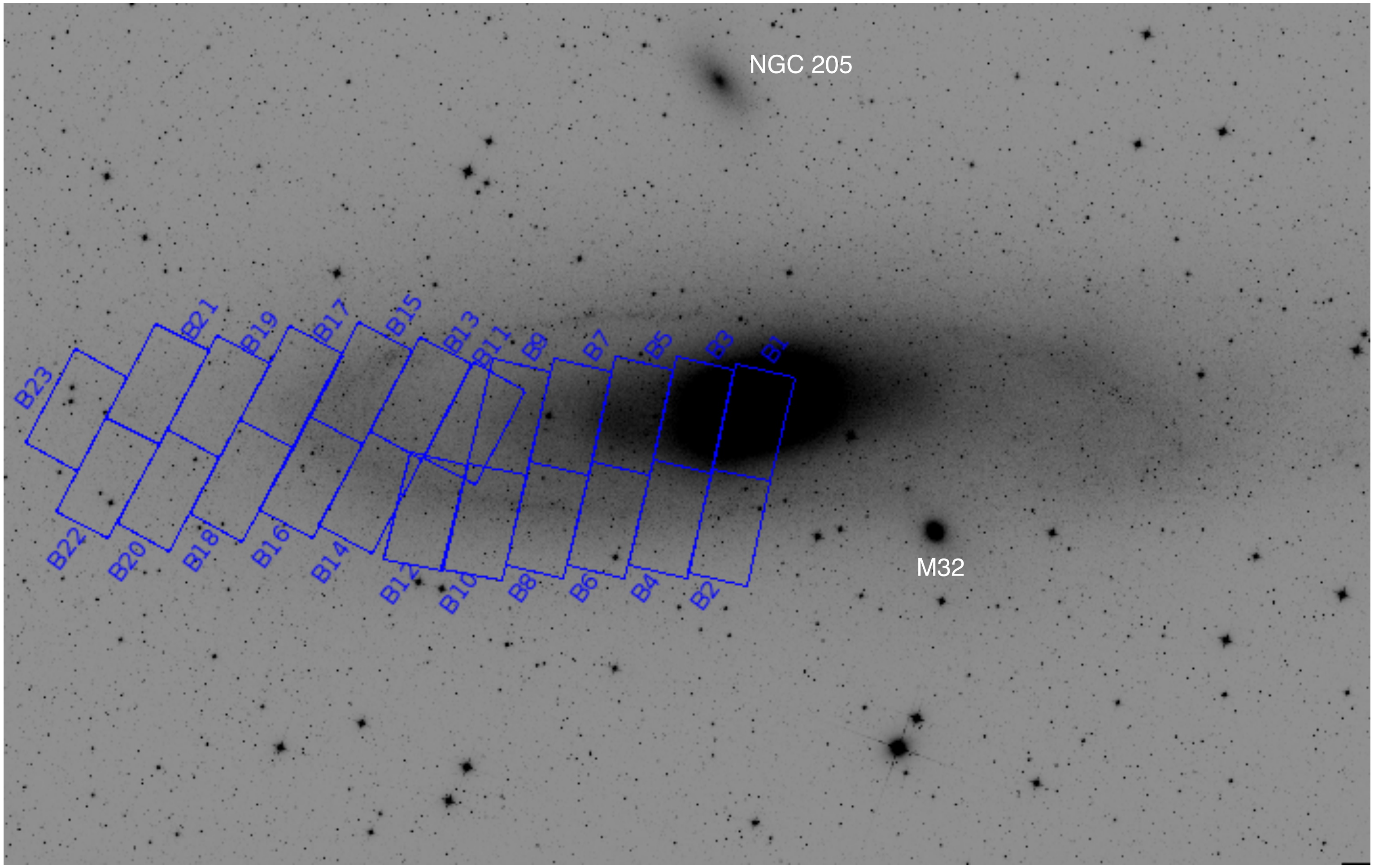

Figure 4.1 Footprint of the PHAT survey (Dalcanton et al. 2012) region (blue) displayed on a mosaic WISE W1 image of M31. The survey covers 0.5 deg^2 area.

in the regions highly obscured by the dust. To study the M31's galactic structures, we first isolate RGB stars from the PHAT photometery (Williams et al. 2014).

Figure 4.2 shows the NIR CMD for all IR-detected stars in the `gst` catalogs of the entire PHAT survey. We apply a foreground extinction correction of $E(B-V) = 0.062$ (Schlafly & Finkbeiner 2011) to the data. Following Dalcanton et al. (2012), we use NIR color and magnitude cuts to select bright, metal-rich ([Fe/H] > –0.7) RGB stars with $E(B-V) < 3$. The selection region for metal-rich RGB stars was determined based on the PADOVA isochrones (Marigo et al. 2008; Girardi et al. 2010) in Dalcanton et al. (2012). The mean metallicity of the RGB is [M/H] $\simeq$ -0.11, derived assuming a fiducial age of 4 Gyr (Gregersen et al. 2015). Selecting only bright RGB stars minimizes photometric biases due to the crowding, such that the RGB sample should be uniformly detectable across a wide range of stellar density. In the selected RGB sample, there are 1,940,197 stars. The ages of these RGB stars vary from ∼10 Gyr at the blue edge of the selection region to ∼1.5 Gyr, assuming solar metallicity.

Contaminants in the bright, metal-rich RGB star sample could lead to overestimates of the stellar number density. In the absence of dust, our RGB selection region should be almost entirely dominated by RGB stars, with some modest contribution from AGB stars. However, there are core He-burning stars and other evolving giants just blueward of our selection region, and, in the presence of dust, it is possible that some of these will be reddened into our RGB selection region.

In the bottom panel of Figure 4.2, we isolate the region of possible contaminants to the RGB selection. Stars in this region could be reddened into the RGB selection region. This contaminant region parallels the RGB selection region redward along the reddening vector out to $E(B-V) < 3$ ($A(V) \lesssim 9.3$ with $R(V)$ of 3.1); we note that the dust maps in Dalcanton et al. (2015) find essentially no regions with mean extinctions $A(V) \gtrsim 4$, making the estimate of contaminants extremely generous. This region contains any metal-poor ([Fe/H] < –0.7) RGB stars (which are rare; Gregersen et al. 2015), AGB stars, and younger populations such as unreddened red supergiants and TP-AGB stars. We select 521,074 stars from this region as possible contaminants. We use these possible contaminants when making a correction for the dust extinction effect on the RGB stellar density map in the next section.

4.3 The RGB Stellar Number Density Map

With the RGB stars selected based on their position in the CMD (Figure 4.2), we calculate the stellar number densities of these stars in $30'' \times 30''$ bins over the entire PHAT survey area. This bin size ensures a sufficient number of stars in each bin (typically X per bin), allowing us to avoid significant fluctuations due to low number statistics. At a distance of 785 kpc, $30''$ is equivalent to $\sim$114 pc along the major axis.

The RGB stellar number density map is shown in the top panel of Figure 4.4. As expected, the distribution of old populations varies smoothly, in that the stellar number density decreases along the major axis. For purposes of display, we rotate the map with a major-axis position angle of 38° (Barmby et al. 2006) around the galaxy center $(\alpha, \delta) = (10^\circ.6847929, 41^\circ.2690650)$ in J2000. The map shows some very low level residual structures on the scale of the WFC3/IR fields. This structure is due to very low level photometry offsets traced to errors in the PSF model (Dalcanton et al. 2015).

To correct for spatial variation due to reddened blue stars contaminating the RGB selection region in each pixel, we compute the number ratio of the selected RGB stars (hereafter $\mathrm{R_{obs}}$) to the possible contaminants (hereafter $\mathrm{C_{obs}}$) as a function of deprojected galactic radius (Figure 4.3). The median ratio is $\sim$0.227, and about 90% of pixels have $\mathrm{C_{obs}/R_{obs}} < 0.4$. We take the ratio of 0.4 as an intrinsic value for the no-extinction case. We then assume that when $\mathrm{C_{obs}/R_{obs}}$ is less than 0.4, some fraction of the potential contaminant stars were indeed reddened into the RGB selection region, which decreases $\mathrm{C_{obs}}$ and increases $\mathrm{R_{obs}}$. We can correct for this effect by computing $\mathrm{R_{intrinsic}}$ for pixels with $\mathrm{C_{obs}/R_{obs}} < 0.4$ as follows:

$$R_{\mathrm{intrinsic}} = R_{\mathrm{obs}} \frac{1 + C_{\mathrm{obs}}/R_{\mathrm{obs}}}{1.4}. \tag{4.1}$$

The middle panel of Figure 4.4 presents the map of $\mathrm{R_{intrinsic}/R_{obs}}$, showing the amount of the correction. Although they were calculated independently, the distribution of the pixels with low $\mathrm{R_{intrinsic}/R_{obs}}$ shows strong spatial correlations as well as excellent agreement with the map of the RGB mean color deviation from a fiducial RGB locus (see the right

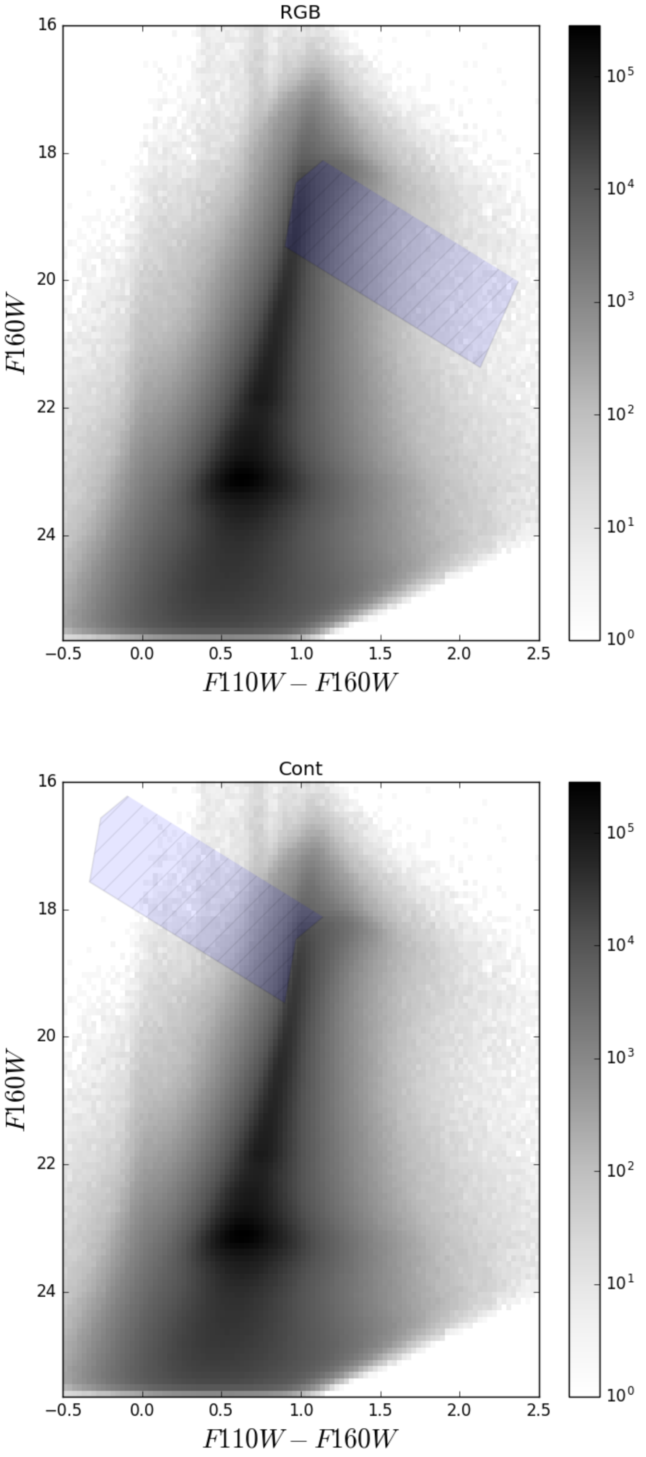

Figure 4.2 The NIR CMD for all IR-detected stars in the PHAT survey. In the top panel, we show our selection of bright, metal-rich ([Fe/H] > –0.7) RGB stars with $E(B-V) < 3$. In the bottom panel, we show possible contaminants. They are metal-poor RGB stars, red supergiants, and AGB stars. When the stars that were originally in this regions are highly reddened, they will move to our RGB selection region.

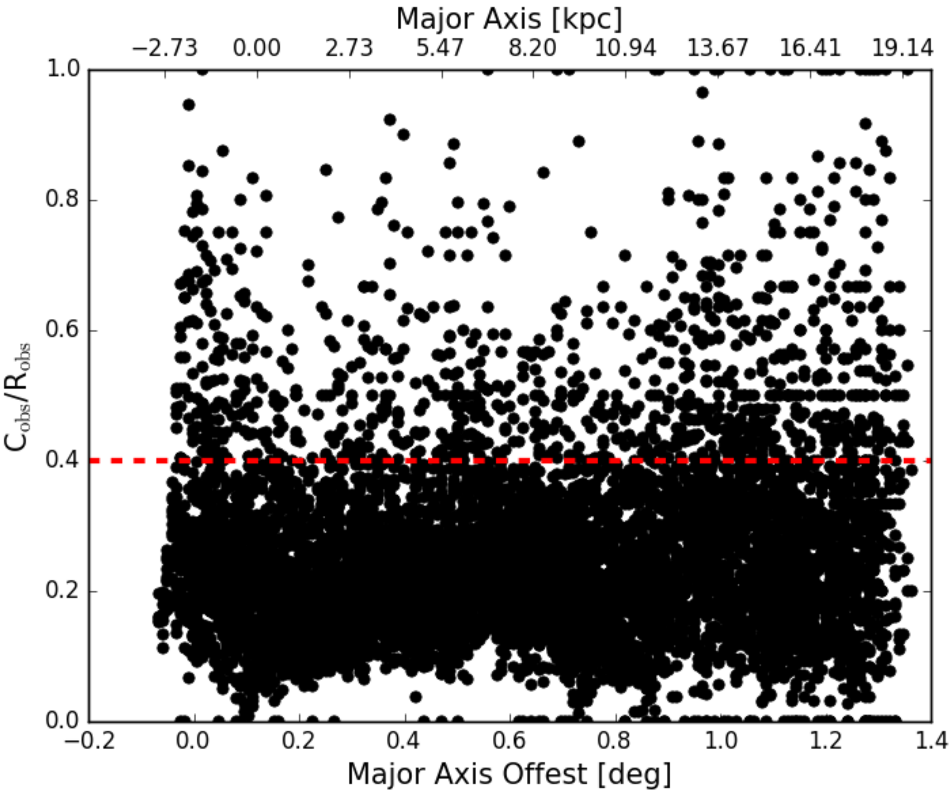

Figure 4.3 The number ratio of possible contaminants (C_{obs}) to the metal-rich RGB stars (R_{obs}) versus the Major axis offset from the galactic center. The median value of $R_{intrinsic}/R_{obs}$ is 0.227. We take the upper envelope of 0.4 as an intrinsic ratio, and assume that lower values are due to potential contaminants being reddened out of the contaminant selection region and into the RGB selection region. We use this ratio to correct for contamination in the RGB sample (Equation 4.1).

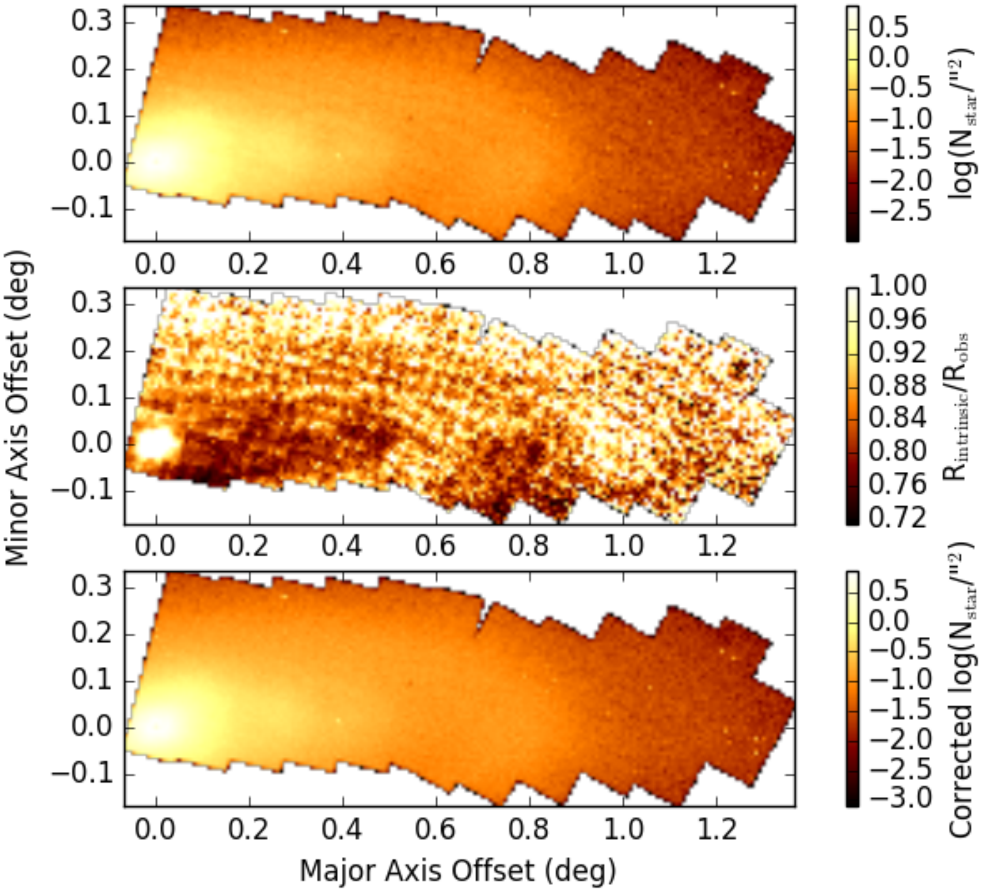

Figure 4.4 The stellar density map of the selected RGB stars (top panel) and the map of $R_{intrinsic}/R_{obs}$ (bottom panel). $R_{intrinsic}$ is the number of metal-rich RGB stars after correcting for the dust extinction effect, and is computed from the Equation 4.1. We rotated these maps assuming a position angle of 38° (Barmby et al. 2006).

panel of Figure 6 in Dalcanton et al. 2015). The regions with higher correction (i.e., lower $\mathrm{R_{intrinsic}/R_{obs}}$) correspond to the regions with larger color shifts. Since the color shifts increase both with dust extinction and higher fractions of stars behind the dust layer, the spatial agreement with our $\mathrm{R_{intrinsic}/R_{obs}}$ map suggests the correction is reasonable. Dalcanton et al. (2012) showed that this correction significantly reduced pixel-to-pixel scatter in the RGB density map in general, without affecting the RGB overdensity feature at the 10 kpc. Thus, we expect this correction would not change our interpretations based on large scale features.

In the correct RGB density map (Figure 4.4), one can see signs of two overdensities: one at ∼0.3 degree away from the center and the other at ∼0.8 degree away from the center. The former one is at near the edge of the bar, and the latter one is at the 10 kpc. In the rest of this work, we will analyze these overdensities and explore their origins.

4.3.1 WISE W1 Mosaic Image

Although the RGB stellar number density map is a direct measure of old stellar mass, the map constructed from the PHAT photometry covers only a fraction of M31, especially along the minor axis. Furthermore, the galactic center suffers from severe crowding in the PHAT images, compromising RGB selection. Thus, we also take an independent approach to constraining the overall structure of M31, including the bulge, using a Wide-field Infrared Survey Explorer (WISE; Wright et al. 2010) W1 image mosaic. The central wavelength of W1 band is 3.4 μm.

We generate a 4200 pixel × 4200 pixel unblurred coadd of the WISE W1 imaging for M31 (“unWISE”; Lang 2014) with a center of $(\alpha,\ \delta) = 10^\circ.7,\ 41^\circ.25$. It is shown in Figure 4.1. The WISE mosaic is produced from calibrated individual WISE exposures using the unWISE coaddition code, using the background-matching option. The publicly released unWISE coadds use a background-estimation method that is run independently on each input frame, but this results in over-estimated backgrounds near large structures such as M31. With the background-matching option, the code matches the median brightness of each exposure to the accumulated coadd, so the background estimate is continuous and does not overshoot around bright objects. When the coadd is complete a single background level is estimated and removed.

The WISE pixelscale is 2.75 arcsec/pixel, and thus the coadd covers an area of 3.2° × 3.2° on the sky. This mosaic is the largest areal coverage of M31 in the mid-IR presented to date. It includes the two satellite galaxies (M32 and NGC 205), and extends well beyond the faint outskirts of M31.

Before modeling the galactic structures of M31 using the W1 mosaic, we construct a mask of all foreground stars and the two satellite galaxies. We use SExtractor (Bertin & Arnouts 1996) to identify sources, and, for bright foreground stars and NGC 205, we enlarge their initial mask sizes by a factor of 5/3 to ensure low surface halos are adequately masked.

Decomposing a 4200 × 4200 pixel galaxy image into its different structural components is computationally expensive. To make the decomposition efficient, we resample the original WISE W1 image, by summing fluxes in individual pixels. We combine 8 × 8 pixels, including mask information by taking the mean flux only from unmasked pixels. Then we assign a value of the mean flux multiplied by 64 to a new combined pixel. If the fraction of masked pixels in a new combined pixel is greater than 60%, then we exclude that combined pixel from the fitting process.

The pixelscale of the resampled map is $22''$ (∼83.6 pc), which is less than one tenth of the bulge half-light radius (e.g., Courteau et al. 2011; Tempel et al. 2011; Dorman et al. 2013). The spatial resolution of this resampled map is comparable to, but ∼30% better than, that of the constructed RGB map. Thus, resampling still provides sufficient spatial resolution to model the inner part of the galaxy properly, while having a factor of 64 fewer samples.

The resulting resampled W1 map is presented in Figure 4.5. We also make an empirical standard deviation map to use as uncertainties (σ) in the fitting process. For each pixel, we estimate the standard deviation σ from the neighboring 10 × 10 pixels. The empirical σ map is shown in Figure 4.6. These maps are in units of Vega "nanomaggies"; a flux unit with a zeropoint of 22.5 Vega magnitude.

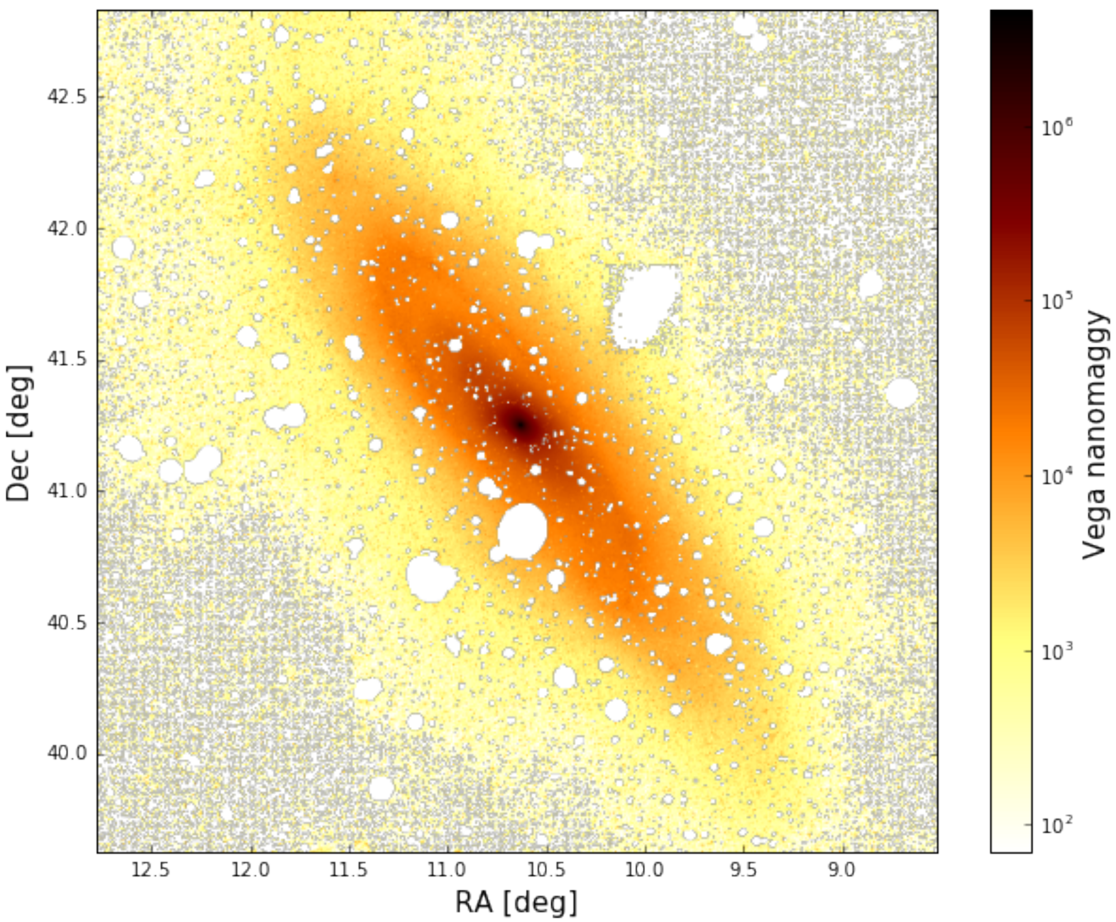

Figure 4.5 Resampled WISE W1 map by combining 8 × 8 pixels in the original mosaic. A new pixelscale is 22 arcsec/pixel, corresponding to ~83.6 pc at the distance of M31. White pixels are the ones maksed that we exclude from the fitting process.

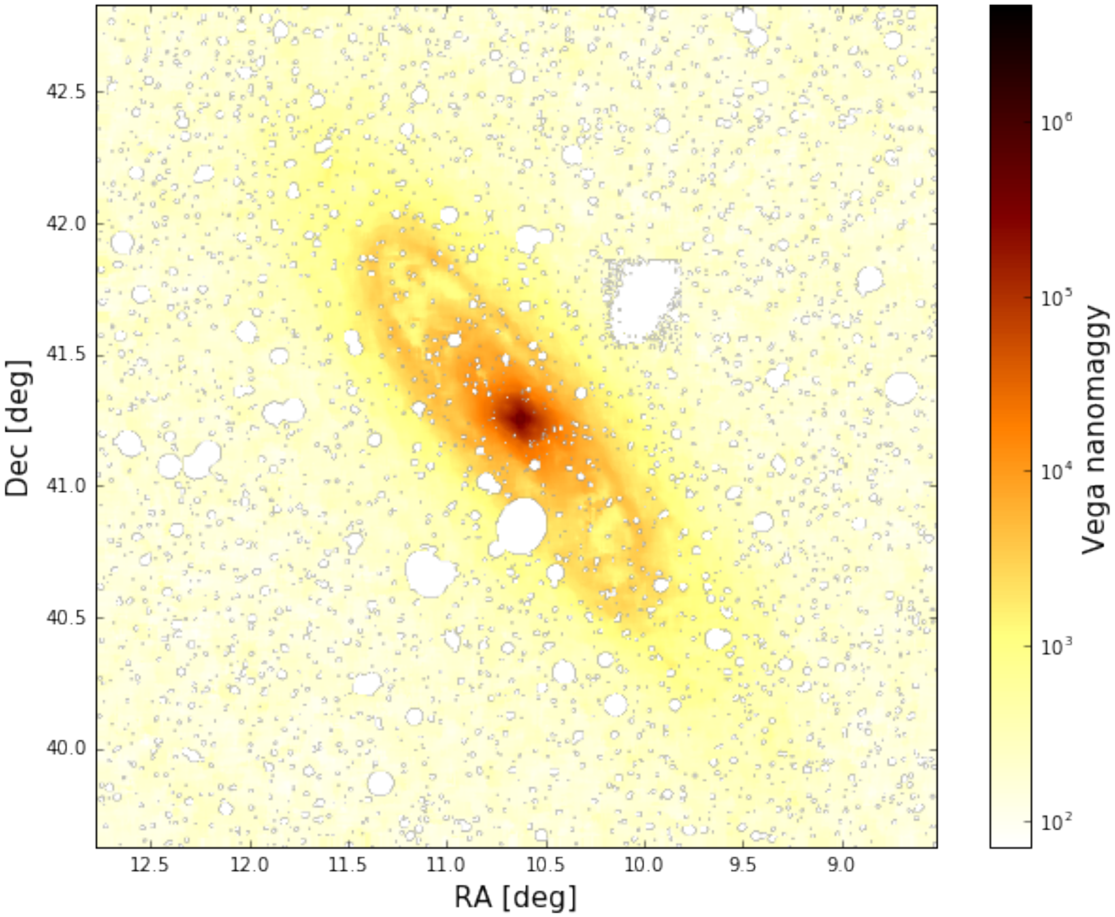

Figure 4.6 Resampled W1 sigma map.

4.4 Analysis

In this section, we present the results for the two-component modeling of the WISE W1 image and the three-component modeling of the RGB stellar number density map. Most parts of analysis are completed, thus we are able to constrain the underlying galactic structure and identify overdensities in M31. However, we will include extra components (e.g., classical bulge, halo, etc.) in our 2-D modeling to potentially improve our ability to model complex inner structures and quantify overdensity structures more accurately in the future.

As we mentioned above (Section 4.1), M31's appearance suggests the existence of multiple interesting structural components. In particular, there is a prominent feature at ∼10 kpc where recent SF is enhanced (e.g., Habing et al. 1984; Gordon et al. 2006; Lewis et al. 2015), and appears to have been elevated for multiple dynamical times ($>$ 500 Myr; Lewis et al. 2015). In addition, there is a round-shaped feature at ∼5 kpc, near the end of the galactic bar (e.g., Davidge 2012; Dorman et al. 2015; Gregersen et al. 2015). The origin of these features is not clear. In this section, we first focus on characterizing these 10 kpc and 5 kpc structures.

4.4.1 Decomposing M31's Galactic Structures Using WISE W1 Map

To better characterize the stellar overdensities at ∼10 kpc and ∼5 kpc, we first need to model the underlying galactic structure. We start by fitting the WISE W1 image (Figure 4.5) with a multi-component galaxy model. For comparison, Figure 4.7 shows the areal coverage of the RGB map superposed on the resampled WISE image.

We start with a simple two-component parameterization consisting of a Sérsic (1968) bulge and an exponential disk, and then we add an additional bar component. Then we attempt a more complex model that includes a classical bulge and a bar.

4.4.1.1 Galaxy Model Components

For the bulge, we adopt a Sérsic (1968) profile,

$$I(r) = I_e \exp\left\{-b_n\left[\left(\frac{r}{r_e}\right)^{1/n} - 1\right]\right\}, \tag{4.2}$$

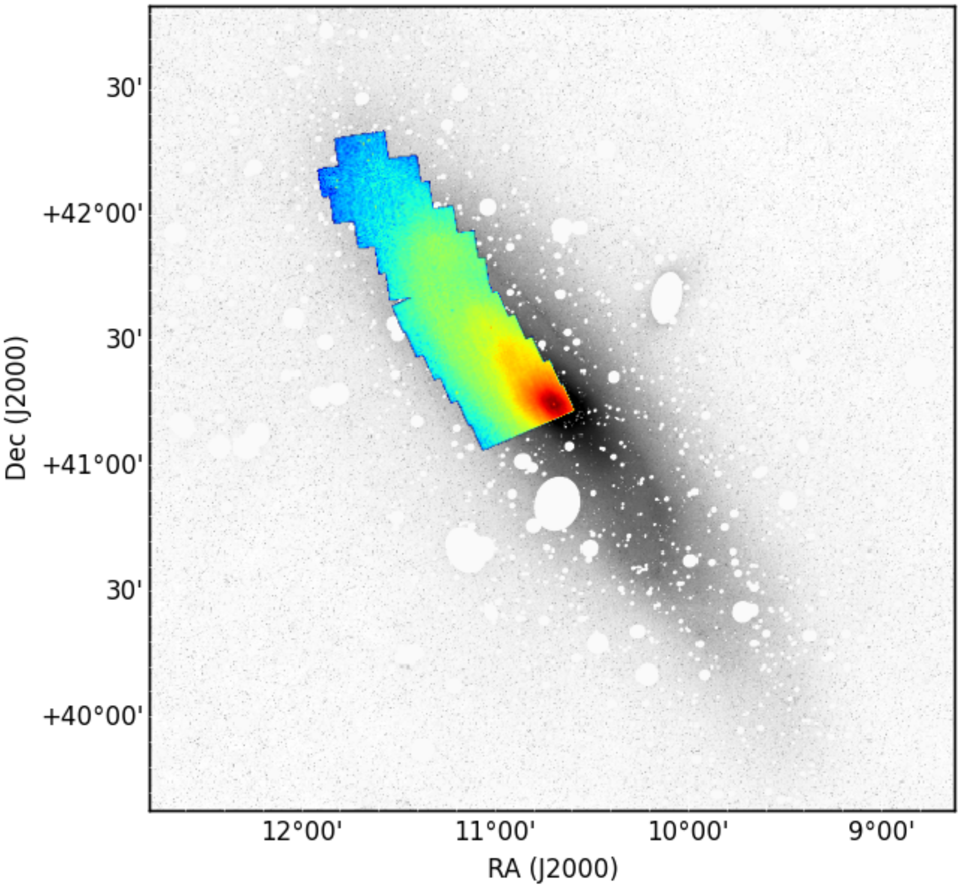

Figure 4.7 The RGB stellar number density map on top of the WISE W1 image.

where r_e is the bulge half-light radius, I_e is the bulge intensity at r_e, n is the Sérsic index, and $b_n = 1.9992n - 0.3271$ (valid for $0.5 < n < 10$; Capaccioli 1989). The shape of this profile is mainly determined by the Sérsic index n. With $n = 4$, the Sérsic profile is equivalent to the de Vaucouleurs profile.

To account for the boxyness/diskyness, we apply a generalized ellipse as the r term in in the Sérsic profile,

$$r(x, y) = \left(|x - x_0|^{C_0+2} + \left| \frac{y - y_0}{b/a} \right|^{C_0+2} \right)^{\frac{1}{C_0+2}}, \tag{4.3}$$

where (x_0, y_0) is the center of the bulge, and a and b are the semimajor and semiminor axes of the bulge. When $C_0 = 0$, the shape of the isophotes is purely elliptical. When $C_0 > 0$, the shape becomes boxy, whereas the shape becomes disky when $C_0 < 0$. The b/a ratio determines the inclination, $i = cos^{-1}(b/a)$, and the ellipticity, $\epsilon = 1 - (b/a)$.

For the disk, we adopt a single exponential profile,

$$I(r) = I_{0,d} \exp\left(-\frac{r}{r_d} \right), \tag{4.4}$$

where $I_{0,d}$ is the disk central intensity and r_d is the disk scale length. We do not consider double exponential profiles for the M31 disk, because there is no noticeable disk break in our RGB map.

Finally, we adopt the modified Ferrers profile (e.g., Laurikainen et al. 2007; Peng et al. 2010) for a bar,

$$I(r) = I_{0,b} \left[1 - \left(\frac{r}{r_{out}} \right)^{2-\beta} \right]^{\alpha}, \tag{4.5}$$

where $I_{0,b}$ is the bar central intensity, r_{out} indicates the end of the bar profile, α determines the sharpness of the truncation at r_{out}, and β determines the inner slope of the profile.

4.4.1.2 Model Fitting with Bayesian Technique using MCMC sampling

We also decompose the M31's image using a Bayesian technique with the Markov chain Monte Carlo (MCMC) sampler `emcee` (Foreman-Mackey et al. 2013). With the Bayesian approach, we can extract the probability distribution functions (PDFs) of each of the model parameters, as well as the correlations among parameters.

We can also incorporate prior knowledge about the model parameters. We assign equal likelihoods on values within the physically meaningful ranges. When parameters deviate from these ranges, we set zero probability for the priors. The ranges for each parameter are presented in the 3rd column of Table 4.1.

To achieve the computational efficiency and accuracy, we compute the log probability:

$$lnP(\theta \,|\, F_D) \propto lnP(F_D \,|\, \theta) \ + lnP(\theta). \tag{4.6}$$

We use the Gaussian likelihood with an extra uncertainty term σ_{jitter},

$$lnP(F_D \,|\, \theta) = -0.5 \sum_{i}^{nx} \sum_{j}^{ny} \left[ln(2\pi \, (\sigma^2(i,j) + \sigma^2_{jitter})) + \frac{(F_D(i,j) - \theta \, (i,j))^2}{\sigma^2(i,j) + \sigma^2_{jitter}} \right]. \tag{4.7}$$

The σ_{jitter} term is a nuisance parameter that accounts for underestimated uncertainties or imperfections in the models. In cases when it is unnecessary, the nuisance parameter naturally goes to zero. We include the nuisance parameter in the MCMC analysis. The total number of parameters included in the two-component modeling is 11 (10 structural parameters + 1 nuisance parameter). For the three-component modeling, there are 6 additional structural parameters associated with the bar component.

Instead of starting the walkers randomly sampled from flat priors, we run MCMC for 1,000–2,000 steps several times to find a good initial guess for parameters. Restarting the walkers around the maximum $lnP(\theta \,|\, F_D)$ position of the last step in the previous run is efficient for finding a reasonable initial guess. This technique also prevents the walkers from being stuck at a local maximum.

Once we set a reasonable initial point in the parameter space, we start 50 independent walkers in a small N-dimensional ball around this initial guess point. In this study, N is 11 for the two component modeling, and 17 for the three component modeling. At earlier steps in the chain, the walkers do not represent the true posterior PDFs. Once we run MCMC long enough (∼10 autocorrelation times; Foreman-Mackey et al. 2013), the ensemble of the walkers approximates the true posterior PDFs and thus we can estimate the parameters after discarding the first n steps in the chain (i.e., "burn-in"). We determine conservatively the length of the burn-in phase based on the $ln(F_D \,|\, \theta)$ over steps in the chain to assure the minimal effect of initial values.

4.4.1.3 Results for the Two-Component Model

We first model the WISE WI image with an exponential disk and a Sérsic bulge. Figure 4.8 presents the results from the MCMC method. Our final run has 3,000 steps in the chain and the first 1,000 steps are discarded, although it reaches to the equilibrium distribution after the first ∼500 steps. Figure 4.8 shows posterior PDFs for each parameter along the diagonal, and visualizes the covariances between parameters from the last 2,000 steps. The 50th percentile value with 1σ confidence interval for each parameter is presented in Table 4.1. We estimate 1σ confidence intervals from the marginalized 1D posterior PDFs for each parameter, by identifying the values containing 16% and 84% of the probability.

All of the disk parameters agree well with values measured from previous studies using NIR images of M31 (e.g., Seigar et al. 2008). For example, the disk position angle of $38^\circ.198$ is consistent with the previous measurements (e.g. Walterbos & Kennicutt 1987; Ferguson et al. 2002; Barmby et al. 2006). This position angle has been accepted as a standard global position angle of M31. The position angle of our bulge is $\sim 20^\circ$ greater than that of the disk, which is consistent with the previous works (e.g., Athanassoula & Beaton 2006; Beaton et al. 2007). Contrary to the boxy appearance, the bulge has a negative C_0 value, i.e., disky. The disky bulge results from modeling a complex inner part with basically only one component; contribution of the disk component in the inner part is marginal. The bulge's axis ratio of ∼0.5 also can be interpreted as the contribution from an elongated bar component. We expect the true axis ratio of the bulge is larger than 0.5.

We compare our results with those (model G) reported in Courteau et al. (2011). Among their models, the model G is the most appropriate for comparison because of the similarity in bandpass and fitting method. Specifically, in their model G, they decomposed the azimuthally averaged 1D IRAC 3.6μm surface brightness profile into an exponential disk and a Sérsic bulge. Although they did not fit for the position angles for each component (and instead assumed a single position angle and inclination for different components), we find good agreement with most of our resulting parameters including disk central surface brightness $\mu_{0,d}$, disk scale length r_d, bulge effective surface brightness μ_e, and bulge effective radius r_e. However, we measure a slightly flatter (∼0.1 dex smaller Sérsic index) bulge

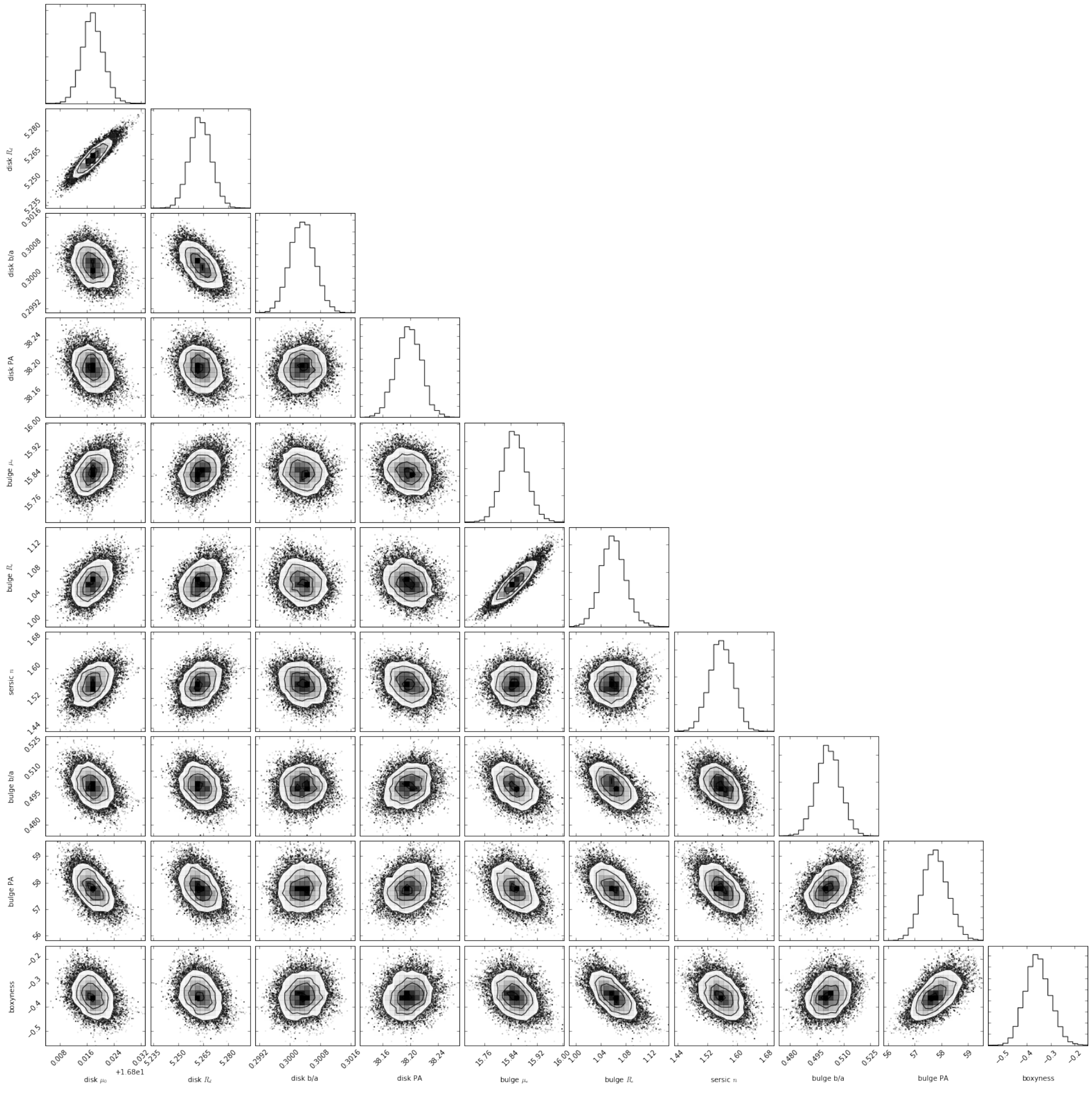

Figure 4.8 The results of the two-component modeling of the WISE W1 image using the MCMC method. We present the posterior PDFs for individual parameters and covariances between them.

Table 4.1. Parameters for the two-component modeling of the WISE W1 image using the MCMC method

Parameter	Description	Range for Flat Prior	Results
$\mu_{0,d}$ [mag/$''^2$]	disk central SB	0–∞	$16.817^{+0.003}_{-0.003}$
r_d [kpc]	disk scale length	0–∞	$5.263^{+0.006}_{-0.006}$
$(b/a)_{disk}$	disk axis raio	0–1	$0.3003^{+0.0003}_{-0.0003}$
PA$_{disk}[deg]$	disk position angle	0–90	$38.198^{+0.0183}_{-0.0179}$
μ_e [mag/$''^2$]	bulge effective SB	0–∞	$15.851^{+0.035}_{-0.037}$
r_e [kpc]	bulge half-light radius	0–∞	$1.059^{+0.019}_{-0.018}$
n	Sérsic index	0.5–10	$1.557^{+0.031}_{-0.031}$
$(b/a)_{bulge}$	bulge axis ratio	0–1	$0.501^{+0.006}_{-0.006}$
PA$_{bulge}$ [deg]	bulge position angle	0–90	$57.762^{+0.448}_{-0.496}$
C_0	bulge shape parameter	-2–3	$-0.355^{+0.055}_{-0.050}$

than Courteau et al. (2011). This difference likely results from our allowing misalignment between the disk and the bulge rather than assuming a constant position angle for both components, we better trace the bulge profile that decreases slowly with projected radii along its own semi-major axis.

We quantify the correlations between parameters by computing the Spearman's correlation coefficient, ρ, which varies from -1 to 1. The strongest correlations are found between the length and the brightness both for the disk and the bulge components. For the disk, $\rho(r_d,\mu_{0,d}) = 0.888$. For the bulge, $\rho(r_e,\mu_e) = 0.865$. This positive coefficient implies that the size and surface brightness correlates inversely, since the surface brightness was fit in magnitude units, which increase with lower surface brightness. Thus, the surface brightness increases when the size of a component decrease to incorporate about the same amount of total flux, which minimizes the difference between the model and the data. Pairs with signif-

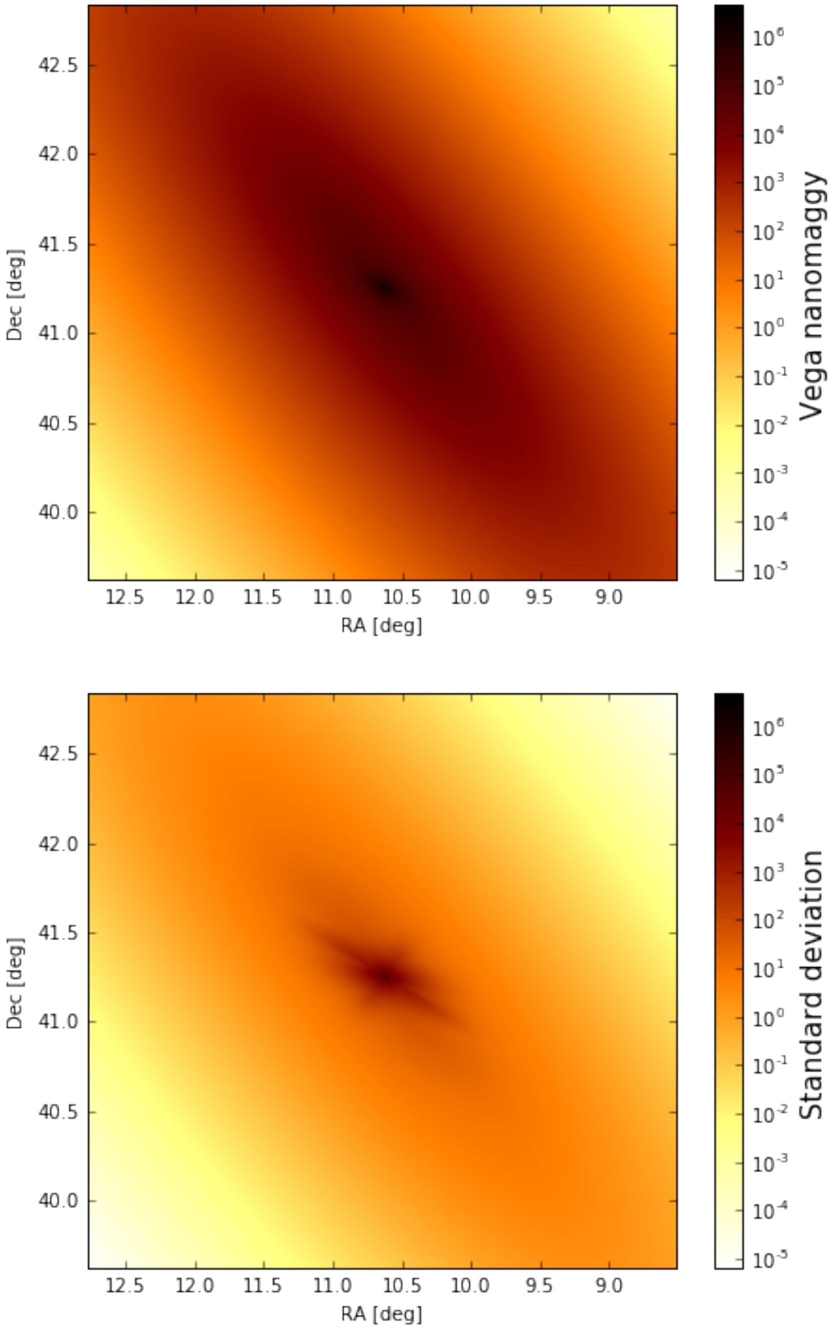

Figure 4.9 From the 500 randomly selected models out of 100,000 acceptable fits, we construct the median model galaxy (top) and the standard deviation map (bottom).

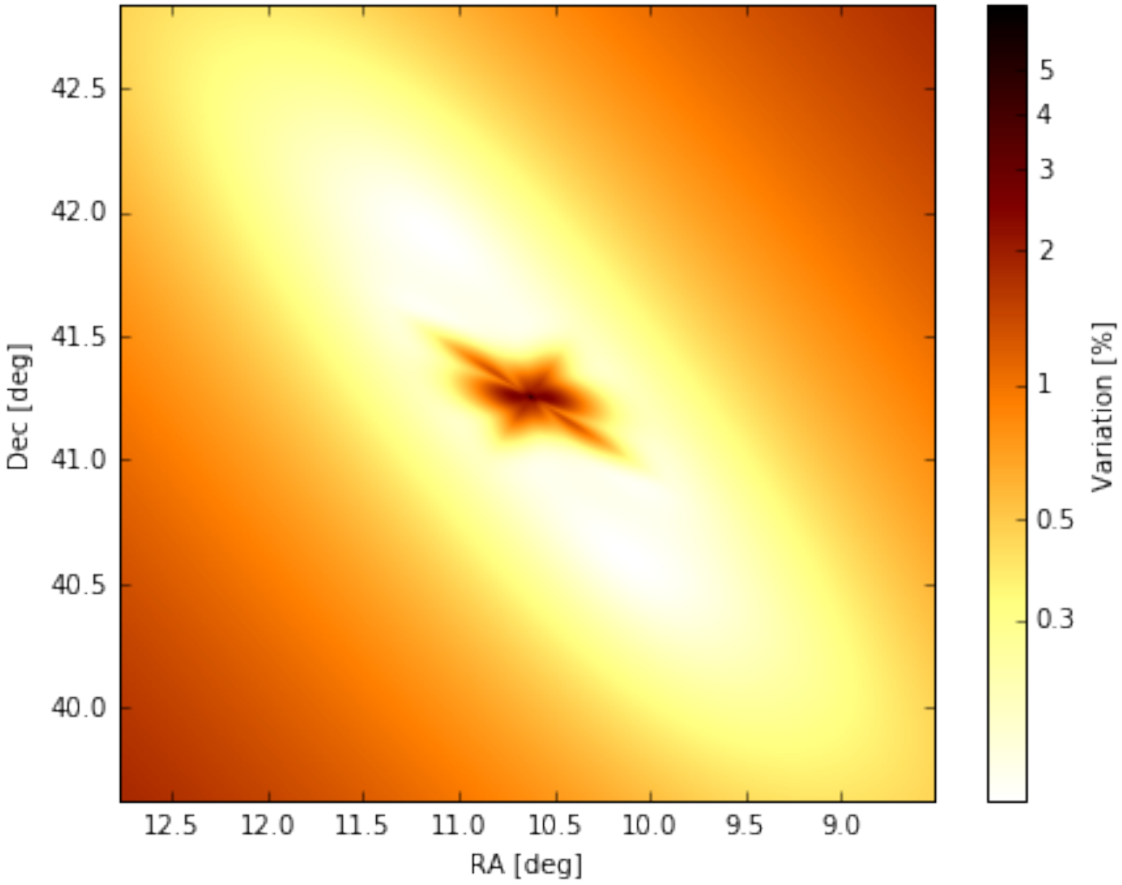

Figure 4.10 Fractional variation map. It shows the ratio map of the standard deviation map to the median model galaxy.

icant ($|\rho| > 0.5$) correlations are ($\mu_{0,d}, PA_{disk}$), ($r_d, (b/a)_{disk}$), ($r_e, (b/a)_{bulge}$), (r_e, PA_{bulge}), (r_e, C_0), and (PA_{bulge}, C_0).

We produce a median model map from 500 randomly selected models out of 100,000 (= 2,000 steps × 50 walkers) accepted fits. This random selection naturally results in the probability-weighted median model galaxy. We also compute the standard deviation of the selected 500 models to see which parts of the galaxy vary the most depending on the parameters.

In Figure 4.9, we present the median model galaxy and the standard deviation map. As expected, the bulge component dominates the central region while the disk component dominates in the outer disk region. In the standard deviation map, it is clearly seen that the central part of the galaxy is sensitive to variations in the model parameters. This is not only because the most light is concentrated at the center, but also the galaxy center is the most complex region. On the other hand, the outer disk is quite stable against variations in the parameters, indicating that the disk parameters are well constrained. Although the central region shows large variation, it corresponds to only ∼1–3% fractional uncertainty (see Figure 4.10). Overall the fractional uncertainty level across the entire image is ∼0.5–0.6%.

In Figure 4.11, we present the fractional difference between the data and the model. We subtract the median model galaxy from the data and divide by the median model. A value of 1 (–1) indicates a factor of 2 overdensity (underprediction). Red (blue) color indicates the model's over(under)-prediction. While most parts of the main disk show a mean fractional difference of ∼0, the model is under-predicted around 10 kpc, as well as a weak sign at 5 kpc that has a round shape (marked with a red circle in Figure 4.11). This feature is very similar to that reported by Davidge (2012). We found no clear evidence for a 15 kpc ring in the residual map. However, there are two small overdensity regions at 15 kpc along the major axis in the residual map.

There are notable $m = 2$ mode residuals in the central region. These are likely to be due to the inability of a single bulge component, which was not boxy, to fully capture the complex inner structure of M31 (Beaton et al. 2007). The ∼30% under-prediction in the central region strongly suggests an additional component(s) would help to better

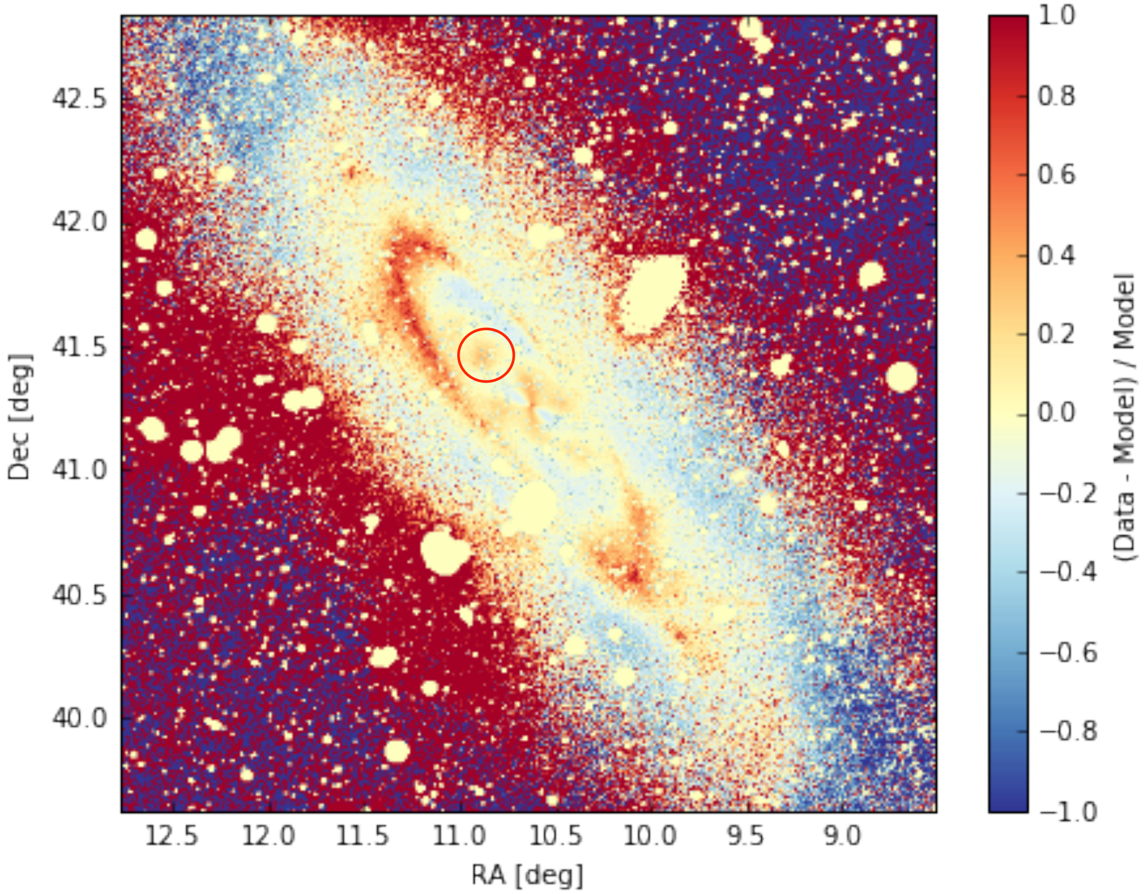

Figure 4.11 Residual map showing the fractional deviation of the median two-component model from the WISE W1 image. The most significant ring-like overdensity is at 10 kpc. We mark the notable overdensity at 5 kpc as a red circle.

characterize the features.

4.4.1.4 Deprojecting the Residual Map from the Two-Component Model

It is ambiguous whether the residual at 10 kpc is a ring or spiral arms based on its appearance, because the feature is neither complete or axisymmetric. To investigate the morphology of the observed overdensity around 10 kpc, we first select pixels inside the disk, and deproject them assuming the best-fit inclination of $72^\circ.52$ and position angle of $38^\circ.19$. In Figure 4.12, the selected pixels are plotted both in cartesian (top) and polar (bottom) coordinates. In the top panel, we denote the 10 kpc and 15 kpc radii from the galactic center. The angle is 0 at the third quadrant, and increases counterclockwise.

If the 10 kpc overdensity were a logarithmic spiral arm, then it should appear as a straight line with a nonzero slope in polar coordinates (phase vs. $\ln(R)$). In the bottom panel of Figure 4.12, for comparison, we show the best-fit spiral arm (dashed red line) with a pitch angle of $9^\circ.1$, adopted from Kirk et al. (2015). Gordon et al. (2006) and Kirk et al. (2015) both reported the spiral arm's pitch angle of $\sim 9^\circ$ when assuming a inclination of 75°, which is the median value of the inclinations reported in Braun (1991). Even if we take into account a small difference between our best-fit inclination and their assumed inclination, the WISE W1 overdensities do not follow the logarithmic spiral arm identified by Gordon et al. (2006) and Kirk et al. (2015).

An alternative possibility is that the 10 kpc overdensity is associated with a ring, not a spiral arm. If the residual feature were a ring centered at the center of M31, then it should appear as a horizontal line in the polar coordinate plot. If such a ring were off-centered, it would appear as a sinusoid. Gordon et al. (2006) examined M31's morphology using the Spitzer MIPS images at 24, 70, and 160 μm, and found a circular 10 kpc ring that is offset from the galaxy center. They showed a circular ring with this offset is well-fit by a wavy line in polar coordinates. Kirk et al. (2015) explored the spatial distribution of molecular clouds in M31 using the HELGA data set (Fritz et al. 2012), and they also found the 10 kpc ring as a wave line in the phase diagram.

Unfortunately, even with this new analysis, it is unclear whether the WISE W1 overdensity follows a ring or not. The southern feature in the top panel of Figure 4.12 might be considered as a short segment of a spiral arm. If so, then the pitch angle should be ∼27°, but this large a pitch angle has never been reported before in M31. The northern feature is more complex, and maybe a combination of a spiral arm and a ring. On the deprojected cartesian coordinate, the feature is spread out between 10 to 15 kpc in the radial direction. We note that our residual features coincide exactly with the regions where the rings and spiral arms cross each other (see Figure 16 in Kirk et al. 2015). Our two-component modeling might support the existence of both rings and spiral arms in M31.

4.4.2 Modeling the RGB Map with an Additional Bar Component

The co-existence of a bar and a bulge is common in normal disk galaxies. M31 is also known to have an elongated bar (e.g. Athanassoula & Beaton 2006; Beaton et al. 2007). Specifically, Beaton et al. (2007) suggested a narrow bar that emerges from both sides of the boxy bulge and extends outward to 4–5 kpc. We now model the RGB number density (ND) map with the three-component galaxy (an exponential disk, a bulge, and a bar).

In the previous section, we roughly constrained the global structure of M31 with a simple two-component model of the WISE data. Adopting some of the resulting parameters helps to remedy limitations of the RGB map constructed from the PHAT photometry, namely incomplete areal coverage and crowding in the galactic central region. In particular, we fix the position angles of the disk and the bulge from the WISE W1 two-component modeling.

We choose to fix the disk position angle and the disk b/a ratio, which are more reliably estimated from images of the entire disk, like the WISE image. The disk position angle and the b/a ratio were well-constrained in the WISE fitting, showing the least dependence on any other structural parameters in Figure 4.8. We fix these 2 parameters, and fit the RGB stellar number density map for the rest of the disk and bulge structural parameters, adding an additional bar component.

We further narrow the prior distributions for some parameters using results from the WISE fitting. For example, the allowed range for the bulge half-light radius r_e is between 0 and the disk scale length r_d, while there was no maximum limit in the two-component

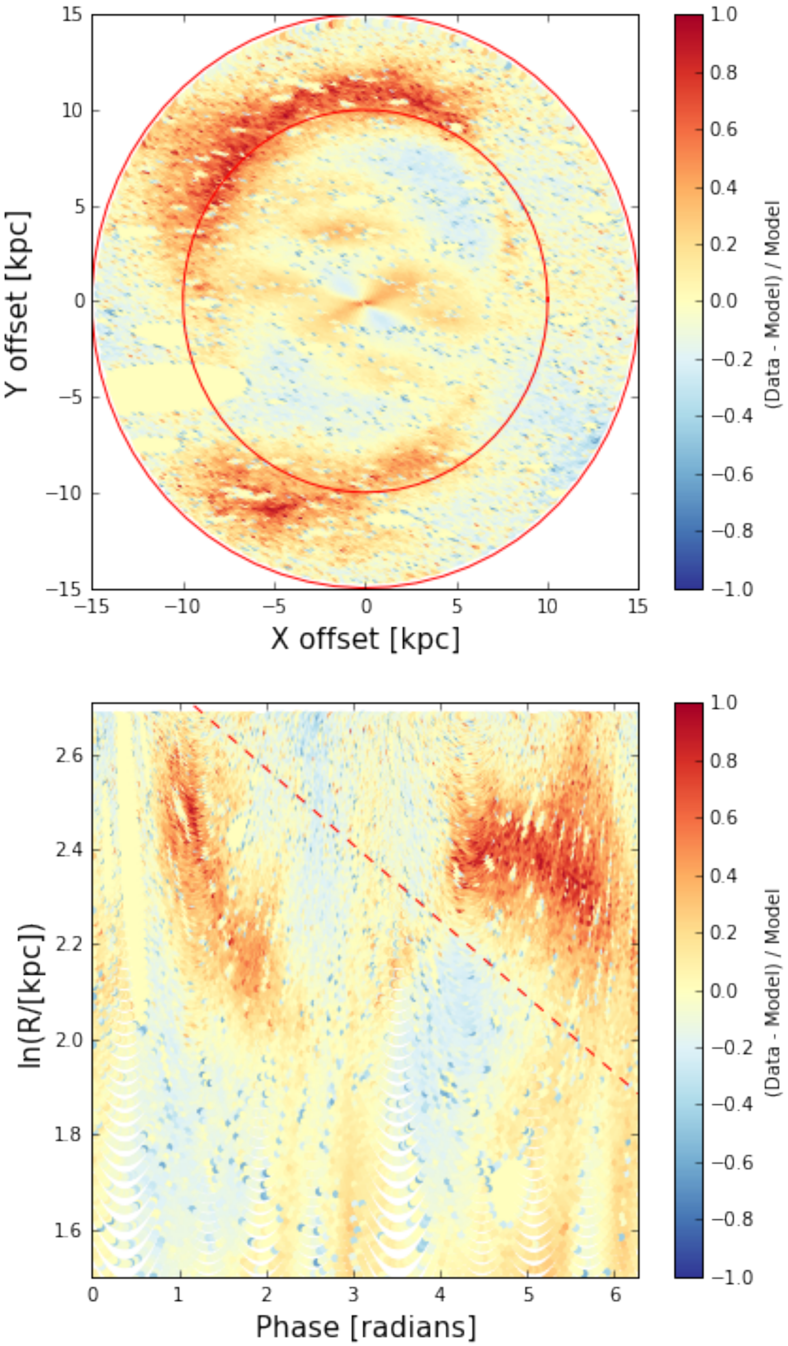

Figure 4.12 Deprojected residuals within the disk and their phase diagram (radius, azimuthal angle). In the top panel, the solid red lines denote 10 and 15 kpc radii, respectively. In the bottom panel, the dashed solid line shows the best-fit spiral arm with a pitch angle of 9°.1 (Kirk et al. 2015).

WISE fitting. Athanassoula & Beaton (2006) provided evidence for a longer bar than a boxy bulge. We thus limit the allowed prior range for the bar length r_{out} to be longer than r_e, but still shorter than r_d. We also specify the allowed range for the bar's position angle to be between PA_{disk} and PA_{bulge}. The total of 17 model parameters, including the jitter term, and their allowed ranges are listed in Table 4.2. All of the parameters' 50th percentile values and 1σ uncertainties are presented in Table 4.2.

The median model RGB map and the standard deviation map from the three-component modeling are shown in Figure 4.13. The basic trend is similar to that found in the two-component WISE model, in that the variation is large at the central region, but the fractional uncertainty remains $< 6\%$ across the majority of the inner disk (see Figure 4.14). However, compared to the WISE two-component model, the variations among acceptable models is larger, especially at the outer disk (up to $\sim$13%) along the major axis and near the end of the bar component (up to $\sim$6%). This likely results from our choice to fix the disk position angle and axis ratio.

These larger variations can be explained by the strong correlation between the disk and bar parameters. The correlations between the bar size and the two free disk parameters, disk central ND and disk scale length, are very strong. This trend is easy to understand, in that both the bar and disk components compete for stellar number density in the inner disk of the galaxy. The Spearman's correlation coefficients for these two pairs are $\rho(\rho_{0,d}, r_{out}) =$ -0.853 and $\rho(r_d, r_{out}) = 0.8676$, respectively. This strong correlation causes a large fractional uncertainty in the outer disk see in Figure 4.14. When the bar extends further outward, then the disk's contribution needs to decrease and this lower number density disk can extend even further. It also can lead a large fractional uncertainty near the end of bar. The enhanced fractional uncertainty in the inner disk marks the boundary where the bar ends and the disk component become dominant.

It is worth noting that the bulge is boxy in the three-component model, while the two-component WISE model finds a disky bulge. The discrepancy is expected, because in the current model the bulge no longer tries to fit the fluxes likely associated with a narrow bar. This is clearly seen in Figure 4.15, showing the fractional contribution of each component to the final model galaxy. The galactic central region consists of a boxy bulge, whereas the

Table 4.2. Parameters for the Three-component modeling using the MCMC method

Parameter	Description	Range for Flat Prior	Results
$\rho_{0,d}$ [N/$''^2$]	disk central ND	0–∞	$0.78^{+0.109}_{-0.101}$
r_d [kpc]	disk scale length	0–∞	$5.558^{+0.493}_{-0.413}$
$(b/a)_{disk}$	disk axis raio	fixed	$0.3003^{+0.000}_{-0.000}$
PA$_{disk}$ [deg]	disk position angle	fixed	$38.198^{+0.000}_{-0.000}$
ρ_e [N/$''^2$]	bulge effective ND	0–∞	$2.806^{+0.089}_{-0.100}$
r_e [kpc]	bulge half-light radius	$0 < r_e < r_d$	$0.594^{+0.016}_{-0.016}$
n	Sérsic index	0.5–10	$0.504^{+0.008}_{-0.003}$
$(b/a)_{bulge}$	bulge axis ratio	0–1	$0.742^{+0.016}_{-0.015}$
PA$_{bulge}$ [deg]	bulge position angle	PA$_{disk}$ $<$ PA$_{bulge}$ $<$ 90	$57.129^{+1.346}_{-1.306}$
C_0	bulge shape parameter	-2–3	$0.165^{+0.137}_{-0.109}$
$(b/a)_{bar}$	bar axis ratio	0–1	$0.414^{+0.027}_{-0.023}$
$\rho_{0,b}$ [N/$''^2$]	bar central ND	0–∞	$1.281^{+0.241}_{-0.242}$
r_{out} [kpc]	bar length	$r_e < r_{out} < r_d$	$5.309^{+0.508}_{-0.432}$
α	profile sharpness at	0–10.5	$2.714^{+0.679}_{-0.632}$
β	inner profile slope	0–2	$0.542^{+0.351}_{-0.347}$
PA$_{bar}$ [deg]	bar position angle	PA$_{disk}$ $<$ PA$_{bar}$ $<$ PA$_{disk}$	$50.826^{+1.491}_{-1.422}$

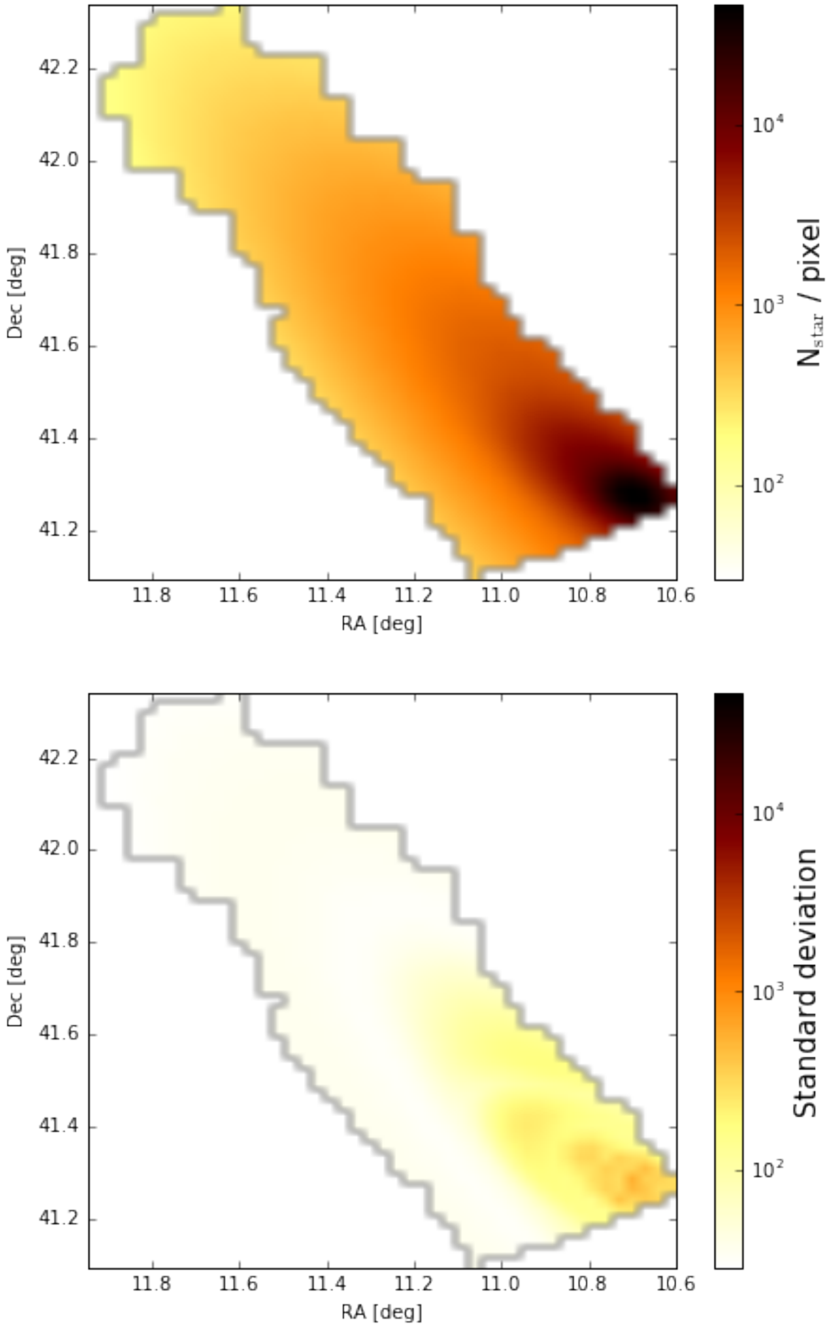

Figure 4.13 From the 500 randomly selected models out of 100,000 acceptable fits, we construct the median model galaxy (top) and the standard deviation map (bottom).

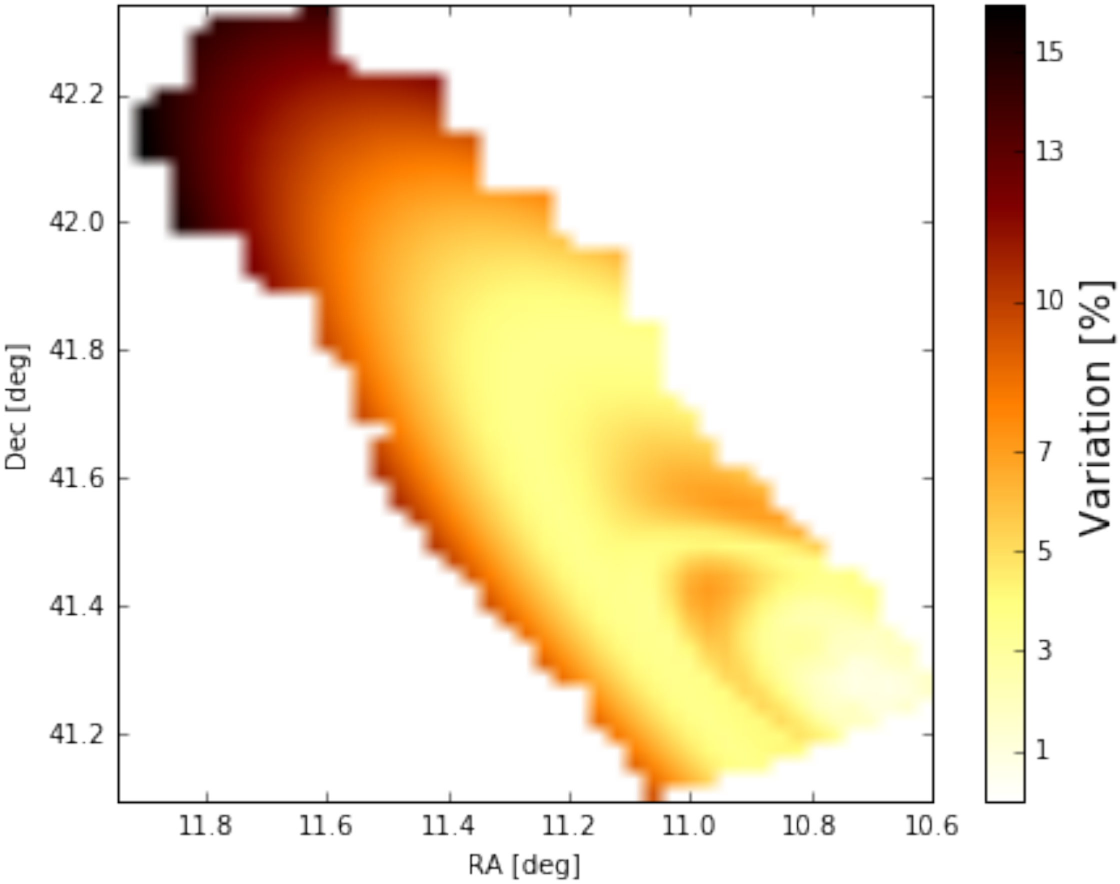

Figure 4.14 Fractional uncertainty map. It shows the percentage variation of acceptable model galaxies.

outer region is dominated by a disk. The narrow bar contributes both to the galactic inner region and the inner disk. We note that the bulge's large position angle remains almost the same as compared to the two-component WISE modeling.

The elongated bar extends to ∼5.3 kpc, which is a bit longer than the rough estimate of 4.56 kpc ($1200''$) from Beaton et al. (2007), but within 1σ agreement with the measurement of ∼5 kpc ($22'$) from their M31-like model galaxy. The measured position angle of the bar is $\sim 50°$, which is ∼12° larger than PA_{disk} and ∼7° smaller than PA_{bulge}. Although we restrict the allowed range for PA_{bar} to be between PA_{disk} and PA_{bulge} based on prior knowledge, it is evident in the morphology of the isophotes that the bar has a position angle deviating from that of the bulge and getting close to the that of disk. Even if we do not apply this strong prior on PA_{bar}, it still does not exceed PA_{bulge}.

In Figure 4.16, the fractional difference between the RGB map and the median model galaxy is shown. There are two prominent RGB overdensities (i.e., under-predicted in the model). In addition to the 10 kpc overdensity, also clearly seen in the WISE two-component residual map, there is another prominent overdensity feature at around 5 kpc where the bar ends.

The stellar number density along the 10 kpc feature is elevated by ∼20-50%. The typical overdensity on the 5 kpc feature is 20–30%. There was a sign (∼25–30% in residual) for the 5 kpc feature in the WISE two-component residual map as well, but the amplitude was 2–3 times weaker than the 10 kpc feature (∼50–80% in residual) in the two-component model, which had higher uncertainty in the inner region than the RGB three-component model. The better modeling of the inner disk with a bar component better reveals the 5 kpc overdensity at the end of the bar. This overdensity is located at around the Davidge object (Davidge 2012), marked as a star in the right panel of Figure 4.15. We discuss this further in Section 4.5 below.

In Figure 4.17, we display both the deprojected residuals in the RGB map and their phase diagram using the position angle and inclination as the WISE deprojection (Figure 4.12). In the deprojected RGB residual map, the 10 kpc overdensity seems more like a ring. However, the morphology of the 10 kpc overdensity is almost identical to that seen in the area of overlap in the WISE residual deprojection (Figure 4.12). In the WISE residual map,

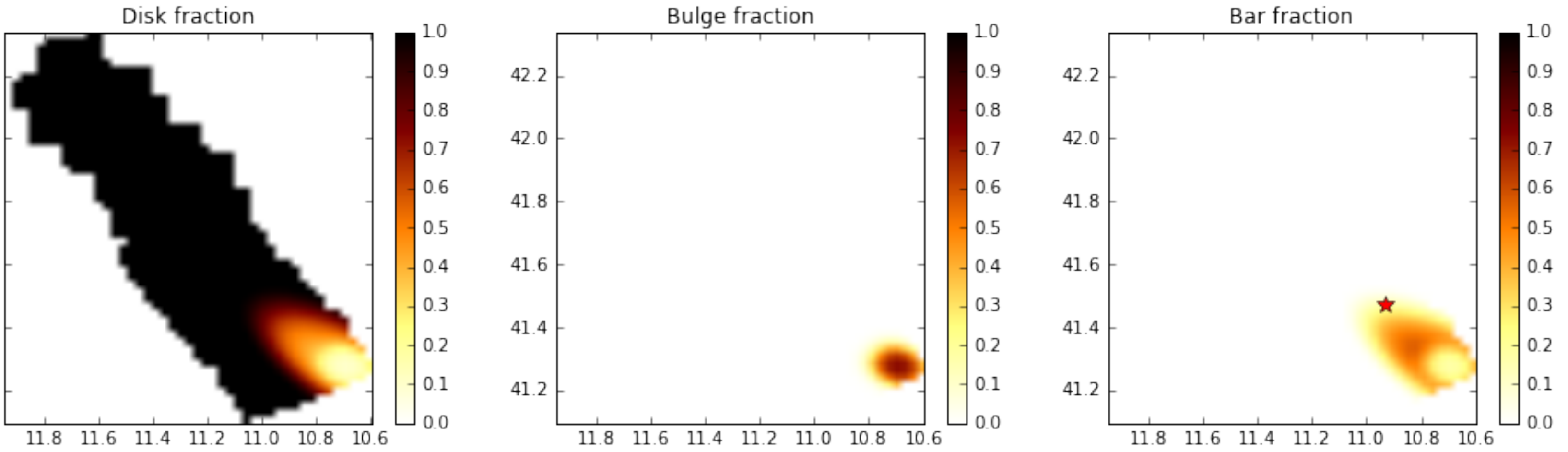

Figure 4.15 The fractional contribution of each component to the final model galaxy.

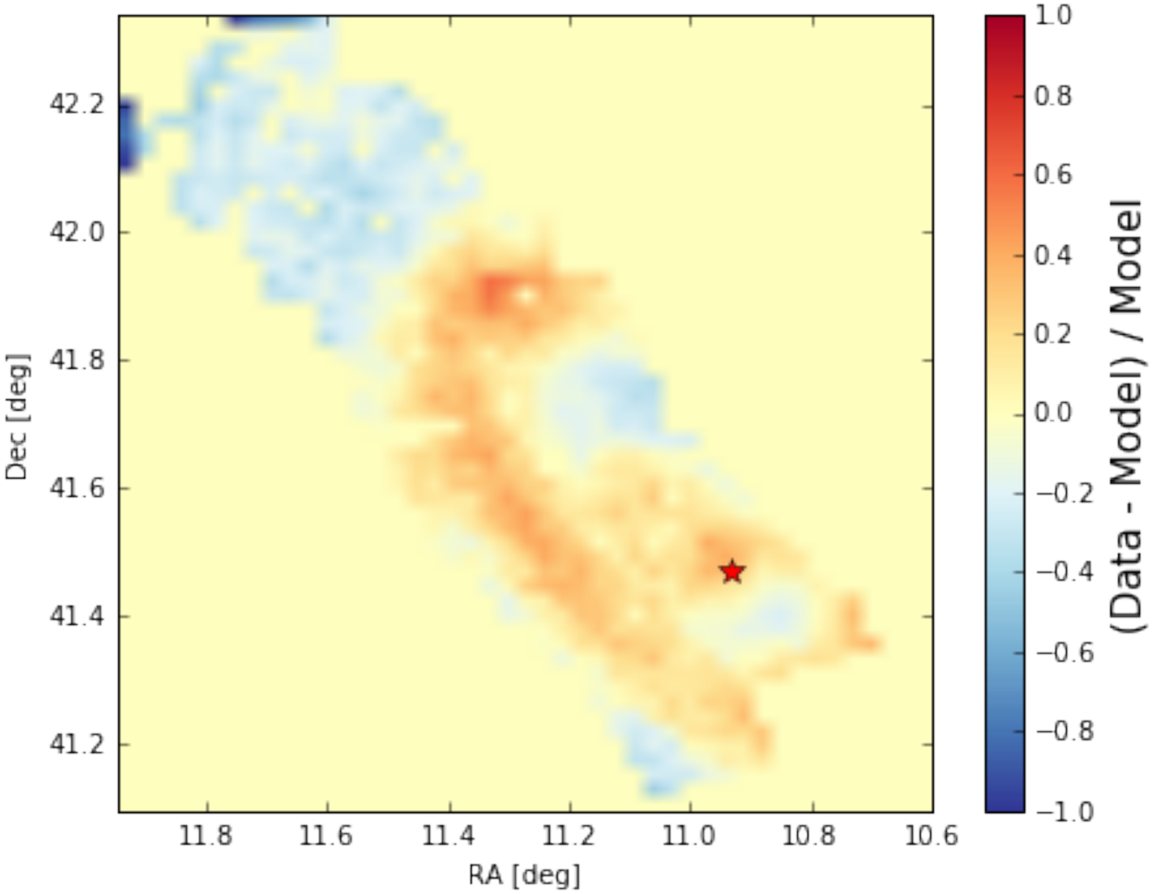

Figure 4.16 Fractional difference between the RGB stellar number density map and the median model. We exclude Brick 1 bulge field where suffers from crowding.

the 10 kpc feature looks patchy.

Although the highest overdensity in the 10 kpc feature is detected at phase $\simeq 4.7$ (270°), the mean overdensity along the 10 kpc feature shows no significant dependence on phase. The amplitude of overdensity scatters between 20 to 50% across the 10 kpc feature at a given phase, even at the both edges of the feature. This trend is also found in the deprojected WISE residual map and indicates that the 10 kpc overdensity has a sharp edge. This differs from a more complete ring-like shape observed in gas tracers such as 24μm, 250μm, and H I(Brinks & Shane 1984; Gordon et al. 2006; Kirk et al. 2015, e.g.,), or in tracers of young stellar populations (e.g., FUV and recent SFH; Gil de Paz et al. 2007; Lewis et al. 2015). Furthermore, our maximum overdensity does not align with the regions, from which the strongest gas emission emerges (between 310°–350°).

In the spatially-resolved recent SFH map, Lewis et al. (2015) found enhanced SFR in both overdensities at 5 and 10 kpc. Although they also found a significant enhancement in the SFR at ∼15 kpc ring-like structure, that feature is not notable in our RGB residual map. This is likely due to a combination of high uncertainty at the outer disk in our RGB modeling and a weaker overdensity compared to overdensities at 5 and 10 kpc. Or, it is also possible that there is indeed no overdensity from old stellar populations at 15 kpc. In this work, we focus on understanding possible origins of the 5 and 10 kpc overdensities.

4.5 Investigating the Causes of the Overdensities (in progress)

From both analysis with the WISE W1 image and the RGB stellar number density map, we have shown that there are two regions where there are excesses of both RGB stars and 3.4 μm flux in a 10 kpc structure and in a localized 5 kpc region along the major axis. However, it is unclear what cause(s) these overdensity features.

If these overdensities result from dynamical effects, then a stellar mass overdensity at these locations should be expected. Fortunately, this scenario is testable by exploring the variation of the mass-to-model RGB number ratio.

Williams et al. (in preparation) reconstructed total stellar mass maps for M31. They derived spatially-resolved ancient SFHs by fitting the CMD in each $83'' \times 83''$ subregion of the PHAT survey, except for Brick 1. They modeled the optical and IR CMDs simultane-

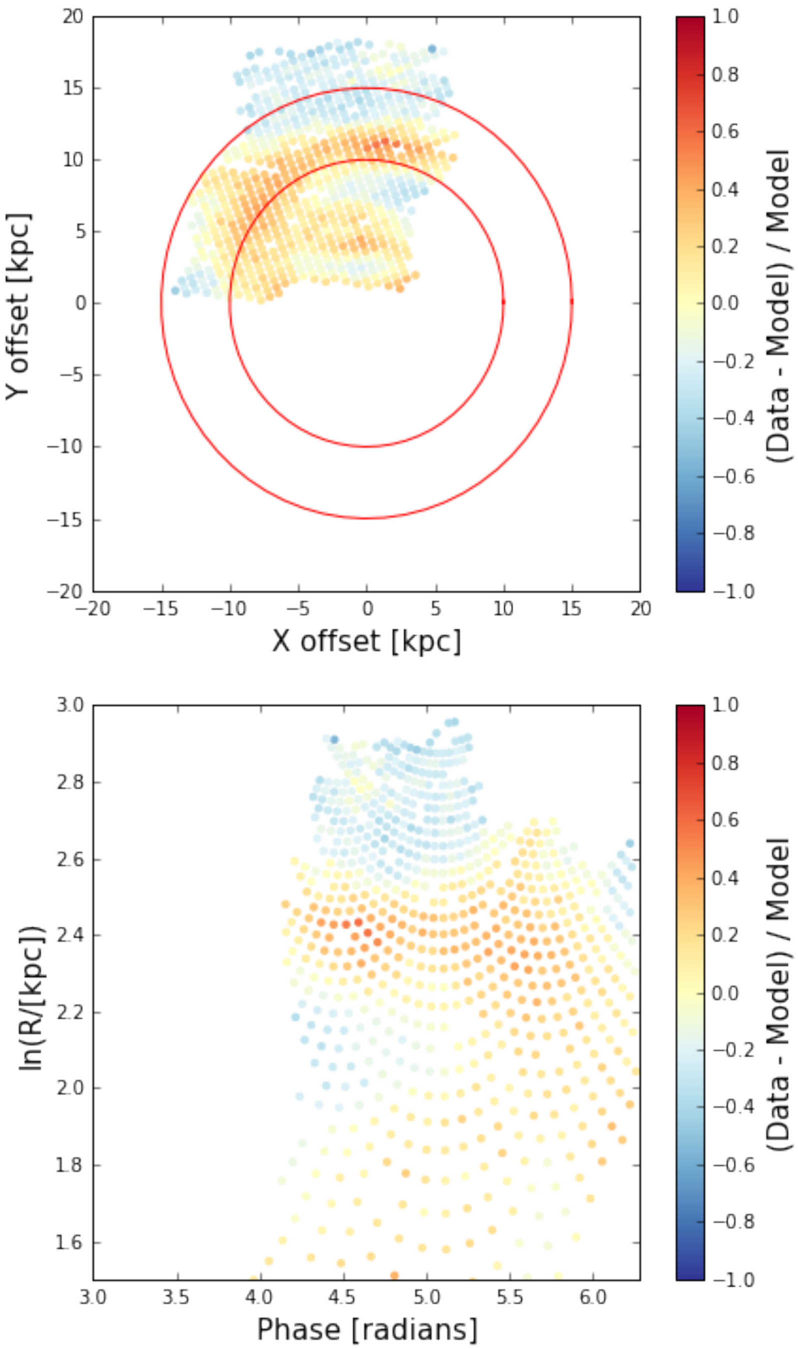

Figure 4.17 Deprojected residuals within the disk and their phase diagram (radius, azimuthal angle). In the top panel, the solid red lines denote 10 and 15 kpc radii, respectively.

ously with a careful dust extinction modeling based on the dust map by Dalcanton et al. (2015). They tried three different stellar evolutionary tracks, and found that the structure of the total stellar mass as a function of position in M31 is robustly constrained, despite of systematic differences between models. This indicates that the choice of a stellar model does not affect the global stellar mass structure study.

We choose to use their two different stellar mass maps from the PADOVA (Marigo et al. 2008; Girardi et al. 2010) model: one with the age-metallicity constrained to have the metallicity increase monotonically with time ("zMass" map hereafter) and the other without this constraint ("Mass" map hereafter). In Figure 4.18, we show these two stellar mass maps. Each map is normalized to its maximum stellar mass. The one without the age-metallicity constraint produces ×4.56 more total stellar mass than the one with the constraint. The variation in the ratio between the two stellar mass maps is small, remaining mostly a constant ratio of $\sim$4.56 across the disk. This supports that the global structures of the two stellar mass maps well agree each other, even though there is a global difference in amplitude.

If the total stellar mass varies smoothly across the M31's disk, as the *model* RGB number density, we predict no structures on a ratio map of the stellar mass to the model RGB number density. However, if the RGB overdensities result from actual enhancement in stellar mass, then the similar overdensity structures are expected to appear in the ratio map.

We present ratio maps of the normalized total stellar mass to the normalized model RGB in Figure 4.19. Each of the stellar mass map and the model RGB map is normalized to its median value. We show the ratio of the normalized maps instead of the ratio of the absolute value maps, which are systematically elevated, because the number density scaling in the model were based on only bright RGB stars whereas the total stellar mass were constructed from the full SFHs. Although the true values for these ratio maps would be different than those shown in our ratio maps, the morphology would remain the same as long as the bright RGB stars represent the distribution of old stellar populations, which is likely to be the case.

The top and the bottom panels of Figure 4.19 show the resulting ratio maps with the "Mass" and "zMass" maps, respectively. In both ratio maps, the almost identical structures

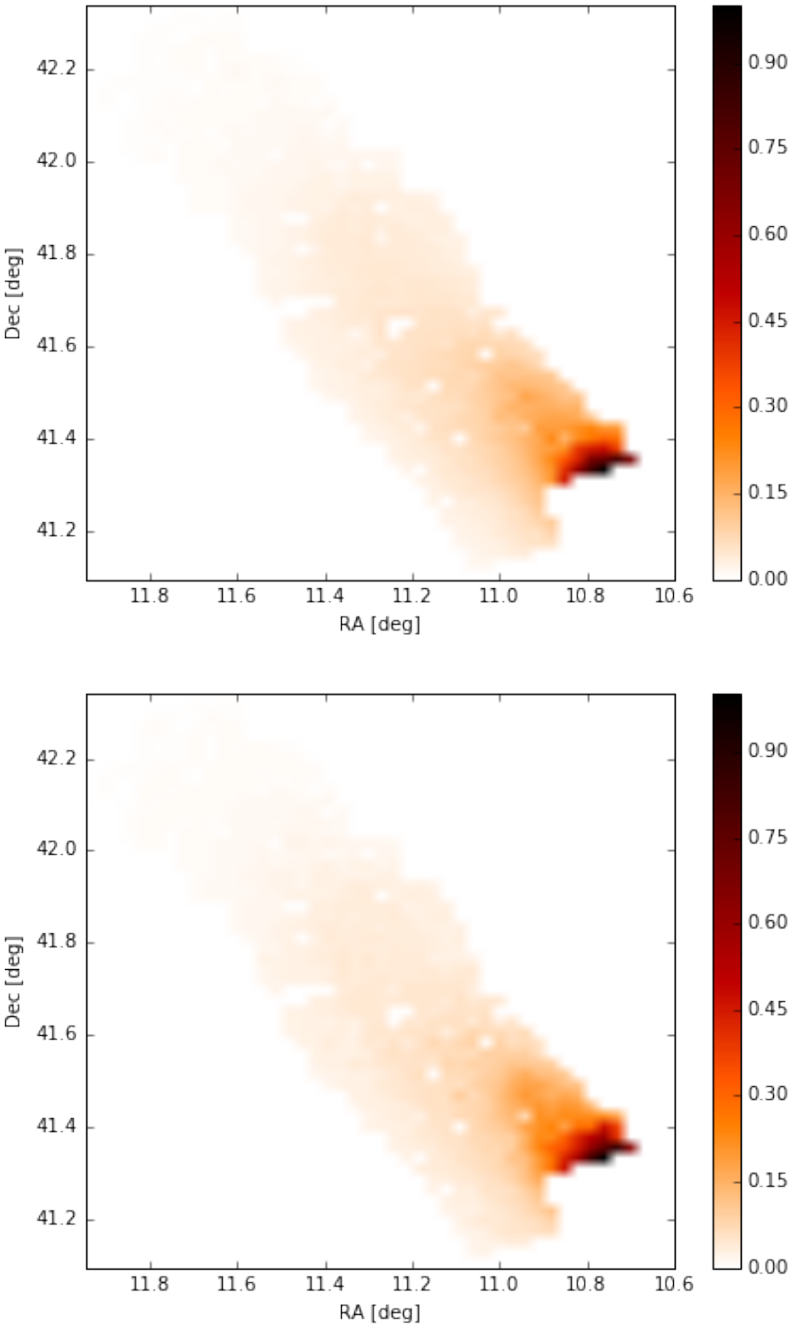

Figure 4.18 Normalized stellar mass maps reconstructed from the derived ancient SFHs (Williams et al., in preparation). The top panel shows the normalized spatially-resolved total stellar mass, measured without the age-metallicity constraint. The bottom panel shows the stellar mass map with the age-metallicity constrained to have the metallicity to increase monotonically with time.

are found at the same locations where we observed the RGB overdensities, indicating more stellar mass compared to the rest parts of the disk. The amplitude of the stellar mass enhancement is ∼30%. This amplitude is comparable to the RGB overdensity at 5 kpc, and slightly less than the 10 kpc overdensity. Therefore, the enhancement in this ratio map suggests that actual stellar mass excesses can explain fully the RGB overdensity at 5 kpc and mostly (not fully) the RGB overdensity at 10 kpc, indicating the overdensities mainly originate from dynamical effects.

The 5 kpc feature has been recognized in various studies. Davidge (2012) observed enhancement in AGB number density at (R.A., Dec.) $= (10^\circ.93, 41^\circ.47)$, marked as a red star in Figure 4.16. Dorman et al. (2015) measured the highest velocity dispersion ($>$100 km s^{-1}) in this region across the PHAT survey region, and they showed that this dynamically hot structure is present in all age bins, such as younger AGB, older AGB, and RGB (both metal-poor and -rich), with older populations being dynamically hotter. This region also shows a significantly enriched metallicity (Gregersen et al. 2015). Lewis et al. (2015) measured enhanced recent SFR in this region over the last few hundred Myr.

Combining these observed properties with our findings that the 5 kpc overdensity can be fully explained by dynamical effect suggests that the 5 kpc overdensity is likely to be induced by the central bar. A gravitational torque generated by the bar leads to form substructures both inside the bar, such as a nuclear ring, nuclear spirals, and dust lanes (e.g., Buta 1986; Athanassoula 1992; Sakamoto et al. 1999; Sheth et al. 2005; Martinez-Valpuesta et al. 2006; Kim et al. 2012), and outside the bar including resonant rings (Buta & Combes 1996). No distinct dynamical populations have been detected in this region (Dorman et al. 2015). Furthermore, significant metallicity enhancement (Gregersen et al. 2015) rules out either alternative possibilities that the 5 kpc overdensity is a satellite dwarf galaxy (Davidge 2012) or that this feature formed recently ($<$ 1 Gyr).

First of all, the central bar can explain most of the observed properties for the 5 kpc overdensity. A bar can accrete gas from the disk into the galactic center, leading to both metal enrichment Di Matteo et al. (2013) and SF activity. The strongest concentration of inflowing gas around the bar can cause dynamical heating of the stars at the end of the bar, i.e., increasing their velocity dispersion. The secular internal heating by the bar can reproduce the age-dispersion correlation seen in M31 (e.g., Dorman et al. 2013).

Secondly, the bar can explain the 10 kpc feature as a outer resonant ring at the outer Lindblad Resonance (OLR) (e.g., Schwarz 1981; Buta 1986). The outer ring is predicted to form at a radius of twice the bar size (Athanassoula et al. 2009), which is 10 kpc for the M31 case. The outer ring results from material accumulation at the OLR, leading to active SF. In fact, the 10 kpc feature in M31, known as the ring of fire, shows elevated SFR over the past 500 Myr (Lewis et al. 2015). Additionally, emission from molecular clouds is strongly concentrated in the 10 kpc ring (Gordon et al. 2006; Kirk et al. 2015, e.g.,).

4.6 Summary & Future Work

We model both the WISE W1 image and the RGB stellar number density map for M31 as a multi-component galaxy. In the both residual maps, we detect excess of 3.4 μm flux and the RGB stellar number density at $\sim$5 and 10 kpc from the galactic center. We also observe significant enhancement in the total stellar mass map in these regions. This mass enhancement can fully explain the amplitude of the 5 kpc overdensity, while partially explain that of the 10 kpc overdensity. Thus our preliminary results suggest that the primary cause for these two overdensities is the dynamical effect, likely due to the central bar. We will continue to verify the bar-induced origin in detail, and explore other possible explanations for these RGB overdensities.

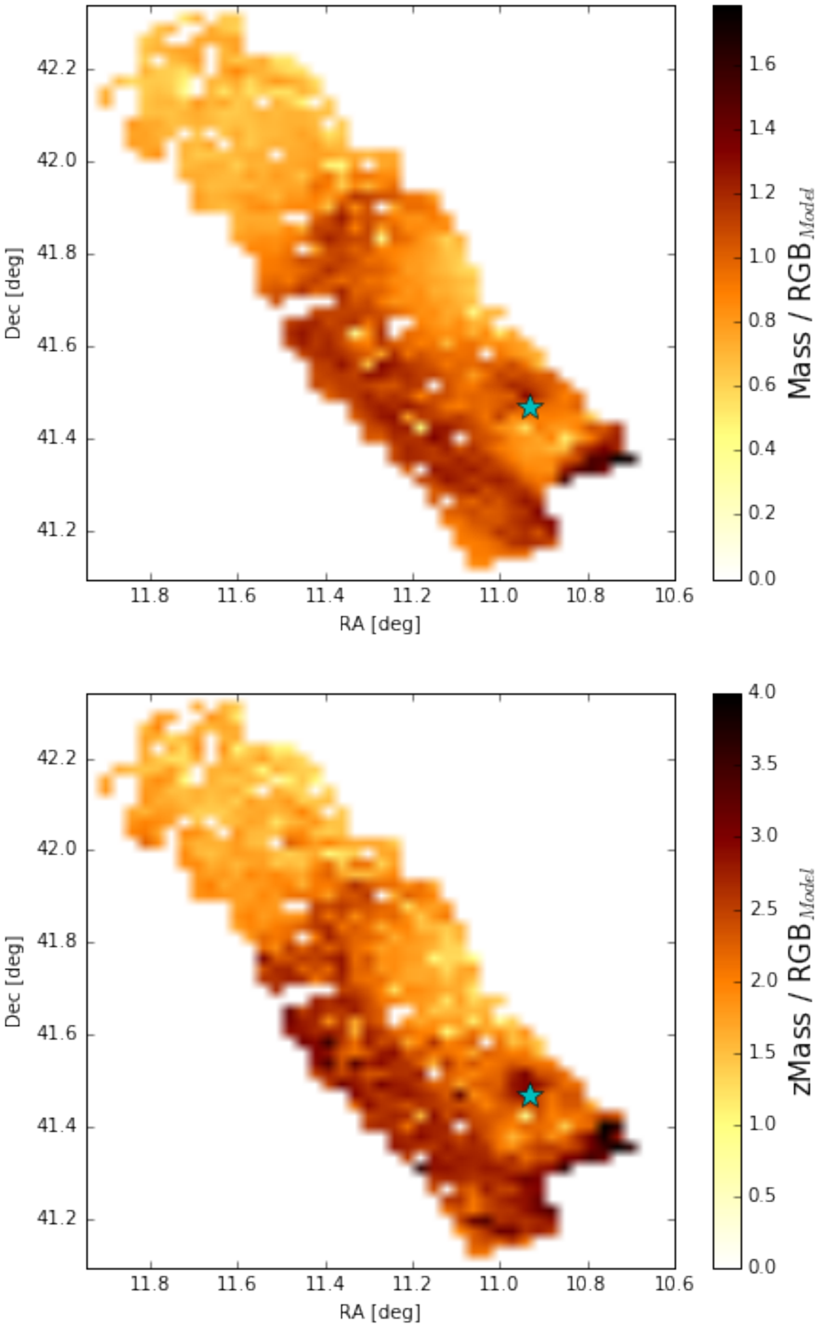

Figure 4.19 Normalized stellar mass maps reconstructed from the derived ancient SFHs (Williams et al. in prep.). The top panel shows the normalized spatially-resolved total stellar mass, measured with the age-metallicity constrained to have the metallicity to increase monotonically with time. The bottom panel shows the stellar mass map without this constraint.

Chapter 5

CONCLUSION

Individual stars in a galaxy have recorded a history of their host galaxy, therefore they are valuable tools to understand past and current astrophysical processes that occurred in the galaxy. My dissertation research contributes to the understanding of various aspects of galactic physics using the power of resolved stellar populations, imaged in multiple wavelengths by HST. Here, I summarize my work.

In Chapter 2, I introduced a new methodology to measure the escape fraction of ionizing photons from a galaxy, and applied that to the nearest starburst dwarf galaxy NGC 4214, an excellent analog of high-z star forming galaxies. In recent years, the escape fraction of ionizing photons from galaxies has been an active topic in cosmology, because it determines whether they emitted sufficient UV photons to reionize the IGM. Whereas our understanding of reionization history has been well constrained, which sources are responsible has not. Most likely contributing sources to cosmic reionization are dwarf star forming galaxies. In galaxies with shallower potential wells, stellar feedback from massive stars can damage the ISM severely and thus create holes in the ISM along which ionizing photons can escape. Nevertheless, observational measurement of the escape fraction from galaxies have not been successful in that they are lower than the required values to reionize the IGM at the epoch of reionization ($z > 6$). I discussed several obstacles associated with the previous measurements in Chapter 2.

Contrary to the traditional methodologies using spatially-averaged composite spectra or images, my new method to measure the escape fraction used individual stars within a galaxy. For NGC 4214, I used ~83,000 stars imaged by HST in 6 filters, including 2 UV, 2 optical, and 2 IR. From these multi-wavelength photometry, I constructed broad stellar SEDs for individual stars and model these observed stellar SEDs using the probabilistic SED fitting tool, called BEAST. I describe the general aspects of the BEAST as well as the specific settings for NGC 4214. I calculated the number of intrinsic ionizing photons produced by each star and the number of ionizing photons absorbed by dust along the line-of-sight toward each star using the stellar SED fitting results.

I then separately measured the number of ionizing photons consumed by neutral hydrogen in the ISM from the extinction-corrected Hα recombination emission. By taking the ratio between the number of ionizing photons not consumed by either the gas or dust and the number of intrinsic ionizing photons, I measured the line-of-sight local escape fraction for individual star forming regions in NGC 4214 presented as a map. I found a significant local variation in the escape fraction with position, from 0–20% depending both on the morphology of H II region and stellar contents. I also measured the global escape fraction for the entire galaxy. It varied from 2.65% to 21.03% with a median of 11.84% based on the covering factor adopted. This high escape fraction from a dwarf galaxy is promising, supporting the scenario in that small star forming galaxies provide ionizing photons to the IGM at the epoch of reionization. I will apply my new methodology to a larger sample of nearby dwarf galaxies to obtain more local measurements. I believe that detailed analysis of the escape fractions in analogs of high-z galaxies can improve our understanding of cosmic reionization.

In Chapter 3, I tested the stationary density wave theory with a grand-design spiral galaxy M81, one of the largest grand-design spirals in nearby universe. In this theory, grand-design spiral arms are stationary density waves that propagate through a galactic disk with a constant pattern speed, and stars and gas move though the spiral pattern. As gas moves through the spiral potential well, it becomes dense enough to ignite star formation. Therefore, the density wave theory predicts the systematic stellar age gradient across a spiral arm: spiral arm with younger ages at the upstream side and older ages at the downstream side.

In M81, I divided one of its spiral arm into 20 sub-regions and measured SFHs for individual regions by modeling their observed CMDs. Then I compared the spatially resolved SFHs around the spiral arm with various different predicted star formation propagation across the spiral arm. I showed that the measured SFHs were stochastic and, none of the predictions match the measured SFHs. I discussed alternative mechanism that can result in two-armed grand-design spirals: tidal interaction with companion galaxies M82 and NGC 3077. I concluded that our findings in M81 are consistent with tidally-induced grand-design spiral arms.

In Chapter 4, I briefly presented preliminary results from work in progress. The nearest galaxy M31 shows two interesting galactic structures: the 10 kpc star-forming feature and the 5 kpc round-shaped feature. The ultimate goal of this work is to understand the origin of these structures. First, I decomposed M31's galactic structures using the WISE W1 image with an exponential disk and a Sérsic bulge to characterize the global galactic structure. Then I modeled the RGB stellar number density map constructed from the PHAT IR photometry with an extra bar component. From each of the residual maps (i.e., data − model), I detected significant positive residuals at the 5 kpc and 10 kpc. I also found a significant enhancement in the stellar mass at the same regions. In future work, I will explore the origin of these overdensities more in detail.

BIBLIOGRAPHY

Alexandroff, R. M., Heckman, T. M., Borthakur, S., Overzier, R., & Leitherer, C. 2015, ApJ, 810, 104

Appleton, P. N., Davies, R. D., & Stephenson, R. J. 1981, MNRAS, 195, 327

Athanassoula, E. 1992, MNRAS, 259, 345

Athanassoula, E., & Beaton, R. L. 2006, MNRAS, 370, 1499

Athanassoula, E., Romero-Gómez, M., & Masdemont, J. J. 2009, MNRAS, 394, 67

Baade, W., & Arp, H. 1964, ApJ, 139, 1027

Baba, J., Saitoh, T. R., & Wada, K. 2013, ApJ, 763, 46

Barkana, R., & Loeb, A. 2001, Phys. Rep., 349, 125

Barmby, P., Ashby, M. L. N., Bianchi, L., et al. 2006, ApJ, 650, L45

Bastian, N., Covey, K. R., & Meyer, M. R. 2010, ARA&A, 48, 339

Beaton, R. L., Majewski, S. R., Guhathakurta, P., et al. 2007, ApJ, 658, L91

Bendo, G. J., Wilson, C. D., Pohlen, M., et al. 2010, A&A, 518, L65

Bergemann, M., Lind, K., Collet, R., Magic, Z., & Asplund, M. 2012, MNRAS, 427, 27

Bergvall, N., Zackrisson, E., Andersson, B.-G., et al. 2006, A&A, 448, 513

Bertin, E., & Arnouts, S. 1996, A&AS, 117, 393

Bianchi, L., Clayton, G. C., Bohlin, R. C., Hutchings, J. B., & Massey, P. 1996, ApJ, 471, 203

Block, D. L., Bournaud, F., Combes, F., et al. 2006, Nature, 443, 832

Bohlin, R. C., Gordon, K. D., & Tremblay, P.-E. 2014, PASP, 126, 711

Borthakur, S., Heckman, T. M., Leitherer, C., & Overzier, R. A. 2014, Science, 346, 216

Bottema, R. 2003, MNRAS, 344, 358

Bouwens, R. J., Illingworth, G. D., Oesch, P. A., et al. 2015, ApJ, 811, 140

—. 2012, ApJ, 752, L5

Braun, R. 1991, ApJ, 372, 54

Bressan, A., Marigo, P., Girardi, L., et al. 2012, MNRAS, 427, 127

Brinks, E., & Shane, W. W. 1984, A&AS, 55, 179

Buta, R. 1986, ApJS, 61, 609

Buta, R., & Combes, F. 1996, Fund. Cosmic Phys., 17, 95

Calzetti, D., Harris, J., Gallagher, III, J. S., et al. 2004, AJ, 127, 1405

Capaccioli, M. 1989, in World of Galaxies (Le Monde des Galaxies), ed. H. G. Corwin, Jr. & L. Bottinelli, 208–227

Cardamone, C., Schawinski, K., Sarzi, M., et al. 2009, MNRAS, 399, 1191

Cardelli, J. A., Clayton, G. C., & Mathis, J. S. 1989, ApJ, 345, 245

Castelli, F., & Kurucz, R. L. 2004, ArXiv Astrophysics e-prints, astro-ph/0405087

Chandar, R., Tsvetanov, Z., & Ford, H. C. 2001, AJ, 122, 1342

Chapman, S. C., Ibata, R., Lewis, G. F., et al. 2006, ApJ, 653, 255

Collins, M. L. M., Chapman, S. C., Ibata, R. A., et al. 2011, MNRAS, 413, 1548

Cormier, D., Madden, S. C., Hony, S., et al. 2010, A&A, 518, L57

Courteau, S., Widrow, L. M., McDonald, M., et al. 2011, ApJ, 739, 20

Dalcanton, J. J., Williams, B. F., Seth, A. C., et al. 2009, ApJS, 183, 67

Dalcanton, J. J., Williams, B. F., Lang, D., et al. 2012, ApJS, 200, 18

Dalcanton, J. J., Fouesneau, M., Hogg, D. W., et al. 2015, ApJ, 814, 3

Dale, D. A., Cohen, S. A., Johnson, L. C., et al. 2009, ApJ, 703, 517

Davidge, T. J. 2012, ApJ, 749, L7

de Blok, W. J. G., Walter, F., Brinks, E., et al. 2008, AJ, 136, 2648

de Mello, D. F., Smith, L. J., Sabbi, E., et al. 2008, AJ, 135, 548

Di Matteo, P., Haywood, M., Combes, F., Semelin, B., & Snaith, O. N. 2013, A&A, 553, A102

Dobbs, C., & Baba, J. 2014, PASA, 31, e035

Dobbs, C. L., & Pringle, J. E. 2010, MNRAS, 409, 396

Dobbs, C. L., Theis, C., Pringle, J. E., & Bate, M. R. 2010, MNRAS, 403, 625

Dolphin, A. E. 2000, PASP, 112, 1383

—. 2002, MNRAS, 332, 91

—. 2012, ApJ, 751, 60

—. 2013, ApJ, 775, 76

D'Onghia, E., Vogelsberger, M., & Hernquist, L. 2013, ApJ, 766, 34

Dorman, C. E., Widrow, L. M., Guhathakurta, P., et al. 2013, ApJ, 779, 103

Dorman, C. E., Guhathakurta, P., Seth, A. C., et al. 2015, ApJ, 803, 24

Draine, B. T. 2003, ARA&A, 41, 241

Draine, B. T., Aniano, G., Krause, O., et al. 2014, ApJ, 780, 172

Dunkley, J., Komatsu, E., Nolta, M. R., et al. 2009, ApJS, 180, 306

Egusa, F., Kohno, K., Sofue, Y., Nakanishi, H., & Komugi, S. 2009, ApJ, 697, 1870

Elmegreen, B. G. 2000, ApJ, 530, 277

—. 2011, ApJ, 737, 10

Elmegreen, B. G., Seiden, P. E., & Elmegreen, D. M. 1989, ApJ, 343, 602

Fan, X., Strauss, M. A., Becker, R. H., et al. 2006, AJ, 132, 117

Feng, C.-C., Lin, L.-H., Wang, H.-H., & Taam, R. E. 2014, ApJ, 785, 103

Ferguson, A. M. N., Irwin, M. J., Ibata, R. A., Lewis, G. F., & Tanvir, N. R. 2002, AJ, 124, 1452

Ferreras, I., Cropper, M., Kawata, D., Page, M., & Hoversten, E. A. 2012, MNRAS, 424, 1636

Finkelstein, S. L., Papovich, C., Ryan, R. E., et al. 2012, ApJ, 758, 93

Finkelstein, S. L., Ryan, Jr., R. E., Papovich, C., et al. 2015, ApJ, 810, 71

Fitzpatrick, E. L. 1999, PASP, 111, 63

Foreman-Mackey, D., Hogg, D. W., Lang, D., & Goodman, J. 2013, PASP, 125, 306

Foyle, K., Rix, H.-W., Dobbs, C. L., Leroy, A. K., & Walter, F. 2011, ApJ, 735, 101

Fritz, J., Gentile, G., Smith, M. W. L., et al. 2012, A&A, 546, A34

Fujii, M. S., Baba, J., Saitoh, T. R., et al. 2011, ApJ, 730, 109

Gil de Paz, A., Boissier, S., Madore, B. F., et al. 2007, ApJS, 173, 185

Girardi, L., Bertelli, G., Bressan, A., et al. 2002, A&A, 391, 195

Girardi, L., Williams, B. F., Gilbert, K. M., et al. 2010, ApJ, 724, 1030

Gnedin, N. Y., Kravtsov, A. V., & Chen, H.-W. 2008, ApJ, 672, 765

Gogarten, S. M., Dalcanton, J. J., Williams, B. F., et al. 2009, ApJ, 691, 115

Goldreich, P., & Lynden-Bell, D. 1965, MNRAS, 130, 125

Gordon, K. D., Cartledge, S., & Clayton, G. C. 2009, ApJ, 705, 1320

Gordon, K. D., & Clayton, G. C. 1998, ApJ, 500, 816

Gordon, K. D., Clayton, G. C., Misselt, K. A., Landolt, A. U., & Wolff, M. J. 2003, ApJ, 594, 279

Gordon, K. D., Bailin, J., Engelbracht, C. W., et al. 2006, ApJ, 638, L87

Gordon, K. D., Fouesneau, M., Arab, H., et al. 2016, ApJ, 826, 104

Gottesman, S. T., & Weliachew, L. 1975, ApJ, 195, 23

Grand, R. J. J., Kawata, D., & Cropper, M. 2012, MNRAS, 421, 1529

Gregersen, D., Seth, A. C., Williams, B. F., et al. 2015, AJ, 150, 189

Grimes, J. P., Heckman, T., Aloisi, A., et al. 2009, ApJS, 181, 272

Gunn, J. E., & Peterson, B. A. 1965, ApJ, 142, 1633

Haas, M., Lemke, D., Stickel, M., et al. 1998, A&A, 338, L33

Habing, H. J., Miley, G., Young, E., et al. 1984, ApJ, 278, L59

Haywood, M. 2008, MNRAS, 388, 1175

Heckman, T. M., Borthakur, S., Overzier, R., et al. 2011, ApJ, 730, 5

Hermelo, I., Lisenfeld, U., Relaño, M., et al. 2013, A&A, 549, A70

Hernquist, L. 1990, Dynamical status of M51., ed. R. Wielen, 108–117

Hodge, P. W. 1979, AJ, 84, 744

Hoopes, C. G., Walterbos, R. A. M., & Bothun, G. D. 2001, ApJ, 559, 878

Hoversten, E. A., Gronwall, C., Vanden Berk, D. E., et al. 2011, AJ, 141, 205

Hummer, D. G., & Storey, P. J. 1987, MNRAS, 224, 801

Iwata, I., Inoue, A. K., Matsuda, Y., et al. 2009, ApJ, 692, 1287

Izotov, Y. I., Orlitová, I., Schaerer, D., et al. 2016a, Nature, 529, 178

Izotov, Y. I., Schaerer, D., Thuan, T. X., et al. 2016b, ArXiv e-prints, arXiv:1605.05160

Jaskot, A. E., & Oey, M. S. 2013, ApJ, 766, 91

Julian, W. H., & Toomre, A. 1966, ApJ, 146, 810

Kalirai, J. S., Gilbert, K. M., Guhathakurta, P., et al. 2006, ApJ, 648, 389

Karachentsev, I. D., Karachentseva, V. E., Huchtmeier, W. K., & Makarov, D. I. 2004, AJ, 127, 2031

Kendall, S., Kennicutt, R. C., Clarke, C., & Thornley, M. D. 2008, MNRAS, 387, 1007

Kennicutt, R. C., & Evans, N. J. 2012, ARA&A, 50, 531

Kennicutt, Jr., R. C. 1981, AJ, 86, 1847

—. 1998, ARA&A, 36, 189

Khaire, V., Srianand, R., Choudhury, T. R., & Gaikwad, P. 2016, MNRAS, 457, 4051

Kim, W.-T., Seo, W.-Y., & Kim, Y. 2012, ApJ, 758, 14

Kimm, T., & Cen, R. 2014, ApJ, 788, 121

Kirk, J. M., Gear, W. K., Fritz, J., et al. 2015, ApJ, 798, 58

Kobulnicky, H. A., & Skillman, E. D. 1996, ApJ, 471, 211

Koekemoer, A. M., Fruchter, A. S., Hook, R. N., & Hack, W. 2003, in HST Calibration Workshop : Hubble after the Installation of the ACS and the NICMOS Cooling System, ed. S. Arribas, A. Koekemoer, & B. Whitmore, 337

Konstantopoulos, I. S., Bastian, N., Smith, L. J., et al. 2009, ApJ, 701, 1015

Kormendy, J., & Norman, C. A. 1979, ApJ, 233, 539

Krist, J. 1995, in Astronomical Society of the Pacific Conference Series, Vol. 77, Astronomical Data Analysis Software and Systems IV, ed. R. A. Shaw, H. E. Payne, & J. J. E. Hayes, 349

Kroupa, P. 2001, MNRAS, 322, 231

Lang, D. 2014, AJ, 147, 108

Lang, D., Hogg, D. W., Mierle, K., Blanton, M., & Roweis, S. 2010, AJ, 139, 1782

Lanz, T., & Hubeny, I. 2003, ApJS, 146, 417

—. 2007, ApJS, 169, 83

Laurikainen, E., Salo, H., Buta, R., & Knapen, J. H. 2007, MNRAS, 381, 401

Lee, J. C., Gil de Paz, A., Tremonti, C., et al. 2009, ApJ, 706, 599

Lee, J. C., Gil de Paz, A., Kennicutt, Jr., R. C., et al. 2011, ApJS, 192, 6

Leitet, E., Bergvall, N., Hayes, M., Linné, S., & Zackrisson, E. 2013, A&A, 553, A106

Leitherer, C., Hernandez, S., Lee, J. C., & Oey, M. S. 2016, ApJ, 823, 64

Leitherer, C., Vacca, W. D., Conti, P. S., et al. 1996, ApJ, 465, 717

Leitherer, C., Schaerer, D., Goldader, J. D., et al. 1999, ApJS, 123, 3

Leroy, A. K., Bigiel, F., de Blok, W. J. G., et al. 2012, AJ, 144, 3

Lewis, A. R., Dolphin, A. E., Dalcanton, J. J., et al. 2015, ApJ, 805, 183

Li, A., & Draine, B. T. 2001, ApJ, 554, 778

Lim, S., Hwang, N., & Lee, M. G. 2013, ApJ, 766, 20

Lin, C. C., & Shu, F. H. 1964, ApJ, 140, 646

Lindblad, P. O. 1960, Stockholms Observatoriums Annaler, 21

Lintott, C., Schawinski, K., Bamford, S., et al. 2011, MNRAS, 410, 166

Loinard, L., Dame, T. M., Heyer, M. H., Lequeux, J., & Thaddeus, P. 1999, A&A, 351, 1087

Louie, M., Koda, J., & Egusa, F. 2013, ApJ, 763, 94

Lowe, S. A., Roberts, W. W., Yang, J., Bertin, G., & Lin, C. C. 1994, ApJ, 427, 184

Ma, X., Kasen, D., Hopkins, P. F., et al. 2015, MNRAS, 453, 960

MacKenty, J. W., Maíz-Apellániz, J., Pickens, C. E., Norman, C. A., & Walborn, N. R. 2000, AJ, 120, 3007

Maiz-Apellaniz, J., Mas-Hesse, J. M., Munoz-Tunon, C., Vilchez, J. M., & Castaneda, H. O. 1998, A&A, 329, 409

Maíz Apellániz, J., & Rubio, M. 2012, A&A, 541, A54

Marigo, P., Girardi, L., Bressan, A., et al. 2008, A&A, 482, 883

Martínez-García, E. E., & González-Lópezlira, R. A. 2013, ApJ, 765, 105

Martinez-Valpuesta, I., Shlosman, I., & Heller, C. 2006, ApJ, 637, 214

McConnachie, A. W., Irwin, M. J., Ferguson, A. M. N., et al. 2005, MNRAS, 356, 979

McGreer, I. D., Mesinger, A., & D'Odorico, V. 2015, MNRAS, 447, 499

McLeod, D. J., McLure, R. J., Dunlop, J. S., et al. 2015, MNRAS, 450, 3032

McQuinn, K. B. W., Skillman, E. D., Dalcanton, J. J., et al. 2012, ApJ, 759, 77

McQuinn, K. B. W., Skillman, E. D., Cannon, J. M., et al. 2010, ApJ, 721, 297

Misselt, K. A., Clayton, G. C., & Gordon, K. D. 1999, ApJ, 515, 128

Murphy, E. J., Condon, J. J., Schinnerer, E., et al. 2011, ApJ, 737, 67

Nair, P. B., & Abraham, R. G. 2010, ApJS, 186, 427

Nakajima, K., & Ouchi, M. 2014, MNRAS, 442, 900

Nestor, D. B., Shapley, A. E., Kornei, K. A., Steidel, C. C., & Siana, B. 2013, ApJ, 765, 47

Nieten, C., Neininger, N., Guélin, M., et al. 2006, A&A, 453, 459

Oh, S. H., Kim, W.-T., & Lee, H. M. 2015, ApJ, 807, 73

Oh, S. H., Kim, W.-T., Lee, H. M., & Kim, J. 2008, ApJ, 683, 94

Ostriker, E. C., Stone, J. M., & Gammie, C. F. 2001, ApJ, 546, 980

Ouchi, M., Mobasher, B., Shimasaku, K., et al. 2009, ApJ, 706, 1136

Paardekooper, J.-P., Khochfar, S., & Dalla Vecchia, C. 2015, MNRAS, 451, 2544

Peng, C. Y., Ho, L. C., Impey, C. D., & Rix, H.-W. 2010, AJ, 139, 2097

Pérez-González, P. G., Kennicutt, Jr., R. C., Gordon, K. D., et al. 2006, ApJ, 648, 987

Planck Collaboration, Ade, P. A. R., Aghanim, N., et al. 2015, ArXiv e-prints, arXiv:1502.01589

Puerari, I., Elmegreen, B. G., & Block, D. L. 2014, AJ, 148, 133

Rauch, T., Werner, K., Bohlin, R., & Kruk, J. W. 2013, A&A, 560, A106

Roberts, W. W. 1969, ApJ, 158, 123

Roberts, Jr., W. W., Roberts, M. S., & Shu, F. H. 1975, ApJ, 196, 381

Robertson, B. E., Ellis, R. S., Furlanetto, S. R., & Dunlop, J. S. 2015, ApJ, 802, L19

Robertson, B. E., Furlanetto, S. R., Schneider, E., et al. 2013, ApJ, 768, 71

Romaniello, M., Panagia, N., Scuderi, S., & Kirshner, R. P. 2002, AJ, 123, 915

Rosenfield, P., Marigo, P., Girardi, L., et al. 2016, ApJ, 822, 73

Rots, A. H. 1975, A&A, 45, 43

Roškar, R., Debattista, V. P., Quinn, T. R., Stinson, G. S., & Wadsley, J. 2008, ApJ, 684, L79

Sakamoto, K., Okumura, S. K., Ishizuki, S., & Scoville, N. Z. 1999, ApJ, 525, 691

Sakhibov, F. K., & Smirnov, M. A. 1987, Soviet Ast., 31, 132

Santiago-Cortés, M., Mayya, Y. D., & Rosa-González, D. 2010, MNRAS, 405, 1293

Schlafly, E. F., & Finkbeiner, D. P. 2011, ApJ, 737, 103

Schlegel, D. J., Finkbeiner, D. P., & Davis, M. 1998, ApJ, 500, 525

Schwarz, M. P. 1981, ApJ, 247, 77

Schweizer, F. 1976, ApJS, 31, 313

Seigar, M. S., Barth, A. J., & Bullock, J. S. 2008, MNRAS, 389, 1911

Sellwood, J. A. 2011, MNRAS, 410, 1637

Sellwood, J. A., & Binney, J. J. 2002, MNRAS, 336, 785

Sellwood, J. A., & Carlberg, R. G. 1984, ApJ, 282, 61

—. 2014, ApJ, 785, 137

Sérsic, J. L. 1968, Atlas de galaxias australes

Shapley, A. E., Steidel, C. C., Pettini, M., Adelberger, K. L., & Erb, D. K. 2006, ApJ, 651, 688

Sheth, K., Vogel, S. N., Regan, M. W., Thornley, M. D., & Teuben, P. J. 2005, ApJ, 632, 217

Siana, B., Teplitz, H. I., Colbert, J., et al. 2007, ApJ, 668, 62

Sollima, A., Cignoni, M., Gratton, R. G., et al. 2014, MNRAS, 437, 1918

Speights, J. C., & Westpfahl, D. J. 2011, ApJ, 736, 70

Struck, C., Dobbs, C. L., & Hwang, J.-S. 2011, MNRAS, 414, 2498

Tamburro, D., Rix, H.-W., Walter, F., et al. 2008, AJ, 136, 2872

Tang, J., Bressan, A., Rosenfield, P., et al. 2014, MNRAS, 445, 4287

Tempel, E., Tuvikene, T., Tamm, A., & Tenjes, P. 2011, A&A, 526, A155

Thomasson, M., & Donner, K. J. 1993, A&A, 272, 153

Toomre, A., & Toomre, J. 1972, ApJ, 178, 623

Úbeda, L., Maíz-Apellániz, J., & MacKenty, J. W. 2007, AJ, 133, 932

Valencic, L. A., Clayton, G. C., & Gordon, K. D. 2004, ApJ, 616, 912

van den Bergh, S. 1991, PASP, 103, 1053

Vanzella, E., Guo, Y., Giavalisco, M., et al. 2012, ApJ, 751, 70

Visser, H. C. D. 1980, A&A, 88, 149

Wada, K., Baba, J., & Saitoh, T. R. 2011, ApJ, 735, 1

Walter, F., Brinks, E., de Blok, W. J. G., et al. 2008, AJ, 136, 2563

Walter, F., Taylor, C. L., Hüttemeister, S., Scoville, N., & McIntyre, V. 2001, AJ, 121, 727

Walterbos, R. A. M., & Kennicutt, Jr., R. C. 1987, A&AS, 69, 311

Weingartner, J. C., & Draine, B. T. 2001, ApJ, 548, 296

Weisz, D. R., Dolphin, A. E., Skillman, E. D., et al. 2014, ApJ, 789, 148

Weisz, D. R., Dalcanton, J. J., Williams, B. F., et al. 2011, ApJ, 739, 5

Westera, P., Lejeune, T., Buser, R., Cuisinier, F., & Bruzual, G. 2002, A&A, 381, 524

Westpfahl, D. J. 1998, ApJS, 115, 203

Williams, B. F., Dalcanton, J. J., Gilbert, K. M., et al. 2011, ApJ, 735, 22

Williams, B. F., Dalcanton, J. J., Seth, A. C., et al. 2009, AJ, 137, 419

Williams, B. F., Lang, D., Dalcanton, J. J., et al. 2014, ApJS, 215, 9

Wise, J. H., & Cen, R. 2009, ApJ, 693, 984

Wright, E. L., Eisenhardt, P. R. M., Mainzer, A. K., et al. 2010, AJ, 140, 1868

Yajima, H., Choi, J.-H., & Nagamine, K. 2011, MNRAS, 412, 411

Yun, M. S. 1999, in IAU Symposium, Vol. 186, Galaxy Interactions at Low and High Redshift, ed. J. E. Barnes & D. B. Sanders, 81

Yun, M. S., Ho, P. T. P., & Lo, K. Y. 1994, Nature, 372, 530

VITA

Yumi Choi was born in Busan, South Korea to Dong Chang Choi and Jiyeon Lee, and raised with her sister Yujin. She attended Yonsei University where she was a recipient of the Korean Science and Engineering Grant for four years and the Brain Korea 21 Fellowship for two years. She earned a BS and a MS degree in Astronomy from Yonsei University in 2009, and moved to the United States to purse her PhD in Astronomy at the University of Washington. During her PhD, she was awarded the HST research grant (Cycle 23) as a science PI. She completed her doctorate in 2016, and will start working as a postdoctoral research associate at the University of Arizona.